

Complexity

Advanced Methods to Analyse the Complexity of the Brain

Lead Guest Editor: Nadia Mammone

Guest Editors: Hamed Azami and Gaoxiang Ouyang





Advanced Methods to Analyse the Complexity of the Brain

Complexity

Advanced Methods to Analyse the Complexity of the Brain

Lead Guest Editor: Nadia Mammone

Guest Editors: Hamed Azami and Gaoxiang Ouyang



Copyright © 2018 Hindawi. All rights reserved.

This is a special issue published in “Complexity.” All articles are open access articles distributed under the Creative Commons Attribution License, which permits unrestricted use, distribution, and reproduction in any medium, provided the original work is properly cited.

Editorial Board

- José A. Acosta, Spain
Carlos F. Aguilar-Ibáñez, Mexico
Tarek Ahmed-Ali, France
Basil M. Al-Hadithi, Spain
Juan A. Almendral, Spain
Diego R. Amancio, Brazil
David Arroyo, Spain
Mohamed Boutayeb, France
Arturo Buscarino, Italy
Guido Caldarelli, Italy
Eric Campos-Canton, Mexico
Mohammed Chadli, France
Diyi Chen, China
Giulio Cimini, Italy
Danilo Comminiello, Italy
Sara Dadras, USA
Manlio De Domenico, Italy
Pietro De Lellis, Italy
Albert Diaz-Guilera, Spain
Thach Ngoc Dinh, France
Jordi Duch, Spain
Marcio Eisencraft, Brazil
Joshua Epstein, USA
Mondher Farza, France
Thierry Floquet, France
Mattia Frasca, Italy
Lucia Valentina Gambuzza, Italy
Bernhard C. Geiger, Austria
- Carlos Gershenson, Mexico
Peter Giesl, UK
Sergio Gómez, Spain
Lingzhong Guo, UK
Xianggui Guo, China
Sigurdur F. Hafstein, Iceland
Chittaranjan Hens, Israel
Giacomo Innocenti, Italy
Sarangapani Jagannathan, USA
Mahdi Jalili, Australia
Jeffrey H. Johnson, UK
M. Hassan Khooban, Denmark
Vincent Labatut, France
Lucas Lacasa, UK
Qingdu Li, Germany
Chongyang Liu, China
Xiaoping Liu, Canada
R. M. Lopez Gutierrez, Mexico
Vittorio Loreto, Italy
Didier Maquin, France
Eulalia Martínez, Spain
Marcelo Messias, Brazil
Ana Meštrović, Croatia
Ludovico Minati, Japan
Ch. P. Monterola, Philippines
Marcin Mrugalski, Poland
Roberto Natella, Italy
Nam-Phong Nguyen, USA
- Beatrice M. Ombuki-Berman, Canada
Irene Otero-Muras, Spain
Yongping Pan, Singapore
Daniela Paolotti, Italy
Cornelio Posadas-Castillo, Mexico
Mahardhika Pratama, Singapore
Luis M. Rocha, USA
Miguel Romance, Spain
Avimanyu Sahoo, USA
Matilde Santos, Spain
Hiroki Sayama, USA
Michele Scarpiniti, Italy
Enzo Pasquale Scilingo, Italy
Dan Selișteanu, Romania
Dimitrios Stamovlasis, Greece
Samuel Stanton, USA
Roberto Tonelli, Italy
Shahadat Uddin, Australia
Gaetano Valenza, Italy
Dimitri Volchenkov, USA
Christos Volos, Greece
Zidong Wang, UK
Yan-Ling Wei, Singapore
Honglei Xu, Australia
Xinggang Yan, UK
Massimiliano Zanin, Spain
Hassan Zargazadeh, USA
Rongqing Zhang, USA

Contents

Advanced Methods to Analyse the Complexity of the Brain

Nadia Mammone , Gaoxiang Ouyang , and Hamed Azami 
Editorial (2 pages), Article ID 8971891, Volume 2018 (2018)

Using Graph Theory to Assess the Interaction between Cerebral Function, Brain Hemodynamics, and Systemic Variables in Premature Infants

Dries Hendrikx , Liesbeth Thewissen , Anne Smits, Gunnar Nauelaers, Karel Allegaert ,
Sabine Van Huffel , and Alexander Caicedo
Research Article (15 pages), Article ID 6504039, Volume 2018 (2018)

Effect of EOG Signal Filtering on the Removal of Ocular Artifacts and EEG-Based Brain-Computer Interface: A Comprehensive Study

Malik M. Naeem Mannan , M. Ahmad Kamran, Shinil Kang, and Myung Yung Jeong 
Research Article (18 pages), Article ID 4853741, Volume 2018 (2018)

A Wavelet-Based Correlation Analysis Framework to Study Cerebromuscular Activity in Essential Tremor

Yifan Zhao , Ramon C. Laguna, Yitian Zhao , Jimmy Jiang Liu, Xiongxiang He, John Yianni,
and Ptolemaios G. Sarrigiannis
Research Article (15 pages), Article ID 7269494, Volume 2018 (2018)

Automatic Lateralization of Temporal Lobe Epilepsy Based on MEG Network Features Using Support Vector Machines

Ting Wu, Duo Chen, Qiqi Chen, Rui Zhang, Wenyu Zhang, Yuejun Li, Ling Zhang, Hongyi Liu,
Suiren Wan, Tianzi Jiang, and Junpeng Zhang 
Research Article (10 pages), Article ID 4325096, Volume 2018 (2018)

Automated Epileptic Seizure Detection in Scalp EEG Based on Spatial-Temporal Complexity

Xinzhong Zhu, Huiying Xu, Jianmin Zhao, and Jie Tian
Research Article (8 pages), Article ID 5674392, Volume 2017 (2018)

Editorial

Advanced Methods to Analyse the Complexity of the Brain

Nadia Mammone ¹, Gaoxiang Ouyang ², and Hamed Azami ^{3,4}

¹*IRCCS Centro Neurolesi Bonino-Pulejo, Messina, Italy*

²*Beijing Normal University, Beijing, China*

³*University of Edinburgh, Edinburgh, UK*

⁴*Massachusetts General Hospital, Harvard University, Cambridge, MA, USA*

Correspondence should be addressed to Nadia Mammone; nadia.mammone@unirc.it

Received 30 July 2018; Accepted 30 July 2018; Published 8 October 2018

Copyright © 2018 Nadia Mammone et al. This is an open access article distributed under the Creative Commons Attribution License, which permits unrestricted use, distribution, and reproduction in any medium, provided the original work is properly cited.

The brain generates bioelectromagnetic fields due to the intra- and extracellular currents associated with the interaction between neurons. Brain activity is also associated with changes in the cellular metabolism and blood flow. Such bioelectromagnetic and metabolic activities can be detected through proper neurophysiological measurements. The spatio-temporal dynamics of the recorded neurophysiological signals are closely related to the age of a subject, to her/his state of consciousness, to cognitive activities, to the execution of active or passive task (e.g., hyperventilation or external stimulation), to the presence of neurological disorders, to the possible use of medical treatment, and so on. Among the possible neurophysiological acquisition systems, Electroencephalography (EEG), Electrocorticography (ECoG), Magnetoencephalography (MEG), Local Field Potentials (LFP), Event-Related Potential (ERP), Computed Tomography (CT), and functional Magnetic Resonance Imaging (fMRI) are more popular. The data recorded by the abovementioned techniques deeply differ from each other; however, they all are a representation of the output of the complex system that generated them: the brain. The brain is a complex system at least from two perspectives: globally, since it consists of several components dynamically interacting with each other, and locally, as the temporal complexity analysis of univariate time series resulting from a single channel recording can provide information about the local dynamics. Intuitively, complexity in signals or images is associated with meaningful structural richness. In the complexity literature, it is hypothesized that healthy

individuals or systems correspond to more complex states due to their ability to adapt to adverse conditions, exhibiting long range correlations, and rich variability at multiple scales, whereas aged and diseased subjects or systems may present complexity alterations, depending on the disease. To quantify the complexity of signals, a number of univariate and multivariate multiscale entropy methods, nonlinear synchronization measures, complex network models, and many others were introduced. This special issue aimed at attracting relevant contributions, both methodological and applications, in the field of complexity analysis of neurophysiological data. It collected valuable contributions in the most varied fields of research ranging from deep brain stimulation (DBS) to brain computer interface (BCI).

In the paper “A Wavelet-Based Correlation Analysis Framework to Study Cerebromuscular Activity in Essential Tremor,” the issue of DBS in patients with severe essential tremor (ET) was addressed. Y. Zhao et al. proposed a novel framework to improve the reliability of correlation between LFP signals recorded from the brain and the tremulous electrical activity recorded through Electromyography (EMG). Polygraphic recordings, EEG/LFP/EMG, from two patients that underwent DBS surgery for medically refractory ET were analysed. The authors found a relationship between the thalamic local field potential recordings and the contralateral tremorogenic EMG oscillations at the frequency of the tremor and its first harmonic. Preliminary results endorse the hypothesis that the proposed methodology can identify the thalamic contacts to be selected

for high-frequency DBS stimulation, with the aim of achieving a better clinical outcome in comparison to the empirical DBS device programming.

In “Automated Epileptic Seizure Detection in Scalp EEG Based on Spatial-temporal Complexity,” a novel method is introduced to define a patient-specific detector based on spatial-temporal complexity analysis. The authors evaluated both permutation entropy (PE) and sample entropy (SE). The detectors were tested over a publicly available dataset achieving a 99% sensitivity by the use of PE. The proposed method also meets the requirements for real-time seizure detection.

In the paper “Automatic Lateralization of Temporal Lobe Epilepsy Based on MEG Network Features Using Support Vector Machines,” T. Wu et al., proposed a framework for the lateralization of temporal lobe epilepsy (TLE) using support vector machine (SVM) and weighted network metrics obtained from source-space MEG. It was illustrated that showed that MEG is an appropriate monitoring method for the lateralization of TLE. Additionally, it was found that MEG source space brain-network features can be effectively employed for determining the lateralization.

“Effect of EOG Signal Filtering on the Removal of Ocular Artifacts and EEG-Based Brain-Computer Interface: A Comprehensive Study” is a paper that addresses the issue of ocular artifacts contaminating EEG signals acquired for BCI applications. An optimized low-pass filtering may reduce the effects of electrooculographic (EOG) signals and improve the performance of BCI. The authors found that low-pass filtering at 6–8 Hz seems to be the optimal filtering range. Furthermore, motor imagery (MI) datasets were used to validate the results. Classification accuracy improved when EOG filtering was applied.

In the article “Using Graph Theory to Assess the Interaction between Cerebral Function, Brain Hemodynamics, and Systemic Variables in Premature Infants,” D. Hendrikx et al. showed the ability of graph theory in describing interactions between cerebral function, brain hemodynamics, and systemic variables using some data from a propofol dose finding and pharmacodynamics study in the vulnerable population of preterm infants. The results illustrated that propofol induces a decrease in the signal interaction up to 90 minutes after propofol administration. The clinical recovery phase was mainly determined by the EEG dynamics. Finally, a more pronounced loss in cerebral-systemic interactions with increasing propofol dose was found.

Conflicts of Interest

The authors declare that they have no conflicts of interest.

*Nadia Mammone
Gaixiang Ouyang
Hamed Azami*

Research Article

Using Graph Theory to Assess the Interaction between Cerebral Function, Brain Hemodynamics, and Systemic Variables in Premature Infants

Dries Hendrikkx ^{1,2}, Liesbeth Thewissen ^{3,4}, Anne Smits,^{3,4} Gunnar Naulaers,^{3,4}
Karel Allegaert ^{3,5,6}, Sabine Van Huffel ^{1,2} and Alexander Caicedo^{1,2}

¹Department of Electrical Engineering (ESAT), STADIUS, KU Leuven, Leuven, Belgium

²imec, Leuven, Belgium

³Department of Development and Regeneration, KU Leuven, Leuven, Belgium

⁴Department of Neonatology, UZ Leuven, Leuven, Belgium

⁵Department of Pediatric Surgery and Intensive Care, Erasmus MC-Sophia Children's Hospital, Rotterdam, Netherlands

⁶Department of Neonatology, Erasmus MC-Sophia Children's Hospital, Rotterdam, Netherlands

Correspondence should be addressed to Dries Hendrikkx; dries.hendrikkx@esat.kuleuven.be

Received 19 February 2018; Revised 9 April 2018; Accepted 9 May 2018; Published 9 August 2018

Academic Editor: Hamed Azami

Copyright © 2018 Dries Hendrikkx et al. This is an open access article distributed under the Creative Commons Attribution License, which permits unrestricted use, distribution, and reproduction in any medium, provided the original work is properly cited.

Graphs can be used to describe a great variety of real-world situations and have therefore been used extensively in different fields. In the present analysis, we use graphs to study the interaction between cerebral function, brain hemodynamics, and systemic variables in premature neonates. We used data from a propofol dose-finding and pharmacodynamics study as a model in order to evaluate the performance of the graph measures to monitor signal interactions. Concomitant measurements of heart rate, mean arterial blood pressure, arterial oxygen saturation, regional cerebral oxygen saturation—measured by means of near-infrared spectroscopy—and electroencephalography were performed in 22 neonates undergoing INSURE (intubation, surfactant administration, and extubation). The graphs used to study the interaction between these signal modalities were constructed using the RBF kernel. Results indicate that propofol induces a decrease in the signal interaction up to 90 minutes after propofol administration, which is consistent with clinical observations published previously. The clinical recovery phase is mainly determined by the EEG dynamics, which were observed to recover much slower compared to the other modalities. In addition, we found a more pronounced loss in cerebral-systemic interactions with increasing propofol dose.

1. Introduction

A graph is a structure that can be used to represent the relation between different objects. In this context, a graph can be thought of as a diagram which consists of a set of points, where some or all of them are joined by lines. Formally, the points of the graph are referred to as vertices or nodes, whereas the lines between them are called edges or links. In general, graphs can be used to describe a great variety of real-world situations [1]. Think, for example, of a social

network, where people are represented by nodes and the edges between the nodes are used to indicate friendship. Another example is a geographic network of cities, with an edge between two cities indicating a direct connection through a highway. In addition to the presence (or lack) of an edge connecting two nodes, extra measurements can be associated with the edges. These measurements are formally referred to as edge weights. In a social network, edge weights could be used to denote the strength of the friendship (acquaintances, close friends, ...). In a geographic network,

the weights can indicate the physical distance or the amount of traffic typically encountered on each road. Mathematically, this type of diagram corresponds to a weighted graph.

In the present analysis, weighted graphs are used to study the interaction of cerebral function, brain hemodynamics, and systemic variables in premature neonates. Multiple studies are available in the literature that studied the pairwise interactions between some of these variables. Caicedo et al. analysed the relation between mean arterial blood pressure (MABP) and regional cerebral oxygen saturation ($rScO_2$), measured by means of near-infrared spectroscopy (NIRS) [2]. The coupling between these two variables, defined using a transfer function approach, was found to be a measure to assess cerebral autoregulation. Semenova et al. examined the relation between MABP and electroencephalography (EEG) [3]. The authors documented that preterm infants with a high clinical risk index for babies (CRIB) score were found to be associated with a higher nonlinear coupling between EEG activity and MABP, quantified by means of mutual information. Tataranno et al. examined the relation between $rScO_2$ and EEG and found that increased oxygen extraction was related to spontaneous activity transients observed in the EEG [4]. In contrast to the studies mentioned above, we aim to analyse the interaction between cerebral and systemic variables using an extended multimodal approach, integrating three systemic variables: heart rate (HR), MABP and arterial oxygen saturation (SaO_2), $rScO_2$, and EEG.

This study is situated within the interdisciplinary field of network physiology, which analyses how diverse physiologic systems dynamically interact and collectively behave to produce distinct physiologic states and functions [5]. Moreover, the use of graphs enables a graphical representation of the interaction between the different physiological systems in time. This study shows for the first time a comprehensive model of different physiological processes comprising autoregulation, neurovascular coupling, or baroreflex, working at the same moment in time. In literature, most studies focus on these processes individually without taking into account the influence of the other processes. With the graph approach outlined in this paper, we try to show the different processes, their interaction, and the importance of the individual processes at each moment in time. To the best of our knowledge, this is a totally new mindset and way of showing the physiological interaction between cerebral function, brain hemodynamics, and systemic variables in newborn neonates.

The interaction between the different variables is studied using premedication by means of propofol as a model. Propofol (2,6 diisopropylphenol) is a short-acting anesthetic: it has a rapid onset of action and is generally short in duration. In neonates, however, it is documented that clinical recovery takes time [6]. In clinical practice, propofol is administered to the neonates as a single intravenous (IV) bolus. Propofol administration is frequently associated with a decrease in MABP in neonates [6–11], children [12], and adults [13–15]. Propofol distributes into the central nervous system and fat tissue immediately after intravenous dosing, which explains the rapid onset of this anesthetic drug. In a secondary phase, propofol is redistributed into

the circulation, which leads to vasodilation. Combined with the blunted reflex tachycardia, this can result in hypotension [10]. Therefore, a decrease in MABP is observed up to one hour after administration of propofol in neonates [8]. Premedicating neonates with propofol generally causes a modest and short-lasting decrease in HR, SaO_2 , and $rScO_2$, as opposed to the longer-lasting and more pronounced decrease in MABP [8], [11, 16, 17]. In addition, the discontinuity pattern of the EEG is also influenced by propofol, which induces a reversible state of diminished responsiveness behaviorally similar to quiet (nonrapid eye movement (NREM)) sleep [18]. During quiet sleep, the EEG of premature neonates shows a spontaneous, physiological discontinuity of electrical activity, characterized by higher amplitude, lower-frequency EEG rhythms (tracé alternant (TA)) [19, 20]. This phenomenon is generally referred to as burst suppression, which corresponds to an increase in interburst interval (IBI) duration [21, 22]. Moreover, a larger IBI duration is associated with smaller FTOE values, which indicate lower brain energy consumption [23].

This paper is structured as follows. Section 2 describes the dataset used in the present analysis. Section 3 discusses the methods, which include EEG processing, the construction of the graph models, and the definition of features computed from the graph models to quantify the strength of the effect of propofol on these interactions. Section 4 presents the results of the paper, which are extensively discussed in Section 5. Finally, Section 6 summarizes the conclusions.

2. Dataset

The dataset used in the present analysis was collected as part of a study on propofol dose selection by Smits et al. [6]. In the study, 50 neonates were sedated using propofol as part of an endotracheal intubation procedure. All subjects in the group of study were recruited at the NICU of the University Hospitals Leuven, Gasthuisberg. The trial was registered on ClinicalTrials.gov NCT01621373, and ethical approval was provided by the ethical committee at the University Hospitals Leuven.

Due to incomplete data and overly noisy channels found in 28 neonates, only 22 of the 50 neonates are included in this study. These neonates were all sedated using propofol as part of an INSURE (intubation, surfactant, and extubation) procedure. The neonates are characterized by median (range) postmenstrual ages (PMA) of 30 (26–35) weeks and a median (range) dose of propofol (Diprivan 1%; AstraZeneca, Brussels, Belgium) of 1.0 (0.5–4.5) $mg \cdot kg^{-1}$. In the present analysis, the neonates are stratified into three groups, based on PMA, since this is a major covariate of propofol clearance in the absence of variability in postnatal age (PNA) [24]. These groups are generally referred to as extremely preterm (group 1: <28 weeks PMA), very preterm (group 2: 28–31 6/7 weeks PMA), and moderate to late preterm (group 3: 32–36 6/7 weeks PMA) [25]. Most of the neonates have a PNA of 1 day. For details regarding the composition of the patient groups, the PNA of the patients, and the doses of propofol administered to the subjects of each group, see Table 1. More information

TABLE 1: Stratification of the neonates into three age groups, based on postmenstrual age (PMA) in weeks. For each group, the number of patients, postnatal age (PNA) of the patients, and propofol dose values administered to the subjects in the group are presented.

	Group 1 Extremely preterm <28 weeks	Group 2 Very preterm 28–31 6/7 weeks	Group 3 Moderate to late preterm 32–36 6/7 weeks
Number of patients	5	13	4
PNA (days)			
Median	1	1	1
Range	1-2	1-2	1-3
Dose (mg·kg ⁻¹)			
Median	1.0	1.0	2.75
Range	0.5–1.5	0.5–2.5	1.0–4.5

about the clinical characteristics of the subjects can be found in the original paper by Smits et al. [6].

Practices on propofol dosing, particularly in highly vulnerable premature neonates, are not standardized and vary between different NICUs. Multiple studies, however, indicate that propofol dose values of 2.0 to 2.5 mg·kg⁻¹ should be used as preintubation medication in premature neonates [9–11, 16]. The dataset used in the present analysis was collected with the aim to find the median effective dose (ED50) of propofol for sedation. Therefore, lower values of starting propofol dose were used, as indicated in Table 1. More specifically, administered dose ranges from 0.5 to 4.5 mg·kg⁻¹ [6]. In general, the oldest neonates were sedated using higher propofol doses compared to the youngest neonates, as can be observed from Table 1.

The multimodal dataset used in this study consists of concomitant measurements of five signal modalities, comprising HR, MABP, SaO₂, rScO₂, and EEG, recorded from 5 minutes before propofol administration up to 10 hours after. For each neonate, a 6-hour long segment of multimodal data was considered in the analysis, where $t=0$ was aligned with the moment of propofol administration. This length was defined based on the shortest recording found in the dataset. Thus, all signals were shortened to six hours for all patients in order to provide uniformity. Moreover, the use of a long time window of 6 hours allows focusing on the regime of interest, since we can study the effect of propofol together with the recovery of the neonates from the drug. Propofol is a three-compartment drug, characterized by a short α and β (median estimates of 1 and 13 minutes, resp.) and a long γ half-life (median estimate of 350 minutes) [26, 27]. The pharmacodynamic effects are primarily associated with the first (α) and second (β) exponential half-life, which indicates that the effect of propofol at the end of the analysis window is minimal. This is confirmed by Smits et al., Vanderhaegen et al., and Ghanta et al., who all observed a clinical recuperation from single intravenous bolus propofol administration within the first hour in neonates [6, 8, 16]. Therefore, the analysis window is divided in two parts: the first 3-hour long time window is used to study the response of the neonates to propofol and the intubation procedure, while the last 3 hours are used as reference. Figure 1 presents an example of

a 6-hour long segment of multimodal data for one neonate from the group of study.

The systemic variables (HR (beats/min), MABP (mmHg), and SaO₂ (%)) were measured with IntelliVue MP70 (Philips, Eindhoven, The Netherlands) with a Nellcor pulse oximeter. These variables were recorded continuously with a sampling frequency of 1 Hz (Rugloop; Demed, Temse, Belgium). All 22 neonates incorporated in the present analysis had an arterial line, which enabled an invasive measurement of MABP. NIRS was used to measure rScO₂ (%) noninvasively with INVOS 5100 using a cerebral neonatal OxyAlert NIRS sensor (Covidien, Mansfield, Massachusetts). As for the systemic variables, the sampling frequency for rScO₂ is equal to 1 Hz. Cerebral functioning was assessed using a one-channel EEG (μ V). The EEG was measured between the C3 and C4 electrodes according to the international 10–20 system with a sampling frequency of 100 Hz (Olympic Cerebral Function Monitor 6000, Natus). EEG segments with impedance values exceeding 10 k Ω were removed from the raw EEG signal [28]. In addition, movement artifacts identified as rapid changes in the impedance measurement were detected and also removed from the raw EEG signal.

3. Methods

3.1. Running Interburst Interval Duration. In general, EEG signals of premature neonates alternate between periods of activity, called bursts or burst intervals (BIs), and periods of suppressed activity, referred to as IBIs. Thus, the morphology of neonatal EEG is discontinuous, as indicated by the IBIs. However, this discontinuous pattern evolves towards a more continuous trace with increasing PMA. Therefore, some studies have investigated the use of the length of the IBIs as a marker for maturation [29, 30].

Due to the different temporal characteristics between the EEG and all other signal modalities, the EEG signals are processed in order to obtain surrogates for brain activity in a similar time frame as the other measured signals. The EEG signal is segmented in burst and IBI segments using an in-house algorithm based on the line length [31]. The root mean squared (RMS) value and the duration in time for burst and IBIs in overlapping windows

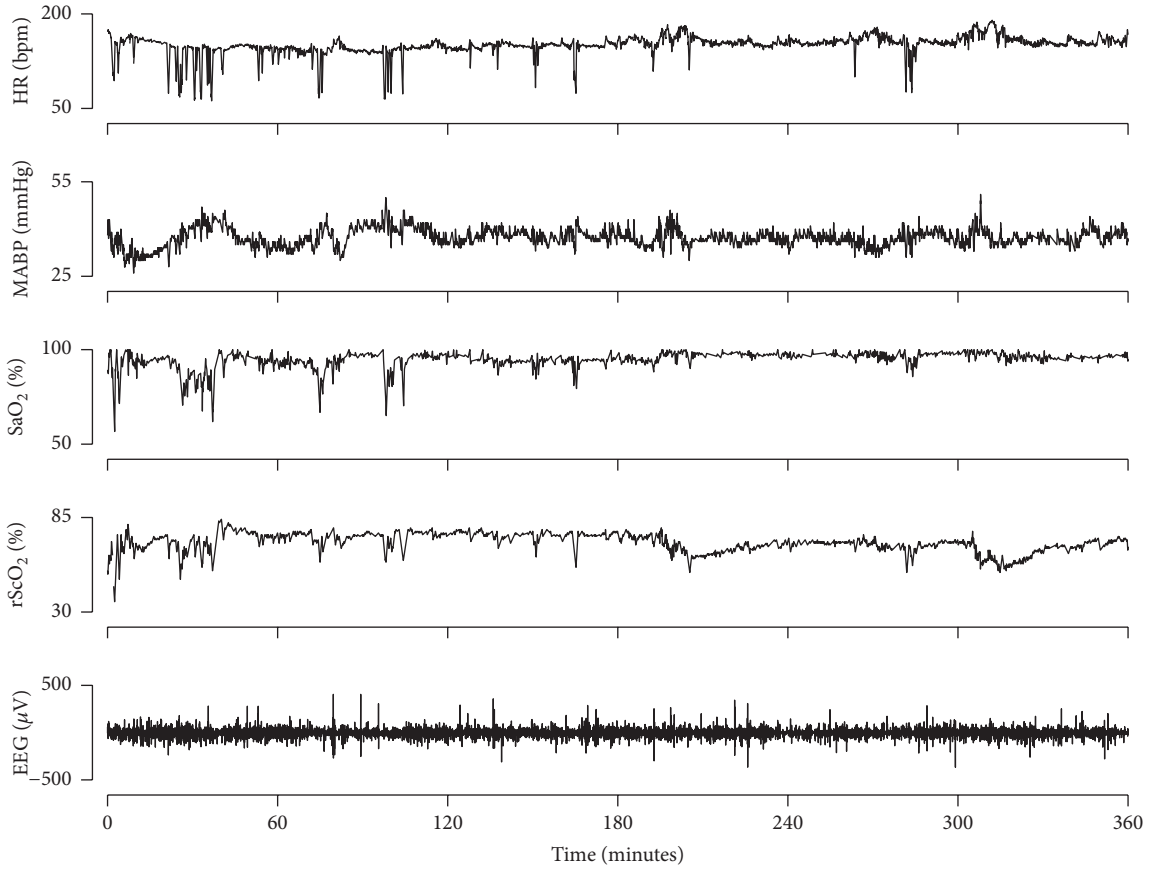


FIGURE 1: Illustration of the 5 signal modalities used to construct graph models for the neonates. A 6-hour long segment of multimodal data is presented for one neonate in the group of study (PMA 27 weeks, $0.5 \text{ mg}\cdot\text{kg}^{-1}$).

of two minutes are used as a surrogate for EEG. The running window is shifted in one second, producing a new score every second. In this way, the sampling frequency of the surrogate measures for EEG has the same sampling frequency as the other signal modalities.

In total, five features are computed from the discontinuous neonatal EEG: running RMS values of the original EEG, BIs, and IBIs and running duration values of the BIs and IBIs. In this paper, we only report the results using the running IBI duration, since this is a very robust measure for EEG activity, and thus cerebral metabolism, as validated by our group in a previous study [31]. In addition, this measure is highly interpretable. It is important to note, however, that the other EEG features indicate similar results, since the different feature values are highly related. An example of the five EEG features is presented in Figure 2.

3.2. Graph Model Developed for This Study. In order to quantify the common dynamics of the different signal modalities, and changes thereof due to propofol, the interaction between the variables is modeled using a graph, as illustrated in Figure 3. In general, a graph is defined by a nonzero number of vertices (nodes) and a number of edges (links, connections) between these nodes. The model for the neonates is constructed using a complete graph. A complete graph is characterized by the presence of an edge between all the

vertices. The vertex set V of the graph consists of $n = 5$ vertices, corresponding to the 5 signal modalities measured in the present analysis, that is,

$$V = \{v_{\text{HR}}, v_{\text{MABP}}, v_{\text{SaO}_2}, v_{\text{rScO}_2}, v_{\text{EEG}}\}. \quad (1)$$

A complete graph with n vertices has $m = n(n-1)/2$ edges. Therefore, the edge set E of the graph considered here consists of 10 edges. The vertices of the graph model defined in (1) are connected by edges. These edges are defined by the corresponding edge weight values, which are generally used to assess the strength of the connection between a pair of vertices.

The topology of the complete graph described in (1) is assumed to be fixed in time. The edge weights, however, change in time, which we hypothesize to reflect the changes in the interaction between the different signals. In order to compute the graph models, the signals are first normalized to $N(0,1)$, since we are interested in the assessment of common dynamics (signal trends in time) and not absolute values of the signals. Next, the edge weights are computed using a 15-minute long running window of multimodal data, which is shifted by 1 minute (14 minutes overlap). Thus, new edge weight values are computed every minute. Finally, two types of interaction curves are extracted from the graph models: the pairwise interaction between two signal modalities,

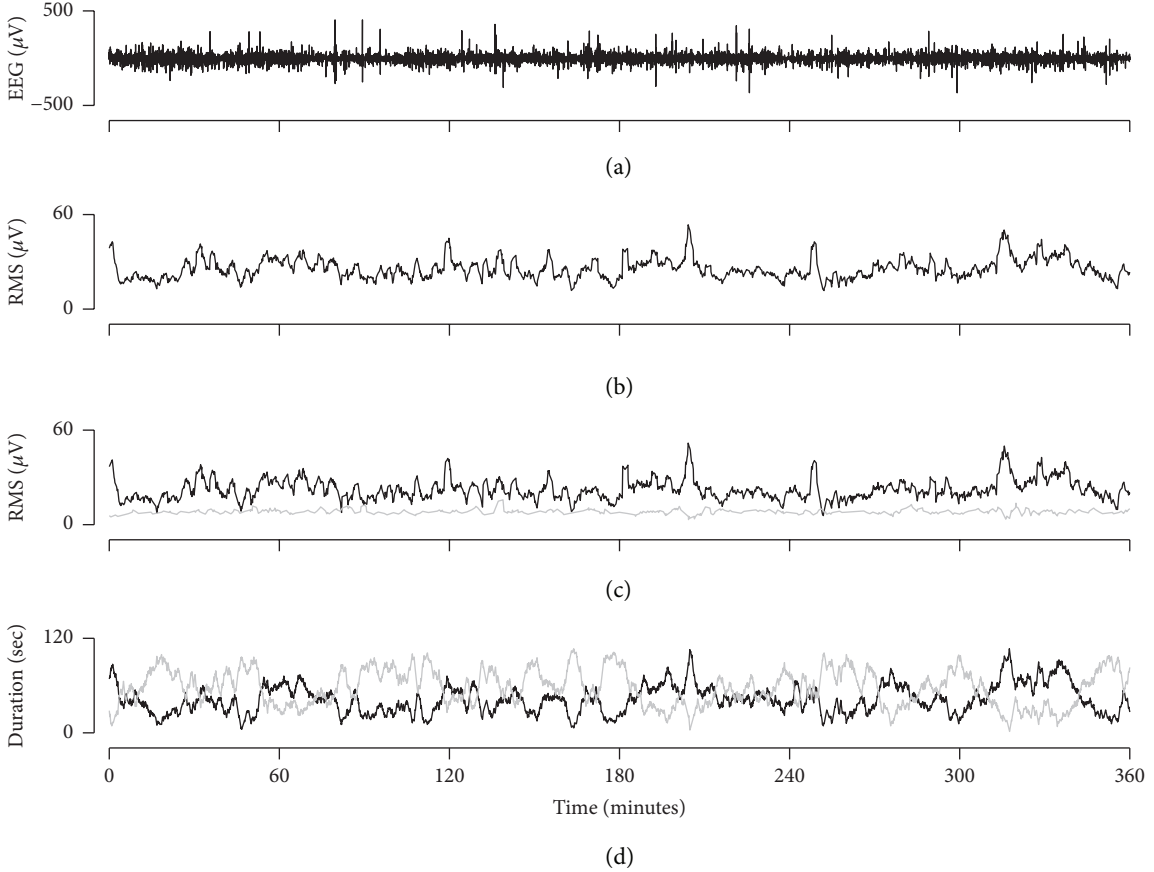


FIGURE 2: Illustration of the features computed from the EEG signal. (a) illustrates a 6-hour long EEG segment for one neonate in the group of study (PMA 27 weeks, $0.5 \text{ mg}\cdot\text{kg}^{-1}$). (b) illustrates the running RMS value. (c) and (d) illustrate the running RMS and running duration values for BIs (black) and IBIs (gray), respectively.

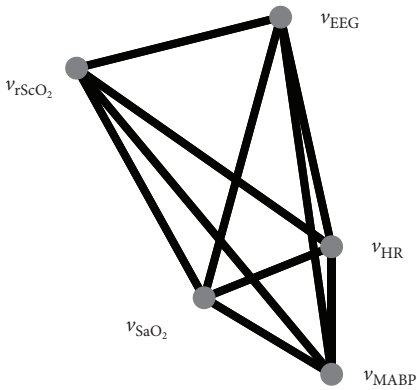


FIGURE 3: Physiological network representing the interaction between 5 signal modalities recorded on a neonate after propofol administration. The graph consists of 5 vertices, corresponding to the signal modalities. In addition, an edge is present between every pair of nodes (complete graph). Each edge is defined by a weight value that represents the interaction between the corresponding signal modalities.

represented by the time course of the corresponding edge weight, and the overall signal interaction, represented by the graph average degree (see Section 3.4).

In the present analysis, weight values are used to denote the interaction between two vertices, that is, two signal modalities. If two modalities are characterized by common nonlinear interactions, they follow the same trends in time. We compute the pairwise similarity using two different similarity measures. Consequently, we generate two graph models for each neonate. Both similarity measures use the radial basis function (RBF) kernel, which is a nonlinear similarity measure. As such, the similarity of the different signals is assessed in a possibly infinitely dimensional feature space, defined by the nonlinear map ϕ . However, the similarity in this feature space is computed implicitly using the RBF kernel function. The first similarity measure $k_T(x_i, x_j)$ uses the raw signals in the RBF kernel and is thus defined as

$$k_T(x_i, x_j) = \phi(x_i)^\top \phi(x_j) = \exp\left(-\frac{\|x_i - x_j\|_2^2}{\sigma^2}\right), \quad (2)$$

where x_i and x_j represent two segments of multimodal data [32] (subscript T indicates that time domain signals are used for the Euclidean distance in the exponent of the RBF kernel). In the present analysis, x_i and x_j are segments with a length of 15 minutes, as mentioned before. The similarity $k_T(x_i, x_j)$ is bounded by 0 (absence of common interactions) and 1 (exact

common interactions). The signal similarity computed by (2) is a function of the Euclidean distance between input signals. Consequently, it highly depends on signal amplitudes and can be affected by delays between the signals. A graph model computed using the similarity measure $k_T(x_i, x_j)$ is denoted as G_T .

The second similarity measure uses the power spectral density (PSD) of the signals in the RBF kernel. Thus, the time input data is transformed to the frequency domain, before computing the RBF kernel function. Mathematically, this similarity measure $k_F(x_i, x_j)$ is defined as

$$k_F(x_i, x_j) = \exp\left(-\frac{\|S_{x_i} - S_{x_j}\|_2^2}{\sigma^2}\right), \quad (3)$$

where S_{x_i} and S_{x_j} represent the PSD of input signals x_i and x_j (length of 15 minutes), respectively (subscript F indicates that frequency domain signals are used for the Euclidean distance in the exponent of the RBF kernel). The PSD is computed using Welch's method using overlapping subwindows of 5 minutes in order to reduce the noise in the PSD estimate (with use of Hamming window, overlap of 4 minutes and 59 seconds). Note that the kernel presented in (3) is a valid positive definite kernel, since the input data is transformed before application of the kernel function. As before, the similarity defined by $k_F(x_i, x_j)$ is bounded by 0 and 1. The transformation to the frequency domain allows to include time-delayed signal interactions and interactions of opposite sign, in contrast to $k_T(x_i, x_j)$ which only takes into account instantaneous amplitude interactions. In physiological systems, it is possible that if one signal increases (decreases), another signal decreases (increases) to maintain homeostasis and that this interaction is not instantaneous but delayed. A graph model computed using the similarity measure $k_F(x_i, x_j)$ is denoted as G_F .

3.3. Kernel Tuning. In order to compute the similarity measure, the bandwidth σ of the RBF kernel should be tuned, that is, optimized to avoid kernel overfitting and underfitting. In the present analysis, the similarity measures $k_T(x_i, x_j)$ and $k_F(x_i, x_j)$ both depend on this parameter σ . The optimization procedure is the same for both similarity measures. Therefore, it is outlined in terms of $k(x_i, x_j)$, which represents the two similarity measures. The strategy used to select the kernel bandwidth for the present analysis considers kernel matrix Ω , which is defined as

$$\Omega_{ij} = k(x_i, x_j), \quad i, j = 1, \dots, n. \quad (4)$$

Note that the kernel matrix Ω is defined by the kernel bandwidth σ through the definitions presented in (2) and (3). The kernel bandwidth σ is tuned by maximizing the Shannon entropy of kernel matrix Ω . The Shannon entropy $H(\Omega)$ is defined as

$$H(\Omega) = -\sum_k p_k \log_2 p_k, \quad (5)$$

where p_k is equal to the probability of seeing the k th possible element of matrix Ω . The entropy is thus determined by estimation of the probability density function (PDF) of matrix Ω . By maximizing the Shannon entropy, we try to obtain a uniform distribution of the values in the kernel matrix, and therefore, we avoid overfitting as well as underfitting.

The kernel bandwidth is tuned for each neonate individually. The tuned bandwidth is denoted as σ_{opt} . The following optimization problem is defined to estimate σ_{opt} :

$$\sigma_{\text{opt}} = \max_{\sigma} H(\Omega_C), \quad (6)$$

with

$$\Omega_C = [\Omega_1 \ \Omega_2 \ \dots \ \Omega_N], \quad (7)$$

where Ω_C is a collection of kernel matrices, computed from all the signal segments recorded per neonate. Thus, a collection of kernel matrices is computed from the 6-hour long data segment instead of only one kernel matrix in the optimization procedure. If we would consider only one kernel matrix per neonate, it would only contain 25 entries, since the kernel matrix is a 5×5 matrix. Clearly, this is not enough data to estimate a robust PDF. Therefore, to solve this problem, we assume that the graph model does not change and that it is situated in the same nonlinear subspace throughout the 6-hour long analysis window. This assumption indicates that σ_{opt} should be uniform throughout the analysis window and that σ_{opt} can be computed using a concatenation of kernel matrices Ω_C , as defined in the optimization problem in (6) and (7).

Figure 4 illustrates the optimization procedure in a schematic way. The original data segment of 6 hours was segmented into nonoverlapping segments of 15 minutes. Thus, $N = 24$ signal segments of 15 minutes were defined. For each of these segments l , kernel matrix Ω_l was computed and all these kernel matrices Ω_l were concatenated as indicated in (7). The use of a collection of kernel matrices allows to estimate the probability density function, and consequently, the Shannon entropy. Therefore, $H(\Omega_C)$ is characterized by one global maximum. For the group of study, median (range) values of σ_{opt} are 27 (26–29) and 94 (86–113) for $k_T(x_i, x_j)$ and $k_F(x_i, x_j)$, respectively.

3.4. Graph Measures. In order to assess the overall interaction of the multimodal dataset, the average degree of the graph is used. This section introduces the adjacency matrix \mathbf{A} of a graph, the degree d_i of a vertex, and the average degree $\delta(G)$ of a graph G .

3.4.1. Adjacency Matrix. A weighted graph G consists of a nonempty finite set V of elements called vertices v_i (or nodes) and a finite set E of distinct unordered pairs of distinct elements of V called edges w_{ij} (or links) [33]. Note that the edges of the graph are represented by their weights w_{ij} . The adjacency matrix \mathbf{A} is a matrix commonly used to define the graph G . The adjacency matrix \mathbf{A} denotes the presence of edges between the vertices v_i of V and their corresponding

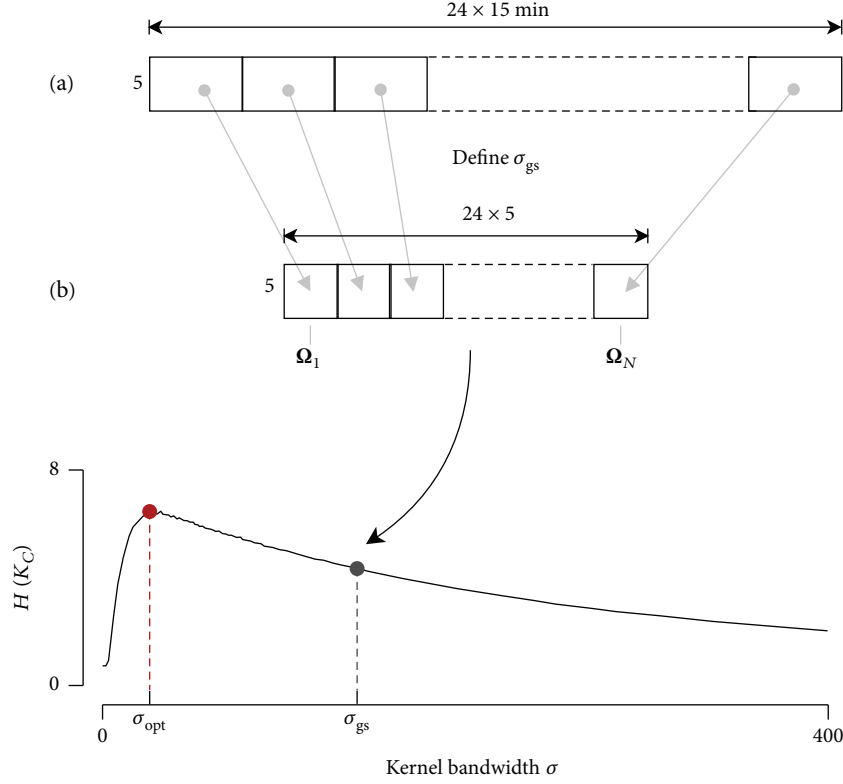


FIGURE 4: Method used to tune the kernel bandwidth σ . In (a), the data is segmented in nonoverlapping signal segments of 15 minutes. For all of these segments, a kernel matrix Ω_i is computed using a predefined σ_{gs} (4). All the individual kernel matrices Ω_i are concatenated in Ω_C , which is depicted in (b). Next, the Shannon entropy of Ω_C is computed. This procedure is repeated for a range of σ values. The σ value associated with maximal $H(\Omega_C)$ is selected as the bandwidth for the kernel function.

weights. More precisely, the adjacency matrix \mathbf{A} is constructed as

$$\mathbf{A}_{ij} = \begin{cases} w_{ij}, & \text{if there is an edge between } v_i \text{ and } v_j, \\ 0, & \text{otherwise.} \end{cases} \quad (8)$$

3.4.2. Vertex Degree. The degree d_j associated with a vertex v_j of an undirected weighted graph G , with adjacency matrix \mathbf{A} , is defined as the sum of all edges incident to v_j :

$$d_j = \sum_{i=1}^n w_{ij} = \sum_{i=1}^n \mathbf{A}_{ij}, \quad (9)$$

where n is the number of vertices. Therefore, the degree d_j characterizes the connection strength of the vertex v_j with respect to the other vertices of the graph. In practice, the weights of the edges of a graph are often restricted to a predefined range, which is often normalized to $w_{ij} \in [0, 1]$. Considering normalized weights, the degree is bounded by 0 and $n - 1$, where n is the number of vertices of the graph, that is,

$$0 \leq d_j \leq n - 1 \quad \text{if } \forall i, j : w_{ij} \in [0, 1]. \quad (10)$$

If $d_j = 0$, vertex v_j is called an isolated vertex, since it is not connected to any other vertex of the graph. A vertex degree

$d_j = n - 1$ indicates a dominating vertex v_j , connected to all other vertices of the graph with edge weight equal to 1.

3.4.3. Average Degree. The average degree $\delta(G)$ of a graph G is defined as the mean value of all vertex degrees d_j

$$\delta(G) = \frac{1}{n} \sum_{j=1}^n d_j \quad (11)$$

and is a measure associated with the overall connectivity of the graph. Evidently, the bounds of $\delta(G)$ are equal to those of the individual vertex degree d_j defined in (10). Small values (close to 0) imply a weak connectivity, whereas high values (close to $n - 1$) indicate a very strong connectivity of the graph.

3.5. Features to Quantify Interaction Strength. In order to quantify the strength of the changes in signal interaction, two features are computed from the interaction curves: the normalized area S between the interaction curve and reference level and the maximal deviation Δ from the reference level. Both feature values are computed in a time frame from 0 to 90 minutes after propofol administration. Reference levels are defined as the median value of an interaction curve in a time frame from 180 to 360 minutes after propofol administration, as mentioned before. Normalization of S is done by dividing the area by the length of the time interval.

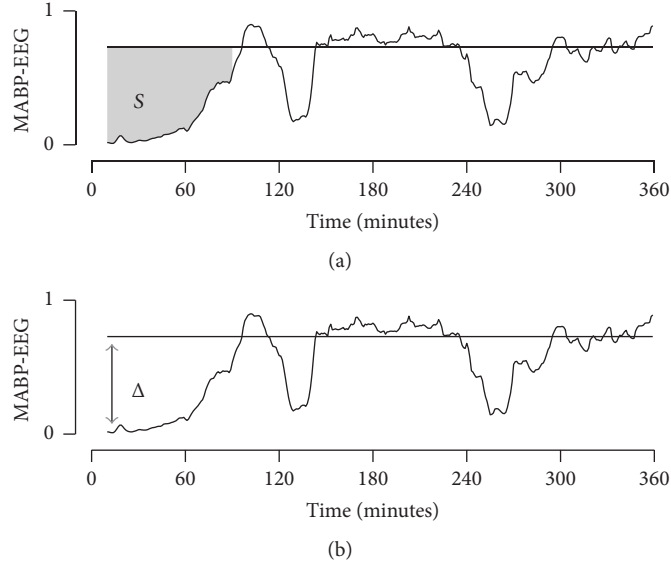


FIGURE 5: Features used to quantify the reduction in signal interaction strength: S (gray shaded area) (a) and Δ (gray arrow) (b). The feature values are illustrated for one neonate in the group of study (PMA 30 weeks, $2.5 \text{ mg}\cdot\text{kg}^{-1}$), where the pairwise interaction was computed using $k_T(x_i, x_j)$ (2). Feature values S and Δ are computed from 0 to 90 minutes, while the reference level is defined as the median value of the interaction curve from 180 to 360 minutes.

Note that S and Δ are bounded by 0 (no deviation from the reference level) and 1 (very strong deviation from the reference level). Figure 5 presents a graphical example of S (Figure 5(a)) and Δ (Figure 5(b)). The features are computed from the interaction curves in order to assess the effect of propofol on the dynamical interactions among the different signal modalities. In addition, we investigated how these features change with PMA and propofol dose.

In the present analysis, the relation between the feature values S and Δ (dependent variables) and PMA and propofol dose (predictor variables) is studied using linear regression models. The coefficient of determination R_i^2 is used to indicate the goodness of fit of the linear model (subscript i denotes the predictor variable i). In addition, the coefficient of partial determination was computed to account for the effect of both predictor variables at the same time. The significance of the coefficient of (partial) determination was assessed using the Monte Carlo permutation test with 10^5 repetitions. A $p < 0.05$ was defined to be statistically significant. A single asterisk, double asterisks, and triple asterisks denote a p value smaller than 0.05, 0.01, and 0.001, respectively.

3.6. Implementation. The analysis, the corresponding computations, and figures presented throughout this study are implemented using MATLAB Release 2016b (The MathWorks, Natick, Massachusetts). Graph theory analysis is performed using the MATLAB toolbox for network analysis, provided by MIT Strategic Engineering [34].

4. Results

4.1. MABP-EEG Pairwise Interaction. The interaction curves of MABP with respect to EEG after administration of propofol at $t=0$ minutes are illustrated in Figure 6. These

curves are computed using $k_T(x_i, x_j)$, defined in (2). The EEG signal is represented by the running IBI duration, as outlined in Section 3. From top to bottom, the interaction pattern is shown for the entire group of study ($N = 22$) and the individual age groups presented in Table 1. First, a pronounced loss in interaction is observed, followed by a gradual increase to a reference level, which is in general reached at $t=90$ minutes. Note that this loss in interaction is present among all of the signal modalities of the multimodal dataset, as indicated by the graphs in Figure 7. Figure 8 presents the relation between the features used to quantify interaction strength (S and Δ) and PMA and propofol dose. In addition to the data points, the least squares linear fit is defined (straight lines), together with the 0.95 percentiles of the linear fit (shaded area). The goodness of the linear fit is assessed using the coefficient of determination R_i^2 , which is equal to $R_A^2 = 0.09$ and $R_D^2 = 0.53$ for feature S and $R_A^2 = 0.17$ and $R_D^2 = 0.30$ for feature Δ (subscripts A and D are used to denote PMA and dose, resp.). Since PMA and dose are correlated (Pearson correlation coefficient $r_{AD} = 0.45$), we also define the coefficient of partial determination in order to account for the effect of both predictor variables on features S and Δ . Numerical values are equal to $R_{A|D}^2 = 0.002$ and $R_{D|A}^2 = 0.49$ for feature S and $R_{A|D}^2 = 0.05$ and $R_{D|A}^2 = 0.20$ for feature Δ . The statistical significance of the coefficients of (partial) determination is denoted in Figure 8. Finally, it is important to note that PMA and dose are not collinear using a linear model. This can be assessed by computing the variance inflatable factor (VIF) [35], which is equal to $VIF = 1.2572$. A VIF close to 1 indicates the lack of collinearity.

4.2. Overall Interactions. Figure 9(a) presents a comparison of the vertex degree d_i (in red is the interaction of modality

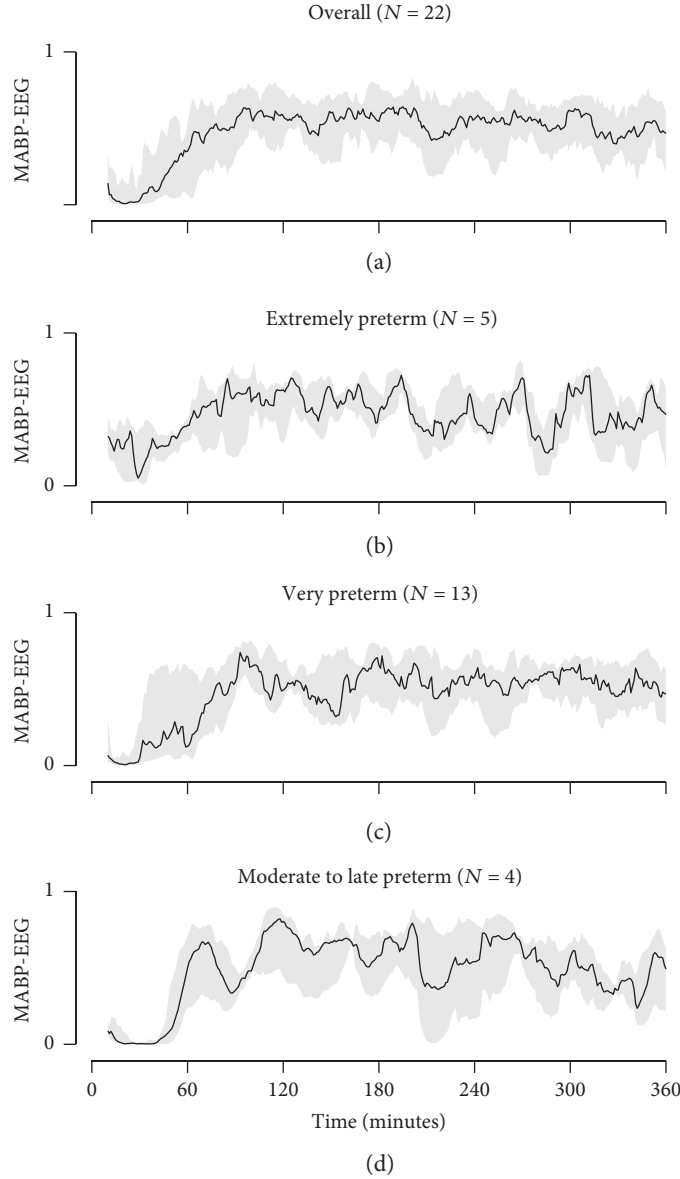


FIGURE 6: Signal interaction between MABP and EEG after administration of propofol at $t=0$ minutes. The signal interaction was computed using $k_T(x_i, x_j)$. A reduction in interaction is observed among the different signal modalities after the administration of propofol, with a slow recovery to the reference level. The black line and gray shaded area present the median and interquartile range (IQR), respectively.

i with respect to the other modalities) with the average degree $\delta(G_T)$ (in black is the average interaction of all signal modalities) for all of the signal modalities after administration of propofol at $t=0$ minutes. The curves are computed from graph models constructed using the similarity measure $k_T(x_i, x_j)$ (2). The results are presented for the whole group of study ($N=22$). Propofol-induced loss of interaction among the signals is associated with a drop in $\delta(G_T)$. The drop in average graph degree can also be observed in Figure 7, which illustrates the graph model for one neonate in the group of study at different time instances. As shown in Figure 9(a), the $\delta(G_T)$ value is highly determined by d_{MABP} during the first 30 minutes. Indeed, the MABP vertex degree is considerably lower compared to the degree of the other

modalities in this time frame. From 30 minutes onwards, the increase of $\delta(G_T)$ to the reference level is highly influenced by d_{EEG} , which is associated with the slowest recovery in signal dynamics.

Figure 9(b) shows the vertex degree d_i (red) with the graph average degree $\delta(G_T)$ (black) after propofol administration at $t=0$ for the graph models constructed using the second similarity measure, that is, $k_F(x_i, x_j)$ (3). As before, the results are presented for the whole group of study ($N=22$). A reduction in interaction can be observed after propofol administration, which is in agreement with the results of Figure 9(a). Again, MABP is observed to be the contributing factor in the propofol-induced loss of interaction during the first 30 minutes after propofol administration.

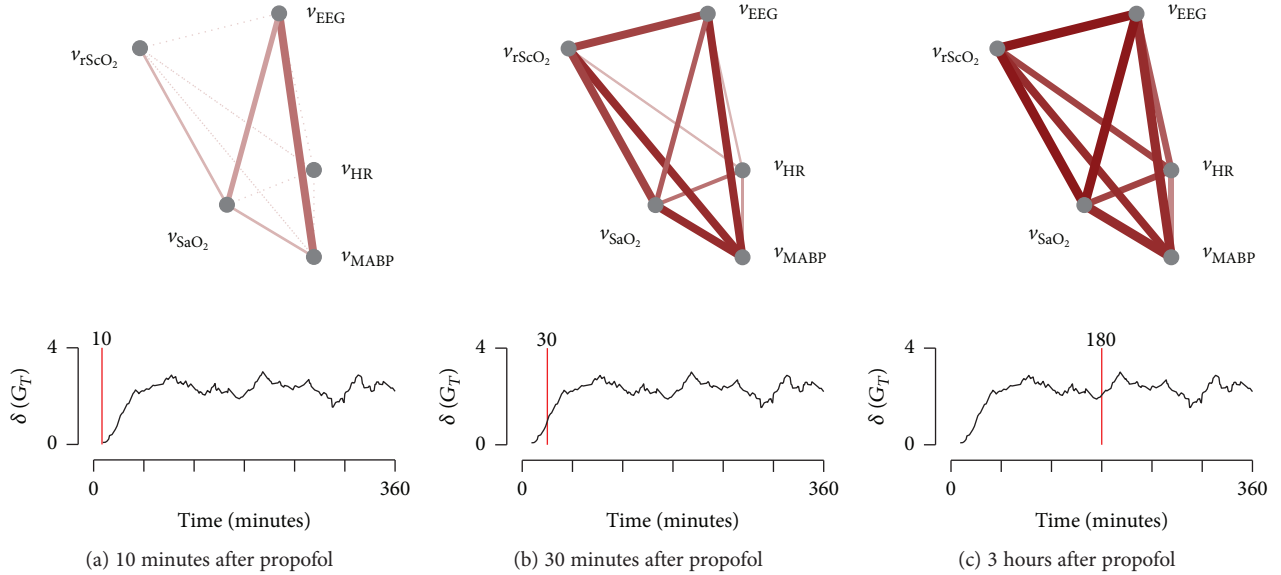


FIGURE 7: Changes in the physiological network, assessed using a graph model G_T , for one neonate in the group of study (PMA 30 weeks, $1.0 \text{ mg}\cdot\text{kg}^{-1}$) at three different time instances: plots (a), (b), and (c) illustrate the edge weights for $t=10$, 30, and 180 minutes after propofol administration, respectively. The graph model was constructed using $k_T(x_i, x_j)$ defined in (2). Under each graph, the average graph degree $\delta(G_T)$ is presented in a time frame starting right after propofol administration ($t=0$) up to 6 hours after. The average graph degree measures the average connection strength of the graph edges. From (a) to (c), the edge weights increase, which translates in an increased $\delta(G_T)$.

Indeed, this vertex is associated with the lowest degree values during this time frame. From 30 minutes onwards, the increase of $\delta(G_T)$ is again influenced by EEG dynamics. This effect is however less pronounced compared to the observation of Figure 9(a). In general, the results from $k_T(x_i, x_j)$ and $k_F(x_i, x_j)$ are similar, which might indicate that time delayed and/or interaction of opposite signs are not present in our dataset or that the influence of those interactions is not relevant, probably due to the length of the analysis window (15 minutes) that we used in the analysis.

5. Discussion

In the present analysis, we study how different physiologic systems dynamically interact and collectively behave after a propofol bolus administration in preterm neonates. These physiologic systems are presented by the different signal modalities under study. Note that we focus on the interaction between the brain and the cardiovascular system. This study can therefore be situated in the interdisciplinary field of network physiology [5].

Results indicate that propofol causes a change in the dynamical interactions between the different signals up to 90 minutes after propofol administration. The strength of this effect was observed to be mainly determined by propofol dose. In addition, the recovery phase was observed to be mainly determined by EEG dynamics, due to a much slower recovery to the reference level compared to the other signal modalities.

5.1. MABP-EEG Pairwise Interaction. Sedation of neonates using propofol induces a reduction in the interaction

between MABP and EEG (Figure 6), with only a slow, gradual increase back to the reference level. The most pronounced decrease in interaction pattern is associated with the oldest neonates in the group of study (moderate to late preterm): a strong loss of interaction is observed during the first 60 minutes after propofol administration, followed by a brisk increase back to baseline (Figure 6(d)). This pattern clearly differs from that of the younger neonates (extremely to very preterm), which are characterized by a less-pronounced reduction in interaction and a more gradual increase back to reference levels (Figures 6(b) and 6(c)).

Two possible indicators for the observed difference in signal interaction patterns are proposed. Both indicators are based on signal amplitude changes, since the signal interaction measure $k_T(x_i, x_j)$ highly depends on signal amplitudes. Firstly, the discontinuity pattern of neonatal EEG changes with age. Especially, the oldest neonates (moderate to late preterm) are characterized by a much more continuous EEG pattern (tracé continue) compared to the younger neonates (extremely to very preterm; tracé discontinue) [30]. A more continuous EEG can result in a more pronounced increase in IBI duration after propofol, potentially explaining the more pronounced loss in signal interaction observed among the oldest neonates in the group of study. Secondly, Simons et al. observed a higher incidence of hypotension with increasing dose of propofol [10]. In this study, higher doses were administered to older neonates, as demonstrated by Table 1. Evidently, a more pronounced impact on MABP can be responsible for a stronger loss in signal interaction.

Since PMA and propofol dose (predictor variables) are correlated ($r_{AD} = 0.45$), the influence of each factor on the resulting signal interaction pattern is assessed using features

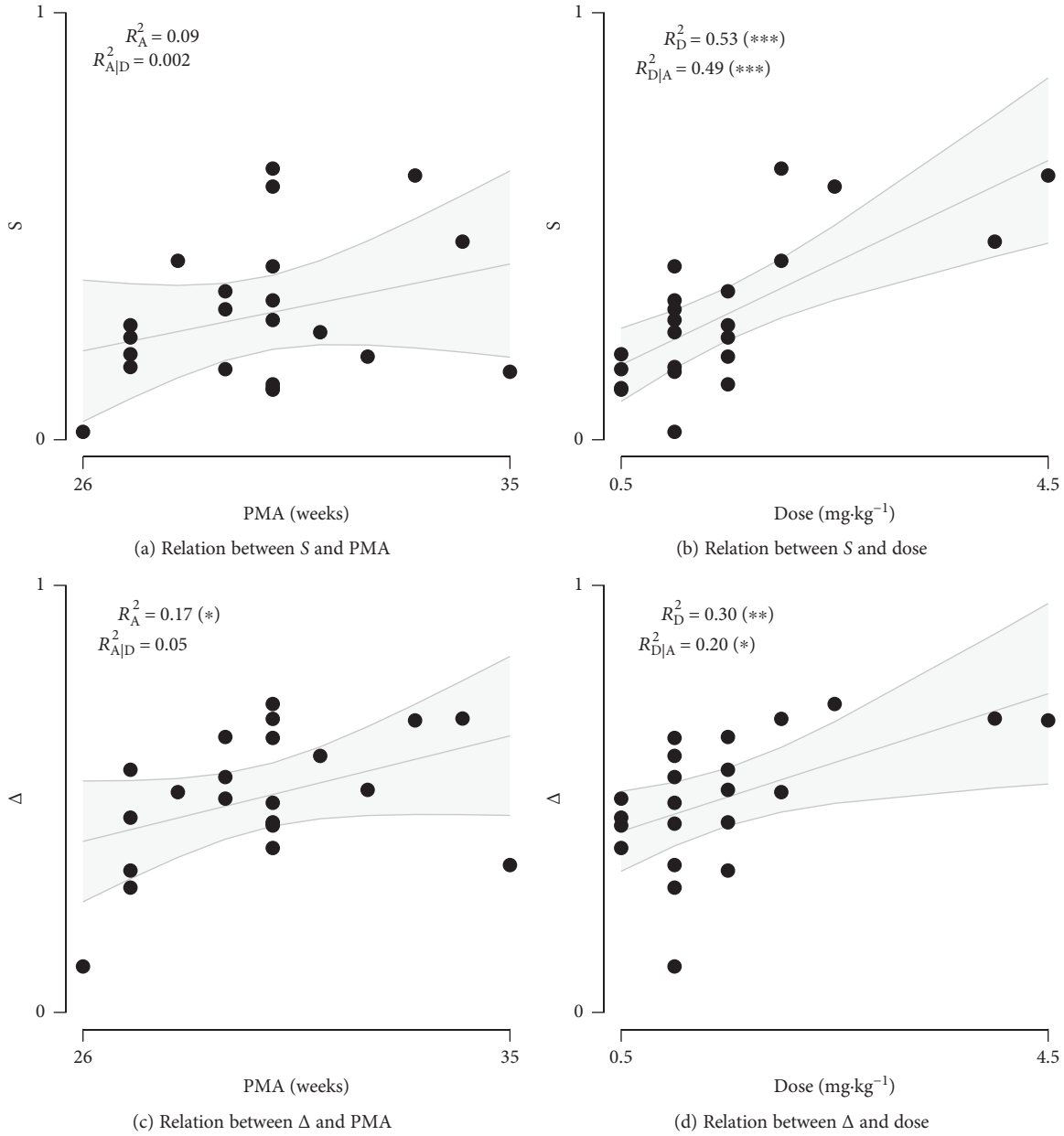


FIGURE 8: The relation between features S and Δ , computed from the MABP-EEG interaction curves presented in Figure 6, and PMA and propofol. The data points and the linear least squares fit are depicted in black and gray, respectively. The shaded area indicates the 95-percent confidence bounds on the least squares fit. The coefficient of (partial) determination is indicated in each plot (subscripts A and D denote PMA and propofol dose, resp.). A single asterisk, double asterisks, and triple asterisks denote a p value smaller than 0.05, 0.01, and 0.001, respectively.

S and Δ (independent variables). Figure 8 presents the relation between these features and PMA and propofol dose. From Figure 8, it is clear that the influence of PMA on the independent variables is minimal, especially when taking into account the influence of the dose. Indeed, the coefficients of partial determination are very small for PMA. ($R_{A|D}^2 = 0.002$ and $R_{A|D}^2 = 0.05$ for S and Δ , resp.). This observation is confirmed by the fact that the coefficient of partial determination is only slightly smaller compared to the coefficient of determination for propofol dose, especially for feature S . Therefore, it is clear that the interaction

between MABP and EEG is mainly influenced by propofol dose. The difference in interaction pattern observed in Figure 6 is thus mainly caused by the difference in propofol dose administered to the neonates in the different age groups, and not by the difference in PMA.

5.2. Overall Interactions. The phase of sedation using propofol is characterized by a markedly different network structure compared to the reference phase, indicating a clear association between network topology and physiologic function. This is illustrated in Figure 7: after 10 minutes, the graph is

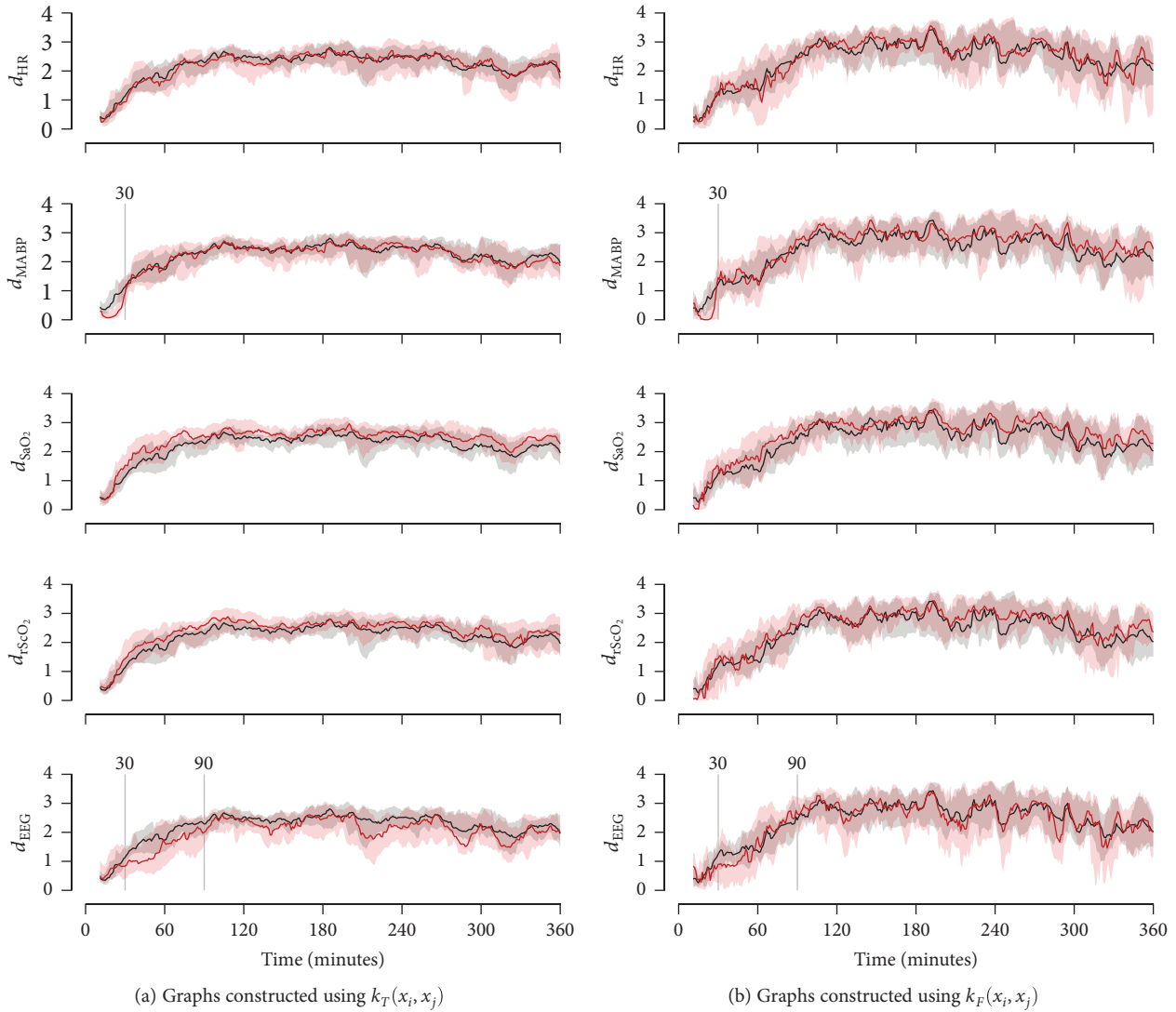


FIGURE 9: Comparing the vertex degree values (red) with the graph average degree (black) after administration of propofol at $t = 0$ minutes. The graph models were constructed using $k_T(x_i, x_j)$ (a) and $k_F(x_i, x_j)$ (b). The results are presented for the whole group of study ($N = 22$). From top to bottom, the vertex degree d_i is compared to the graph average degree $\delta(G)$ for HR, MABP, SaO_2 , rScO_2 , and EEG, respectively. d_{MABP} highly determines the signal interaction pattern during the first 30 minutes after propofol administration, while d_{EEG} highly influences the signal interaction pattern from 30 minutes to 90 minutes after propofol administration. After 90 minutes, the neonates are recovered from propofol, as indicated by the steady reference levels observed after 90 minutes.

weakly connected indicating a highly reduced overall signal interaction as opposed to the strongly connected graph observed at 3 hours after propofol administration.

MABP is observed to be the main contributor to the reduction in signal interaction during the first 30 minutes after propofol administration, as indicated in Figure 9. During this time frame, MABP strongly influences the strength of the overall interaction pattern, since the vertex degree is lower compared to the average graph degree. This effect can partly be explained as an amplitude effect. Indeed, propofol administration is associated with a pronounced decrease in MABP, which can last up to one hour after propofol administration, as described by many authors [6–8, 10]. The physiologic response of the other signal modalities is less affected by propofol compared to MABP. This pronounced change in

signal amplitude could explain why MABP highly influences the overall interactions, especially during the first 30 minutes after propofol administration. It is important to note, however, that the explained loss in signal interaction can not be entirely explained by only taking into account the signal amplitude and change thereof in time. Indeed, the propofol-induced loss in signal interaction is also observed in Figure 9(b), which presents the results using similarity measure $k_F(x_i, x_j)$. This measure assesses the interaction of the signals in the frequency domain.

For 30 minutes up to 90 minutes after propofol administration, the degree of the EEG signal is considerably lower than the degree values of the other modalities. As before, this finding can be observed in Figure 9. The EEG signal is the only signal associated with degree values below the average

degree, indicating the slow recovery of EEG dynamics with respect to the other modalities. Thus, MABP dynamics recover faster (generally recovered 30 minutes after propofol administration) compared to EEG dynamics (recovery takes up to 90 minutes after propofol administration). From a signal processing point of view, this might indicate the safety of propofol, since MABP can adapt to the needs of brain metabolism, once the EEG signal is recovered. It is important to note, however, that the neonates included in the present analysis were all sedated using propofol as part of an INSURE procedure. Surfactant causes a significant decrease in EEG activity, which can last up to 24 hours after surfactant administration, as described by van den Berg et al. [36]. Therefore, surfactant could also influence the decreased EEG interactions observed in Figure 9. The extent of this effect is however not clear at this point, since no control group without surfactant was available to compare with.

From 90 minutes after propofol administration onwards, the vertex degree and average degree curves presented in Figure 9 are characterized by stable reference levels. This indicates that the signal interaction pattern is restored after propofol administration.

6. Conclusions

In this study, we have shown that graph theory can be used to assess changes in signal interaction and that the resulting graph models can be used to study the difference between distinct physiologic states.

Moreover, for our propofol case study, we derived that the overall signal interaction pattern after propofol administration is highly influenced by both MABP and EEG. The MABP signal is the main contributor to the loss in signal interactions during the first 30 minutes after propofol, due to the strong decoupling of MABP dynamics with respect to the other signal modalities, while the EEG signal highly influences the interaction pattern thereafter. This finding indicates that MABP dynamics recover first, followed by a much slower recovery of the EEG signal, meaning that MABP dynamics are recovered while EEG metabolism is still down. Thus, when EEG dynamics recover, MABP can adapt to supply new needs of the brain in order to sustain its function.

Propofol affects signal dynamics with an overall recovery time of around 90 minutes, as assessed by the graph average degree. After 90 minutes, these curves are characterized by steady reference levels, indicating that, at least from a biosignal processing point of view, the overall signal dynamics are recovered from propofol and that the physiological system is associated with a high degree of signal interaction.

The signal interaction pattern observed after propofol administration is influenced only by propofol dose, and thus not by PMA. This relation was observed for the pairwise interaction curves and the system interaction measure (average graph degree) derived from the graph model of the neonate.

Data Availability

The data used to support the findings of this study are restricted by the Ethische Commissie onderzoek UZ/KU Leuven in order to protect patient privacy. Data are available from Dries Hendrikx (dries.hendrikx@esat.kuleuven.be) for researchers who meet the criteria for access to this confidential data.

Disclosure

This paper reflects only the authors' views and the union is not liable for any use that may be made of the contained information.

Conflicts of Interest

The authors declare that there are no conflicts of interest regarding the publication of this paper, since the received funding, as stated in the Acknowledgments, does not lead to any conflicts of interest.

Acknowledgments

This research is supported by Bijzonder Onderzoeksfonds (BOF), KU Leuven: SPARKLE Sensor-based Platform for the accurate and remote monitoring of kinematics linked to Ehealth (no. IDO-13-0358), the effect of perinatal stress on the later outcome in preterm babies (no. C24/15/036), and TARGID—development of a novel diagnostic medical device to assess gastric motility (no. C32-16-00364); Fonds voor Wetenschappelijk Onderzoek (FWO), Vlaanderen: Hercules Foundation (AKUL 043) “Flanders BCI Lab—High-End, Modular EEG Equipment for Brain Computer Interfacing”; Agentschap Innoveren en Ondernemen (VLAIO) (150466: OSA+); Agentschap voor Innovatie door Wetenschap en Technologie (IWT) (O&O HBC 2016 0184); eWatch, imec funds 2017, imec ICON projects (ICON HBC.2016.0167) and “SeizeIT”, Belgian Foreign Affairs Development Cooperation: VLIR UOS programs (20132019); EU: European Union's Seventh Framework Programme (FP7/2007-2013), The HIP Trial: no. 260777; ERASMUS + (INGDIVS 2016-1-SE01-KA203-022114); and European Research Council. The research leading to these results has received funding from the European Research Council under the European Union's Seventh Framework Programme (FP7/20072013)/ERC advanced grant: BIOTENSORS (no. 339804) and EU H2020-FETOPEN “AMPHORA” no. 766456. Dries Hendrikx is a SB Ph.D. fellow at Fonds voor Wetenschappelijk Onderzoek (FWO), Vlaanderen, supported by the Flemish government.

References

- [1] J. A. Bondy and U. S. R. Murty, *Graph Theory with Applications*, Elsevier Science Publishing Co., Inc., 1982.
- [2] A. Caicedo, G. Naulaers, P. Lemmers, F. van Bel, M. Wolf, and S. Van Huffel, “Detection of cerebral autoregulation by near-infrared spectroscopy in neonates: performance analysis of measurement methods,” *Journal of Biomedical Optics*, vol. 17, no. 11, article 117003, 2012.

- [3] O. Semenova, J. M. O'Toole, G. Boylan, E. Dempsey, and A. Temko, "Modelling interactions between blood pressure and brain activity in preterm neonates," in *2017 39th Annual International Conference of the IEEE Engineering in Medicine and Biology Society (EMBC)*, pp. 3969–3972, Seogwipo, South Korea, July 2017.
- [4] M. L. Tataranno, T. Alderliesten, L. S. de Vries et al., "Early oxygen-utilization and brain activity in preterm infants," *PLoS One*, vol. 10, no. 5, article e0124623, 2015.
- [5] R. P. Bartsch, K. K. L. Liu, A. Bashan, and P. C. Ivanov, "Network physiology: how organ systems dynamically interact," *PLoS One*, vol. 10, no. 11, article e0142143, 2015.
- [6] A. Smits, L. Thewissen, A. Caicedo, G. Naulaers, and K. Allegaert, "Propofol dose-finding to reach optimal effect for (semi-)elective intubation in neonates," *The Journal of Pediatrics*, vol. 179, pp. 54–60.e9, 2016.
- [7] L. Welzing, A. Kribs, F. Eifinger, C. Huenseler, A. Oberthuer, and B. Roth, "Propofol as an induction agent for endotracheal intubation can cause significant arterial hypotension in preterm neonates," *Paediatric Anaesthesia*, vol. 20, no. 7, pp. 605–611, 2010.
- [8] J. Vanderhaegen, G. Naulaers, S. Van Huffel, C. Vanhole, and K. Allegaert, "Cerebral and systemic hemodynamic effects of intravenous bolus administration of propofol in neonates," *Neonatology*, vol. 98, no. 1, pp. 57–63, 2010.
- [9] P. Papoff, M. Mancuso, E. Caresta, and C. Moretti, "Effectiveness and safety of propofol in newborn infants," *Pediatrics*, vol. 121, no. 2, pp. 448–449, 2008.
- [10] S. H. P. Simons, R. van der Lee, I. K. M. Reiss, and M. M. van Weissenbruch, "Clinical evaluation of propofol as sedative for endotracheal intubation in neonates," *Acta Paediatrica*, vol. 102, no. 11, pp. e487–e492, 2013.
- [11] M. G. Penido, D. F. de Oliveira Silva, E. C. Tavares, and Y. P. e Silva, "Propofol versus midazolam for intubating preterm neonates: a randomized controlled trial," *Journal of Perinatology*, vol. 31, no. 5, pp. 356–360, 2011.
- [12] A. Vardi, Y. Salem, S. Padeh, G. Paret, and Z. Barzilay, "Is propofol safe for procedural sedation in children? A prospective evaluation of propofol versus ketamine in pediatric critical care," *Critical Care Medicine*, vol. 30, no. 6, pp. 1231–1236, 2002.
- [13] M. A. Claeys, E. Gepts, and F. Camu, "Haemodynamic changes during anaesthesia induced and maintained with propofol," *British Journal of Anaesthesia*, vol. 60, no. 1, pp. 3–9, 1988.
- [14] M. Muzi, R. A. Berens, J. P. Kampine, and T. J. Ebert, "Veno-dilation contributes to propofol-mediated hypotension in humans," *Anesthesia and Analgesia*, vol. 74, no. 6, pp. 877–883, 1992.
- [15] C. C. Hug Jr, C. H. McLeskey, M. L. Nahrwold et al., "Hemodynamic effects of propofol: data from over 25,000 patients," *Anesthesia and Analgesia*, vol. 77, 4 Supplement, pp. S21–S29, 1993.
- [16] S. Ghanta, M. E. Abdel-Latif, K. Lui, H. Ravindranathan, J. Awad, and J. Oei, "Propofol compared with the morphine, atropine and suxamethonium regimen as induction agents for neonatal endotracheal intubation: a randomized, controlled trial," *Pediatrics*, vol. 119, no. 6, pp. e1248–e1255, 2007.
- [17] Y.-C. Hung, C.-J. Huang, C. H. Kuok, C.-C. Chen, and Y.-W. Hsu, "The effect of hemodynamic changes induced by propofol induction on cerebral oxygenation in young and elderly patients," *Journal of Clinical Anesthesia*, vol. 17, no. 5, pp. 353–357, 2005.
- [18] A. Shafer, "Metaphor and anesthesia," *Anesthesiology*, vol. 83, no. 6, pp. 1331–1342, 1995.
- [19] E. N. Brown, R. Lydic, and N. D. Schiff, "General anesthesia, sleep, and coma," *The New England Journal of Medicine*, vol. 363, no. 27, pp. 2638–2650, 2010.
- [20] N. Roche-Labarbe, F. Wallois, E. Ponchel, G. Kongolo, and R. Grebe, "Coupled oxygenation oscillation measured by NIRS and intermittent cerebral activation on EEG in premature infants," *NeuroImage*, vol. 36, no. 3, pp. 718–727, 2007.
- [21] W. P. Akrawi, J. C. Drummond, C. J. Kalkman, and P. M. Patel, "A comparison of the electrophysiologic characteristics of EEG burst-suppression as produced by isoflurane, thiopental, etomidate, and propofol," *Journal of Neurosurgical Anesthesiology*, vol. 8, no. 1, pp. 40–46, 1996.
- [22] S. Ching, P. L. Purdon, S. Vijayan, N. J. Kopell, and E. N. Brown, "A neurophysiological-metabolic model for burst suppression," *Proceedings of the National Academy of Sciences of the United States of America*, vol. 109, no. 8, pp. 3095–3100, 2012.
- [23] A. Caicedo, L. Thewissen, A. Smits, G. Naulaers, K. Allegaert, and S. Van Huffel, "Relation between EEG activity and brain oxygenation in preterm neonates," in *Oxygen Transport to Tissue XXXIX*, H. Halpern, J. LaManna, D. Harrison, and B. Epel, Eds., vol. 977 of *Advances in Experimental Medicine and Biology*, pp. 133–139, Springer, Cham, 2017.
- [24] K. Allegaert, M. Y. Peeters, R. Verbesselt et al., "Inter-individual variability in propofol pharmacokinetics in preterm and term neonates," *British Journal of Anaesthesia*, vol. 99, no. 6, pp. 864–870, 2007.
- [25] March of Dimes, PMNCH, Save the Children, and WHO, *Born Too Soon: the Global Action Report on Preterm Birth*, C. P. Howson, M. V. Kinney, and J. E. Lawn, Eds., World Health Organization, Geneva, 2012.
- [26] K. Allegaert, J. D. Hoon, R. Verbesselt, G. Naulaers, and I. Murat, "Maturation pharmacokinetics of single intravenous bolus of propofol," *Pediatric Anesthesia*, vol. 17, no. 11, pp. 1028–1034, 2007.
- [27] D. J. Eleveld, P. Colin, A. R. Absalom, and M. M. R. F. Struys, "Pharmacokinetic-pharmacodynamic model for propofol for broad application in anaesthesia and sedation," *British Journal of Anaesthesia*, vol. 120, no. 5, pp. 942–959, 2018.
- [28] E. K. S. Louis and L. C. Frey, *Electroencephalography (EEG): An Introductory Text and Atlas of Normal and Abnormal Findings in Adults, Children, and Infants*, American Epilepsy Society, Illinois, 2016.
- [29] A. M. Husain, "Review of neonatal EEG," *American Journal of Electroneurodiagnostic Technology*, vol. 45, no. 1, pp. 12–35, 2005.
- [30] A. Dereymaeker, N. Koolen, K. Jansen et al., "The suppression curve as a quantitative approach for measuring brain maturation in preterm infants," *Clinical Neurophysiology*, vol. 127, no. 8, pp. 2760–2765, 2016.
- [31] N. Koolen, K. Jansen, J. Vervisch et al., "Line length as a robust method to detect high-activity events: automated burst detection in premature EEG recordings," *Clinical Neurophysiology*, vol. 125, no. 10, pp. 1985–1994, 2014.
- [32] J. A. K. Suykens, T. Van Gestel, J. De Brabanter, B. De Moor, and J. Vandewalle, *Least Squares Support Vector Machines*, World Scientific, 2002.

- [33] R. J. Wilson, *Introduction to Graph Theory*, Prentice Hall, 4th edition, 1996.
- [34] O. L. de Weck, "MIT strategic engineering: Matlab tools for network analysis," 2011, February 2017 <http://strategic.mit.edu/downloads.php?%20page=matlab%20networks>.
- [35] J. O. Rawlings, S. G. Pantula, and D. A. Dickey, *Applied Regression Analysis: A Research Tool*, Springer-Verlag New York, Inc., Second Edition edition, 1998.
- [36] E. van den Berg, P. M. A. Lemmers, M. C. Toet, J. H. G. Klaessens, and F. van Bel, "Effect of the "InSurE" procedure on cerebral oxygenation and electrical brain activity of the preterm infant," *Archives of Disease in Childhood - Fetal and Neonatal Edition*, vol. 95, no. 1, pp. F53–F58, 2010.

Research Article

Effect of EOG Signal Filtering on the Removal of Ocular Artifacts and EEG-Based Brain-Computer Interface: A Comprehensive Study

Malik M. Naeem Mannan ¹, M. Ahmad Kamran,¹ Shinil Kang,^{2,3} and Myung Yung Jeong ¹

¹Department of Cogno-Mechatronics Engineering, Pusan National University, 2 Busandaehak-ro 63beon-gil Geumjeong-gu, Busan 609-735, Republic of Korea

²National Center for Optically-Assisted Ultrahigh-precision Mechanical Systems, Yonsei University, Seoul 03722, Republic of Korea

³School of Mechanical Engineering, Yonsei University, Seoul 03722, Republic of Korea

Correspondence should be addressed to Myung Yung Jeong; myjeong@pusan.ac.kr

Received 14 February 2018; Revised 22 April 2018; Accepted 12 May 2018; Published 4 July 2018

Academic Editor: Gaoxiang Ouyang

Copyright © 2018 Malik M. Naeem Mannan et al. This is an open access article distributed under the Creative Commons Attribution License, which permits unrestricted use, distribution, and reproduction in any medium, provided the original work is properly cited.

It is a fact that contamination of EEG by ocular artifacts reduces the classification accuracy of a brain-computer interface (BCI) and diagnosis of brain diseases in clinical research. Therefore, for BCI and clinical applications, it is very important to remove/reduce these artifacts before EEG signal analysis. Although, EOG-based methods are simple and fast for removing artifacts but their performance, meanwhile, is highly affected by the bidirectional contamination process. Some studies emphasized that the solution to this problem is low-pass filtering EOG signals before using them in artifact removal algorithm but there is still no evidence on the optimal low-pass frequency limits of EOG signals. In this study, we investigated the optimal EOG signal filtering limits using state-of-the-art artifact removal techniques with fifteen artificially contaminated EEG and EOG datasets. In this comprehensive analysis, unfiltered and twelve different low-pass filtering of EOG signals were used with five different algorithms, namely, simple regression, least mean squares, recursive least squares, REGICA, and AIR. Results from statistical testing of time and frequency domain metrics suggested that a low-pass frequency between 6 and 8 Hz could be used as the most optimal filtering frequency of EOG signals, both to maximally overcome/minimize the effect of bidirectional contamination and to achieve good results from artifact removal algorithms. Furthermore, we also used BCI competition IV datasets to show the efficacy of the proposed framework on real EEG signals. The motor-imagery-based BCI achieved statistically significant high-classification accuracies when artifacts from EEG were removed by using 7 Hz low-pass filtering as compared to all other filterings of EOG signals. These results also validated our hypothesis that low-pass filtering should be applied to EOG signals for enhancing the performance of each algorithm before using them for artifact removal process. Moreover, the comparison results indicated that the hybrid algorithms outperformed the performance of single algorithms for both simulated and experimental EEG datasets.

1. Introduction

The functional dynamics of the brain have been thoroughly investigated over the course of many years using noninvasive brain imaging techniques [1–5]. Electroencephalography (EEG), for example, is a portable neuroimaging system that can be used to assess different functional brain states [6–9]. However, a recorded EEG signal is highly contaminated with nonneuronal activities from different sources including eye

blinking, eye movements, muscle movements, and electrocardiography (ECG) [10–15]. Eye movements and blinking generate high-magnitude artifacts as compared with the pure neuronal activity present in EEG data [16–18]. Such interferences are commonly known as ocular artifacts [19, 20].

It is widely accepted within the BCI research community that in any BCI system, neurological phenomena are the only source of control [21, 22]. Artifacts, unwanted electrical signals that arise from sources other than the brain, can

interfere with neurological phenomena. Such artifacts might alter the characteristics of neurological phenomena or even be mistakenly used as the source(s) of control in BCI systems [23]. Among the different artifacts, eye movement and blinks are the most important and major sources of physiological artifacts in BCI systems [24–26]. If not removed, these artifacts could, as indicated above, be mistakenly used to control the BCI system, which is the most significant artifact-related problem [27]. As failing to deal with artifacts can result in deterioration of BCI system performance during practical applications, it is necessary to develop automatic methods to handle artifacts or to design BCI systems robust to them. Bashashati et al. showed that dealing with eye artifacts in EEG data can enhance the performance of a self-paced BCI system [24]. Erfanian and Mahmoudi used recurrent neural networks to automatically suppress ocular artifacts for improved EEG-based BCI performance [25]. Recently, Yong et al. combined stationary wavelet analysis with adaptive thresholding to automatically remove ocular artifacts from EEG data in an EEG- and eye tracker-based self-paced BCI system [26]. They showed that their system can achieve higher BCI performance than can BCIs in which artifacts are not removed. Furthermore, artifacts can also affect diagnosis and analysis in clinical research such as on sleep disorders, Alzheimer disease, and schizophrenia [28–32]. It is therefore mandatory, in either clinical or practical research, to deal with these artifacts prior to the analysis of EEG signals.

Several manual and automated methods have been developed to deal with this challenging task. One straightforward approach to the reduction of ocular artifacts is to prevent eye movements as much as possible, though requiring this and achieving it are two very different things. Also, the specific request of avoiding blinks could affect the investigated states and cognitive process of the subject [33]. Another commonly employed solution is to discard those epochs of EEG data that contain ocular artifacts, though this can incur the loss of neuronal activity-related EEG data. Alternatively, several automated methods for detection and removal/reduction of ocular artifacts have been proposed such as blind source separation-based methods, wavelet transforms, regression-based analysis, and empirical mode decomposition. Among these, the most commonly employed, which are known as regression-based algorithms, are based on the removal of electrooculography (EOG) contamination from EEG data. The simplest and most common procedure for removal of ocular artifacts from EEG data entails the subtraction, from each EEG channel, of reference channel signals containing proper artifactual interference. Techniques of this kind were widely applied until the mid-1990s, due to their low computational costs and simplicity [20, 33]. Subsequently, researchers used EOG channels to record eye movement and blinking to efficiently remove ocular artifacts from EEG data. EOG-based methodologies assume that the true neuronal activity and ocular artifacts are present in a linear combination in acquired EEG signals. These methods employ regression-based analysis [10, 18, 34–46], by which, in the time domain, the contamination coefficients of EOG signals are estimated and subtracted from each EEG channel to

obtain clean EEG signals. Since being very low computation demanding, they are a great tool for real-time/online BCI applications. Although these methods have been proved to be more efficient than simple reference channel regression, their performance is highly affected by many factors. For example, neuronal activity from the frontal brain area, which EOG additionally measures, might be eliminated during the subtraction process, resulting in loss of true EEG signals [47]. Furthermore, these techniques are based on the assumption that EOG signals and neuronal activity recorded in EEG signals have no correlation, which has been found to be totally invalid [48, 49]. In order to overcome these issues, recently, regression-based algorithms have been combined with blind source separation techniques in the development of automated methodologies for removal of ocular artifacts [47, 50]. These methodologies have been shown to be more effective than either only regression- or blind source separation-based techniques, but they still lack the best results. The reason might be due to the fact that the outcomes are still affected by bidirectional contamination.

The main problem with regression-based techniques is that they are always affected by bidirectional contamination; for example, EEG recordings are contaminated as the results of eye movement and blinking, while EOG recordings are contaminated by neuronal activities (originating mostly from the frontal and lateral frontal areas) [18, 47, 50, 51]. Therefore, removal of ocular artifacts using EOG signals would also remove common neuronal activity present in both EEG and EOG data. In a modified version of the regression method, called filtered regression, the effects of bidirectional contamination are reduced by low-pass filtering of EOG signals prior to regression analysis [39, 43, 44, 52]. This idea is based on studies that have shown that high-frequency components in EOG channels are generated from brain activity [43, 52]. In Table 1 list of the different low-pass frequencies used by researchers, it can be seen that there is no consensus on any particular frequency of EOG signal, though there is agreement on the fact that the most of the low-frequency components in EOG signals belongs to the ocular artifacts [43, 44, 47, 51, 52]. Determining the optimal low-pass frequency for EOG signals is very important, as the outcomes for regression-based correction methods can be affected by the selected filtering frequency. To the best of our knowledge, no study has investigated the optimal low-pass EOG signal filtering limits for use with regression-based algorithms. Our hypothesis is that EOG signal filtering will enhance the process of artifact removal to reduce bidirectional contamination and if so, then what are the optimal low-pass frequency limits which will give better results from all other low-pass filtering.

In this study, we used simulated contaminated EEG and EOG datasets and motor-imagery-based experimental BCI datasets to investigate the effect of different EOG filtering on the removal of ocular artifacts from EEG data. We used 12 different low-pass EOG signal filtering and unfiltered EOG data along with five different methods from the literature, namely, simple regression [44], least mean square-based regression [53], recursive least squares based regression [45], REGICA [47], and the method developed in [51] (we reference it hereafter as automatic independent

TABLE 1: Different low-pass EOG signal filtering frequencies used in literature.

Study	Low-pass filtering (Hz)	Journal
Maddirala and Shaik [67]	~5	IEEE Sensors Journal
Yang et al. [68]	~100	Neurocomputing
Kanoga et al. [69]	~60	Neurocomputing
Mannan et al. [51]	~5	Front. Hum. Neuro.
Wang et al. [70]	~8	Biomed. Signal Process. Control
Zeng et al. [71]	~15	The Sci. World J.
Sameni and Gouy-Pailler [72]	~100	J. Neurosci. Methods
Murthy and Khan [73]	~30	Research J. Biotech.
Klados et al. [47]	~5	Biomed. Signal Process. Control
Pham et al. [42]	~200	Int. J. Psychophysiology
Ghandeharion and Erfanian [61]	~45	Medical Eng. Phy.
Chan et al. [74]	~30	Annals of Biomed. Eng.
Romero et al. [43]	~7.5	Annals of Biomed. Eng.
Romero et al. [44]	~7.5	Computer in Bio. Med.
Schlogl et al. [55]	~100	Clin. Neurophy.
Puthusserypady and Ratnarajah [75]	~11.5	Signal Process.
Erfanian and Mahmoudi [25]	~40	Med. Biol. Eng. Comput.
Croft et al. [38]	~100	Phychophy.
He et al. [45]	~30	Med. Bio. Eng. Comput.
Wallstrom et al. [18]	~100	Int. J. Psych.
Moretti et al. [76]	~100	Int. J. Psych.
Croft and Barry [66]	~100	Int. J. Psych.
Croft and Barry [35]	~35	Electroen. Clin. Neuro.
Sadasivan and Dutt [65]	~10	Signal Process.

component analysis and regression (AIR)) to determine the effect of different EOG signal filtering on artifact removal from EEG data. Since the underlying artifact-free EEG (true EEG) in artificially contaminated EEG data is known; therefore, it is possible to evaluate the effect of each EOG filtering using different performance metrics. The performance evaluation indexes employed were the mean square error and the mean absolute error in the time and frequency domains, respectively. Additionally, mutual information was utilized to estimate the common information between the reconstructed EEG signal and the artifact-free EEG signal. The improvements in reconstructed EEG is also evaluated using signal-to-artifact ratio before and after the artifact removal process for all algorithms. For real EEG datasets, we evaluated the classification accuracies of each subject and each method after the artifact removal using different low-pass EOG filtering. Finally, paired *t*-test was employed to the results of simulated and experimental datasets to find out the optimal EOG filtering with highest

statistical significance. The results of this statistical testing revealed that best results from EOG-based algorithms could be achieved if low-pass frequency is used from 6–8 Hz. Furthermore, the results of both simulated and real EEG signals indicate that hybrid algorithms performed better than simple regression and adaptive filtering. A schematic diagram of the study is shown in Figure 1.

2. Materials and Methods

2.1. Materials. This section describes the detailed procedure used to simulate contaminated EEG and EOG datasets and real EEG datasets used from BCI competition IV.

2.1.1. Simulated Datasets

(1) *Participants.* Fifteen (15) healthy subjects (all male) participated in this study. All had normal or corrected-to-normal vision. The experimental protocol was approved by the Institutional Review Board of Pusan National University. Experiment was conducted in accordance with the ethical guidelines established by the Institutional Review Board of Pusan National University and the Declaration of Helsinki. Each participant was asked to sign an informed consent form after being thoroughly informed about the nature and purpose of the study. The experiments were performed in a quiet room with dim lighting to prevent environmental disturbances. Each participant was seated in an armchair at a distance of about 1 m from a 24" LCD monitor (ASUS; resolution: 1366 × 768).

(2) *Experiment 1.* In this experiment, the participants were asked to sit relaxed and calm while keeping their eyes closed for 30 s. Each also was instructed to avoid moving their eyes during the experiment so as to avoid or at least minimize artifacts. After the experiment, the subjects' data were carefully inspected for any presence of major artifacts; none was found. These datasets were then used as "clean EEG" signals for the purposes of further analysis. The data from this experiment will be referred as the "neuronal group" throughout in this paper.

(3) *Experiment 2.* The experimental protocol was as follows. At the start of the experiment, the subject was instructed to sit relaxed and calm for 3 s. Three different word cues (blink, move horizontally, and move vertically) were used. The subjects were asked to blink their eyes or move them vertically or horizontally according to any of six visual cues (2 cues for each word) that appeared for 2 s each at the center of the screen. The interval between the cues was 2 s. At the end of the experiment, each subject was again asked to relax for 3 s. The total duration of the experiment was 30 s. The data from this experiment will be referred as "artificial group" throughout in this paper.

(4) *EEG Recordings.* The EEG data were acquired using an ActiCap 32-channel active electrode system with a BrainAmp DC amplifier (Brain Products GmbH, Gilching, Germany). The data sampling rate was 250 Hz. Nineteen

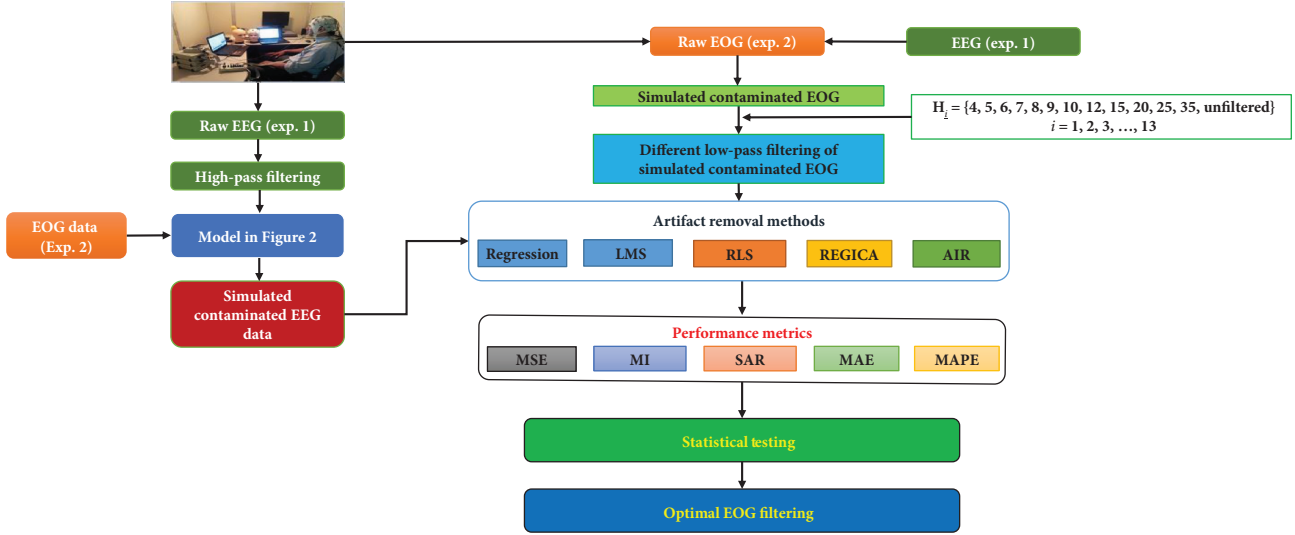


FIGURE 1: Schematic plan of the study.

TABLE 2: Class-wise list of frequencies for low-pass EOG signal filtering used in this study.

Class	Low-pass frequency (Hz)			
I	4			
II	5	6	7	8
III	9	10	12	15
IV	20	25	35	Unfiltered

(19) electrodes positioned according to the international 10–20 system (Fp1, Fp2, F3, F4, F7, F8, Fz, C3, C4, Cz, T7, T8, P7, P8, Pz, P3, P4, O1, and O2) were used for acquisition of EEG signals. AFz and FCz were used as the ground and reference electrodes, respectively. The impedance of all of the electrodes was reduced to below 5 k Ω . The data were high-pass filtered at 0.5 Hz.

(5) *EOG Recordings*. The EOG data were acquired using the BrainAmp ExG system (Brain Products GmbH, Gilching, Germany). Four electrodes were placed around the left and right eye to record ocular activities. All of the data were sampled at a rate of 250 Hz. Table 2 lists the class-wise low-pass frequencies used in this study.

(6) *Simulated Datasets*. In the present study, in order to investigate the optimal frequency limits, we simulated 15 artificially contaminated EEG and EOG datasets. As the underlying true EEG signal in artificially contaminated EEG data is known, such data can be used as a primary tool to determine the optimal filtering for EOG signals. We utilized EEG data recorded in an eyes-closed session to simulate contaminated EEG. Whereas such data might contain low-frequency eye movement contamination, they are notwithstanding preferred, as they tend to contain minimal overall artifacts. The alternative to this is eyes-open data acquisition. Note though that human eyes produce much-higher-

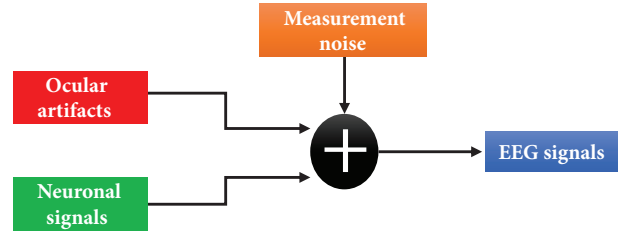


FIGURE 2: General approach for generation of EEG data.

amplitude signals in light than in darkness [54]. In this sense, recording of EEG signals in an eyes-closed session is preferred. However, EOG signals were acquired in an eyes-open session with different eye movements. Simple linear models were estimated to calculate the parameters of contamination for both EEG and EOG. By doing so, we can simulate signals which are bidirectionally contaminated, that is, EEG data is contaminated with EOG signals and EOG data is contaminated with EEG signals. In this sense, we can obtain simulated signals as close as possible to real signals [43].

(6.1) *Simulated EEG Signals*. It is known that the recorded EEG signal contains pure activity from neurons, ocular artifacts, and measurement noise (artifacts from all other sources), as shown in Figure 2. In this paper, neuronal sources (EEG signals from the neuronal group) were artificially contaminated with ocular sources (EOG signals from the artifactual group) to simulate contaminated EEG signals [43]. These interferences were calculated by estimation of simple linear models between EEG and EOG recordings [44]. The detailed procedure is explained below.

Four 2 s epochs with high EOG actives were selected from each one of the fifteen subjects from the artifactual group. A simple linear model was estimated for each 2 s epoch and for each channel. These models have two inputs corresponding to $VEOG_A$ and $HEOG_A$ signals (where X_A refers to signals

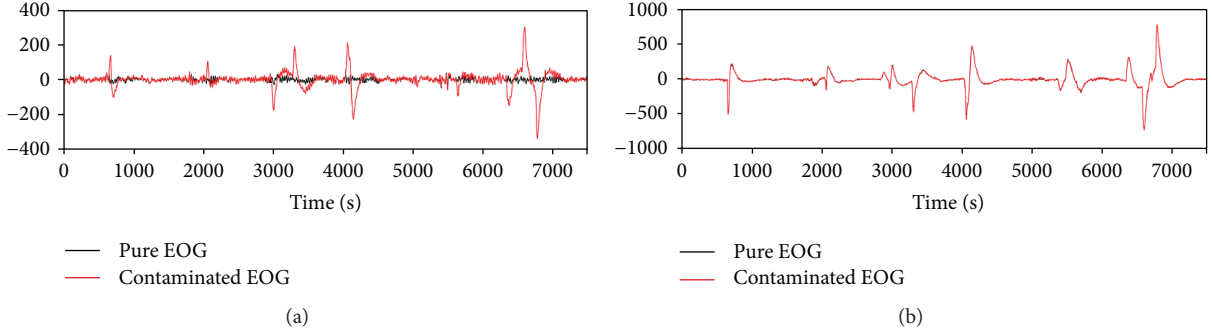


FIGURE 3: Example of simulated signals. (a) Simulated contaminated EEG signal. (b) Simulated contaminated EOG signal.

from the artifactual group) and one output that was each one of the 19 EEG_A channels. For a better estimation of models, neuronal activity in EOG due to bidirectional contamination is reduced in order to calculate accurate parameters of contamination. For this purpose, in each model, EEG_A and EOG_A channels, corresponding to outputs and inputs, respectively, were low-pass filtered with the cutoff frequency corresponding to the highest value of the 99% (f_{99}) of the total energy of these $VEOG_A$ and $HEOG_A$ signals [43]. Thus, the remainder 1% of signal energy was not considered as ocular activity (neural activity, power line interference, electrode noise, etc.) in the EOG_A recordings [43]. The 99% cutoff frequencies obtained were 6.44 ± 2.43 and 7.61 ± 3.82 Hz for $VEOG_A$ and $HEOG_A$, respectively, as mean and standard deviation for all epochs and subjects. This idea was based on and supported by the consideration that most components in the EOG signals related to the high frequencies are of neuronal source [52].

A linear model used to estimate parameters of EOG interferences for each EEG channel i ($i = 1, 2, 3, \dots, 19$) and each epoch p ($p = 1, 2, 3, 4$) is evaluated as follows.

$$EEG_{Aip} = \alpha_{ip} VEOG_{Ap} + \beta_{ip} HEOG_{Ap} + e, \quad (1)$$

where α and β are the unknown model parameters, and e is unknown error mapping. By this procedure, we got four α and four β parameters corresponding to all four epochs for each channel. These parameters were averaged ($\sum_{p=1}^4 \alpha_{ip}/4$ and $\sum_{p=1}^4 \beta_{ip}/4$) to obtain ocular contamination coefficients α_i and β_i for each channel. Finally, simulated EEG signals were generated according to Elbert's contamination model [54] as

$$cEEG_{Ni} = pEEG_{Ni} + \alpha_i VEOG_A + \beta_i HEOG_A + v, \quad (2)$$

where $cEEG$ and $pEEG$ are the artificially contaminated and pure EEG signals, subindex N refers to the neuronal group, and v is modeled as white Gaussian noise compensating for other noise sources. An example of simulated contaminated EEG data for electrode Fp1 is shown in Figure 3(a).

(6.2) *Simulated EOG Signals.* Ocular sources (EOG signals from the artifactual group) were artificially contaminated with neuronal sources (EEG signals from the neuronal group) to simulate contaminated EEG signals. Similar to *simulated EEG signals*, these interferences were calculated by

approximation of simple linear models between EOG and EEG recordings. The detailed procedure is described below.

Four 2 s epochs with no apparent EOG actives were selected from all of the fifteen subjects from the neuronal group. Neuronal contamination of EOG channels was obtained from the frontal electrodes (Fp1, Fp2, F7, and F8), which are the nearest ones to the eyes [44]. A linear model for both $VHOG_N$ and $HEOG_N$ was estimated for each 2 s epoch. These models have four inputs corresponding to EEG_N signals from Fp1, Fp2, F7, and F8 and one output that was each one of the $VHOG_N$ and $HEOG_N$.

Two linear models used to estimate parameters of EEG interferences for $VEOG$ and $HEOG$, and each epoch p ($p = 1, 2, 3, 4$) is evaluated as follows:

$$VEOG_{Nip} = a_{1p} EEG_{Np Fp1} + a_{2p} EEG_{Np Fp2} + a_{3p} EEG_{Np F7} + a_{4p} EEG_{Np F8} + e, \quad (3)$$

$$HEOG_{Nip} = b_{1p} EEG_{Np Fp1} + b_{2p} EEG_{Np Fp2} + b_{3p} EEG_{Np F7} + b_{4p} EEG_{Np F8} + e, \quad (4)$$

where a_j and b_j ($j = 1, 2, 3, 4$) are the unknown model parameters.

By this procedure, we got four a_j and four b_j parameters corresponding to all four epochs for $VEOG_N$ and $HEOG_N$, respectively. These parameters were averaged ($\sum_{p=1}^4 a_{jp}/4$ and $\sum_{p=1}^4 b_{jp}/4$) to obtain neuronal contamination coefficients a_j and b_j for each $VEOG_N$ and $HEOG_N$, respectively. Finally, simulated EOG signals were generated as follows:

$$cVEOG_A = VEOG_A + a_1 EEG_{N Fp1} + a_2 EEG_{N Fp2} + a_3 EEG_{N F7} + a_4 EEG_{N F8}, \quad (5)$$

$$cHEOG_A = HEOG_A + b_1 EEG_{N Fp1} + b_2 EEG_{N Fp2} + b_3 EEG_{N F7} + b_4 EEG_{N F8},$$

where $cVEOG$ and $cHEOG$ are the artificially contaminated $VEOG$ and $HEOG$, respectively. An example of simulated contaminated EOG data can be visualized in Figure 3(b).

2.1.2. *Experimental Datasets.* In this study, the datasets from nine healthy subjects were sampled from publically available MI-based BCI signals of BCI competition IV (datasets 2a).

Four different MI classes including left hand, right hand, both feet, and tongue were performed by all subjects. The experiment consisted of training sessions and evaluation sessions. For all subjects, each session consisted of six runs with short breaks. For each subject, two classes from evaluation sessions corresponding to left- and right-hand MI were selected. One run consisted of twelve trials of each class, resulting in 144 trials for each subject. Twenty-two EEG and three EOG channels [55] were used to record the data with a sampling frequency of 250 Hz and 50 Hz notch filter. All EEG channels were recorded monopolarly with the left mastoid serving as reference and the right mastoid as ground. The signals were band-pass filtered between 0.5 and 100 Hz. More details can be found in [56]. The datasets were highly contaminated with ocular artifacts which is a challenging problem in practical BCI systems [57].

2.2. Methods. In literature, different artifact removal algorithms have been developed to deal with the ocular contamination present in EEG signals. Broadly speaking, these algorithms can be divided into three main categories, namely, EOG-based, non-EOG-based, and hybrid algorithms. The most commonly employed among those are EOG-based regression algorithms [18, 33]. Although these algorithms are simple and perform well as compared with manual rejection, they nonetheless cause EEG data distortion due to bidirectional contamination [47]. To improve the performance of simple regression-based algorithms, researchers developed adaptive filter-based regression algorithms. Most commonly used adaptive filters are least mean squares and recursive least square-based filters, and these methods proved to be more effective as compared to simple regression. On the other hand, non-EOG-based algorithms, for example, the ICA-based algorithms, do not require any EOG signals, though their removal of artifactual ICs might cause the loss of substantial neuronal data, which is their major drawback [58, 59]. Urigüen and Garcia-Zapirain [10] suggested that multiple-combination artifact removal methods can be developed to efficiently remove artifacts from recorded EEG signals. Recently, EOG-based algorithms have been combined with non-EOG-based algorithms (ICA) to more effectively deal with ocular artifacts present in EEG data [47, 50, 51]. These algorithms were shown to outperform all of the algorithms with which they were compared in terms of artifact removal and maintenance of neuronal activity present in EEG data; however, their performance can be further improved if optimal low-pass EOG filtering is used. In this study, we used all three kinds of EOG-based algorithms (simple regression, adaptive regression, and hybrid methods) to investigate the effect of different low-pass filtering on the removal of ocular artifacts from EEG data. One may argue that there are other methods like ICA that can be used to remove ocular artifacts from EEG data without the need of EOG signals, but irrespective of their other disadvantages these methods cannot be used for real-time/online BCI applications whereas regression-based methods (simple and adaptive) are simple and fast; therefore, it can be used as an optimal option for BCI applications if their performance is enhanced [60].

Next, we will briefly describe the implementation steps of the methods used in this study.

2.2.1. Simple Regression Method. The simple regression method is implemented as follows [44]:

- (1) Equation (3) in [44] was used to estimate the parameters of EOG signals.
- (2) Artifact-free EEG was reconstructed by subtracting estimated VEOG and HEOG from contaminated EEG.

2.2.2. LMS Regression Method. The LMS regression method is implemented as follows [53]:

- (1) Least mean square estimation was used to estimate the parameters of EOG signals.
- (2) Artifact-free EEG was reconstructed by subtracting estimated VEOG and HEOG from contaminated EEG.

2.2.3. RLS Regression Method. RLS regression method is applied as follows [45]:

- (1) Recursive least square estimation was used to estimate the parameters of EOG signals.
- (2) Artifact-free EEG was reconstructed by subtracting estimated VEOG and HEOG from contaminated EEG.

2.2.4. REGICA. REGICA is implemented as follows [47]:

- (1) EEG signals are independent component analysis (ICA) decomposed.
- (2) Independent components (ICs) are filtered using recursive least square estimation with reference EOG signal.
- (3) ICs are backprojected to reconstruct EEG signal.

2.2.5. AIR. AIR is implemented as follows [51]:

- (1) Contaminated EEG data are decomposed using ICA to obtain ICs.
- (2) Composite multiscale entropy and kurtosis are calculated to identify ocular-artifact-related ICs.
- (3) ICs are filtered using the linear regression model and extended recursive least mean squares.
- (4) Median absolute deviation is applied to remove any high-magnitude ocular artifacts left.
- (5) Artifact-free EEG data are obtained by backprojecting all ICs using inverse ICA.

2.3. Evaluation Indexes

2.3.1. Mean Square Error. In this study, the performance of each algorithm for each of the EOG signal filtering ranges

was evaluated using the mean square error. It was defined as [41].

$$\text{MSE} = \sum_{n=1}^N \frac{[\text{EEG}_{\text{out}} - \text{EEG}_{\text{in}}]^2}{N}, \quad (6)$$

where EEG_{out} is the reconstructed EEG and EEG_{in} is the artifact-free EEG (EEG from the neuronal group).

2.3.2. Mutual Information. The amount of mutual information between the reconstructed EEG signal and the artifact-free EEG was calculated in order to analyze the utility of each method for recovery of neuronal activity-related EEG signals. Mathematically, the calculation proceeds as follows [61]:

$$\text{MI} = \int_{-\infty}^{\infty} \int_{-\infty}^{\infty} f(a, b) \log \frac{f(a, b)}{f(a)f(b)} da db, \quad (7)$$

where $f(a, b)$ represents the joint pdf and $f(a)$ and $f(b)$ represent the marginal pdfs. The artifact-free EEG and reconstructed EEG were deemed to be closely related if and only if the mutual information values between them were large.

2.3.3. Signal-to-Artifact Ratio. Signal-to-artifact ratio is the metric commonly used to evaluate the improvements in the corrected EEG signal as compared to the contaminated EEG signal. We calculated signal-to-artifact ratio for contaminated EEG signals as follows [62].

$$\text{SAR}_B = \frac{1/N \sum_{n=1}^N |\text{EEG}_{\text{in}}|^2}{1/N \sum_{n=1}^N |\text{EEG}_{\text{cn}} - \text{EEG}_{\text{in}}|^2}, \quad (8)$$

where SAR_B is signal-to-artifact ratio before artifact removal, and EEG_{cn} is the contaminated EEG signal. We also calculated signal-to-artifact ratio for corrected EEG as follows.

$$\text{SAR}_A = \frac{1/N \sum_{n=1}^N |\text{EEG}_{\text{in}}|^2}{1/N \sum_{n=1}^N |\text{EEG}_{\text{cr}} - \text{EEG}_{\text{in}}|^2}, \quad (9)$$

where SAR_A is signal-to-artifact ratio after artifact removal and EEG_{cr} is the corrected EEG signal. An effective artifact removal algorithm will remove all the artifacts and will have higher SAR_A values and consequently $\text{SAR}_A > \text{SAR}_B$. The gain in signal-to-artifact ratio γ can be calculated as follows.

$$\gamma = 10 \log \left(\frac{\text{SAR}_A}{\text{SAR}_B} \right). \quad (10)$$

The γ value is positive if signal-to-artifact ratio is improved, negative if signal-to-artifact ratio is decreased and zero if there is no improvement.

2.3.4. Mean Absolute Error. In order to measure the percentage distortion across the different frequency bands delta (0.5–4 Hz), theta (4–8 Hz), alpha (8–12 Hz), beta (12–30 Hz), and gamma (30–100 Hz), mean absolute error was defined as [51]

$$\text{MAE} = |P_{\text{inEEG}} - P_{\text{outEEG}}|, \quad (11)$$

where P denotes the power spectrum density (PSD). PSD was estimated using the Welch method according to the following parameters: 200 sample points as the window length and 5 sample points as the overlap. The average PSD for each frequency band was calculated for all subjects.

Also, mean absolute percentage error to estimate the percentage distortion in each frequency band was defined as [43].

$$\text{MAPE} = 100 \times \left| \frac{P_{\text{inEEG}} - P_{\text{outEEG}}}{P_{\text{inEEG}}} \right|. \quad (12)$$

3. Results

This study investigated the effect of low-pass filtering on the removal of ocular artifacts from EEG data. According to the literature, different studies used different low-pass filtering for EOG signals ranging from 4 to 100 Hz. In this study, we used unfiltered and twelve different low-pass EOG filtering with simulated EEG datasets in an effort to find the optimal one from which best results could be achieved. For this purpose, we used five different methods from the literature with five performance evaluation metrics. Table 3 lists the average mean square errors of all of the simulated datasets and for all of the electrodes with each method. It can be seen that the mean square error was lowest when the low-pass filter from 6 to 8 Hz was used. Furthermore, the mutual information scores also were calculated in a time domain analysis; the results of which are shown in Table 4. Similar to the mean square error results, the average mutual information for all of the datasets and all of the electrodes was the maximum when one of the 6 to 8 Hz low-pass filter was used with a different method. Table 5 shows the average improvement gained in reconstructing artifact-free EEG by calculating signal-to-artifact ratio before and after the artifact removal. It can be seen that corrected EEG with every EOG filtering showed improved signal-to-artifact ratio but results of this analysis also indicate similar outcomes as in the case of mean square error and mutual information. Moreover, the investigation of the optimal filtering range was carried out also in the frequency domain, by calculating the mean absolute error and mean absolute percentage values for the different frequency bands. The effect of bidirectional contamination can be best observed and analyzed in frequency domain by evaluating the distortion produce in different frequency bands using different filtering. Results of frequency domain analysis are shown in Tables 6–10. Except delta band, mean absolute error for all bands was lowest when 6 or 7 Hz low-pass EOG filtering was used. In case of delta band, least mean squares and recursive least squares showed lowest errors with 6 Hz of low-pass filter; but in case of REGICA and AIR unfiltered EOG, data showed lowest errors. Moreover, Figure 4 depicts and compare the pure EEG and output EEG with different EOG filtering to analyze the effect of bidirectional contamination for time and frequency domain. It can be seen in Figure 4(a) through highlighted regions that different levels of distortions were introduced to EEG signal with different low-pass filtering of EOG signals. Specifically, when using high value low-pass filter (e.g., 35 Hz or unfiltered, magenta,

TABLE 3: Mean square error values (mean of all EEG channels and mean of all simulated subjects).

Low-pass EOG filter (Hz)	Simple		Adaptive filtering				Hybrid methods			
	Regression (mean \pm SD)		LMS (mean \pm SD)		RLS (mean \pm SD)		REGICA (mean \pm SD)		AIR (mean \pm SD)	
4	16.42	26.35	10.90	13.03	6.73	16.49	5.45	12.90	4.64	6.55
5	14.80	23.74	9.42	11.43	5.22	12.39	3.88	8.19	3.07	4.21
6	14.19	22.74	8.94	11.09	4.68	11.22	3.27	6.59	2.46	3.37
7	14.02	22.45	8.97	11.21	4.59	11.23	3.09	6.22	2.28	3.15
8	14.06	22.46	9.24	11.48	4.72	11.67	3.11	6.22	2.30	3.16
9	14.18	22.61	9.59	11.75	4.93	12.19	3.20	6.31	2.39	3.27
10	14.31	22.79	9.89	11.97	5.13	12.62	3.30	6.43	2.49	3.41
12	14.51	23.06	10.25	12.23	5.39	13.15	3.47	6.67	2.66	3.63
15	14.66	23.28	10.49	12.40	5.58	13.53	3.61	6.93	2.80	3.81
20	14.78	23.45	10.64	12.52	5.71	13.85	3.71	7.17	2.90	3.95
25	14.83	23.52	10.71	12.57	5.77	14.00	3.76	7.29	2.95	4.01
35	14.88	23.59	10.77	12.60	5.83	14.09	3.80	7.37	3.00	4.07
Unfiltered	15.00	23.78	10.91	12.71	5.95	14.18	3.92	7.48	3.12	4.24

TABLE 4: Mutual information scores (mean of all EEG channels and mean of all simulated subjects).

Low-pass EOG filter (Hz)	Simple		Adaptive filtering				Hybrid methods			
	Regression (mean \pm SD)		LMS (mean \pm SD)		RLS (mean \pm SD)		REGICA (mean \pm SD)		AIR (mean \pm SD)	
4	1.49	0.24	1.49	0.17	1.60	0.20	1.68	0.17	1.68	0.17
5	1.52	0.26	1.53	0.18	1.65	0.22	1.74	0.19	1.75	0.18
6	1.54	0.28	1.55	0.19	1.68	0.23	1.78	0.20	1.78	0.19
7	1.54	0.28	1.56	0.19	1.69	0.24	1.79	0.21	1.80	0.20
8	1.54	0.28	1.55	0.20	1.69	0.24	1.79	0.21	1.80	0.20
9	1.53	0.27	1.54	0.20	1.68	0.23	1.79	0.21	1.79	0.20
10	1.52	0.27	1.53	0.19	1.67	0.23	1.78	0.20	1.78	0.19
12	1.52	0.26	1.52	0.19	1.66	0.22	1.76	0.20	1.77	0.19
15	1.51	0.26	1.51	0.19	1.64	0.22	1.75	0.19	1.76	0.18
20	1.51	0.26	1.50	0.19	1.64	0.22	1.74	0.19	1.75	0.18
25	1.50	0.26	1.50	0.18	1.63	0.22	1.74	0.19	1.75	0.18
35	1.50	0.26	1.50	0.18	1.63	0.22	1.73	0.19	1.74	0.18
Unfiltered	1.49	0.25	1.49	0.18	1.62	0.21	1.73	0.18	1.73	0.18

and green line), the distortion in the neuronal signal is much more as compared to other low-pass filtering's (e.g., 7 Hz, blue line). It can be seen that the reconstructed EEG from 7 Hz low-pass filtering (blue line) follows the true EEG (black line) very closely as compared to all other outputs. Furthermore, Figure 4(b) illustrates the effect of bidirectional contamination in frequency domain. It can be seen through the highlighted box that artifact-free EEG with 7 Hz successfully recovered the frequencies similar to true EEG signal whereas all other produced distortion in the frequencies. This advocate our hypothesis that bidirectional contamination could be reduced by using optimal low-pass filtered EOG signals.

We used paired t -test to statistically compare results from all the metrics to find out if there are any differences in the outputs with different low-pass filtering. Before applying

paired t -test, as listed in Table 2, all EOG filtering frequencies used in this study were split into four classes which are 4 Hz (belongs to delta band), 5–8 Hz (belongs to theta band), 9–15 Hz (belongs to alpha and low-beta band), and 20 Hz–unfiltered (belongs to high-beta and gamma band). We divided this statistical testing into two steps. In the first step, we analyzed results of paired t -test to select an optimal low-pass filtering class which showed minimum errors with significantly increased results from all four classes as listed in Figure 5. Mean square errors obtained in the range of 5–8 Hz were lowest with 6.81 ± 11.21 (averaged for all methods) when compared to 4 Hz (8.83 ± 15.06 , $p < 0.027$), 9–15 Hz (7.14 ± 11.60 , nonsignificant difference), 20 Hz–unfiltered (7.65 ± 12.32 , $p < 0.1$ except for the LMS method). In case of frequency domain analysis in delta band, 5–8 Hz (MAE: 0.326 ± 0.14 ; MAPE: $3.89 \pm 2.30\%$; $p < 0.026$), 9–15 Hz

TABLE 5: Signal-to-artifact ratio for contaminated EEG, corrected EEG, and gain (mean of all EEG channels and mean of all simulated subjects).

Low-pass EOG filter (Hz)	SAR before artifact removal	Simple Regression		Adaptive filtering				Hybrid methods			
		(mean \pm SD)		LMS		RLS		REGICA		AIR	
		After	Gain	After	Gain	After	Gain	After	Gain	After	Gain
4		112.7	1.44	116.3	1.49	120.7	1.54	123.2	1.57	124.0	1.58
5		114.5	1.46	118.3	1.51	123.9	1.58	127.3	1.63	128.3	1.64
6		115.4	1.47	119.2	1.52	125.7	1.60	129.8	1.66	130.8	1.67
7		115.7	1.47	119.2	1.52	126.2	1.61	130.7	1.67	131.8	1.68
8		115.6	1.47	118.9	1.52	125.9	1.61	130.7	1.67	131.7	1.68
9		115.4	1.47	118.5	1.51	125.4	1.60	130.2	1.66	131.2	1.68
10	78.54	115.2	1.47	118.2	1.51	124.9	1.60	129.7	1.66	130.7	1.67
12		114.9	1.46	117.7	1.50	124.2	1.59	128.9	1.65	129.9	1.66
15		114.7	1.46	117.5	1.50	123.7	1.58	128.4	1.64	129.3	1.65
20		114.5	1.46	117.3	1.50	123.4	1.58	128.0	1.63	128.9	1.65
25		114.5	1.46	117.2	1.50	123.3	1.57	127.8	1.63	128.7	1.64
35		114.4	1.46	117.1	1.50	123.1	1.57	127.7	1.63	128.6	1.64
Unfiltered		114.2	1.46	116.9	1.49	122.8	1.57	127.2	1.62	128.1	1.64

TABLE 6: Mean absolute error (MAE) and mean absolute percentage error (MAPE) values in delta frequency band (mean of all EEG channels and mean of all simulated subjects).

Low-pass EOG filter (Hz)	Simple Regression		Adaptive filtering				Hybrid methods			
	(MAE, MAPE)		LMS		RLS		REGICA		AIR	
	MAE	MAPE	MAE	MAPE	MAE	MAPE	MAE	MAPE	MAE	MAPE
4	0.613	9.249	0.399	7.721	0.319	6.774	0.332	6.750	0.329	6.734
5	0.544	5.858	0.331	4.517	0.250	3.400	0.263	3.575	0.260	3.547
6	0.539	5.968	0.327	4.013	0.245	2.816	0.258	3.053	0.255	3.027
7	0.539	6.061	0.329	4.068	0.245	2.787	0.258	3.014	0.256	2.977
8	0.539	6.080	0.335	4.150	0.247	2.828	0.258	3.045	0.256	3.010
9	0.538	6.082	0.340	4.206	0.248	2.847	0.257	3.055	0.256	3.021
10	0.538	6.080	0.344	4.248	0.249	2.857	0.257	3.058	0.256	3.024
12	0.538	6.077	0.349	4.290	0.251	2.865	0.257	3.060	0.255	3.027
15	0.538	6.076	0.351	4.312	0.251	2.870	0.257	3.060	0.255	3.028
20	0.538	6.077	0.352	4.326	0.251	2.872	0.257	3.060	0.255	3.028
25	0.538	6.078	0.352	4.333	0.251	2.874	0.257	3.060	0.255	3.028
35	0.538	6.078	0.353	4.340	0.251	2.875	0.257	3.061	0.255	3.029
Unfiltered	0.538	6.083	0.353	4.392	0.251	2.889	0.257	3.059	0.255	3.027

(MAE: 0.329 ± 0.14 ; MAPE: $3.86 \pm 2.16\%$; $p < 0.10$), and 20 Hz-unfiltered (MAE: 0.330 ± 0.14 ; MAPE: $3.88 \pm 2.12\%$; $p < 0.159$) showed low errors when compared to 4 Hz (MAE: 0.398 ± 0.17 ; MAPE: $7.45 \pm 8.73\%$). There was a non-significant statistical difference observed when all other ranges were compared (5–8 Hz versus 9–15 Hz, $p < 0.589$; 5–8 Hz versus 20 Hz-unfiltered, $p < 0.518$; and 9–15 Hz versus 20 Hz-unfiltered, $p < 0.965$) for delta band. Five to eight Hz class (theta: MAE: 0.105 ± 0.03 ; MAPE: $3.44 \pm 5.27\%$; alpha: MAE: 0.023 ± 0.007 ; MAPE: $0.60 \pm 0.39\%$; beta: MAE: 0.004 ± 0.001 ; MAPE: $0.73 \pm 0.57\%$) showed highly significantly increased results for theta, alpha, and beta frequency bands when compared with 4 Hz (theta: MAE: 0.279 ± 0.14 ; MAPE: $10.35 \pm 13.66\%$; $p < 0.013$; alpha: MAE: $0.020 \pm$

0.007 ; MAPE: $0.70 \pm 0.60\%$; $p < 0.160$; beta: MAE: 0.006 ± 0.001 ; MAPE: $0.86 \pm 0.57\%$; $p < 0.053$), 9–15 Hz (theta: MAE: 0.134 ± 0.04 ; MAPE: $3.86 \pm 6.74\%$; $p < 0.031$; alpha: MAE: 0.11 ± 0.03 ; MAPE: $3.51 \pm 2.23\%$; $p < 0.001$; beta: MAE: 0.015 ± 0.004 ; MAPE: $2.23 \pm 1.84\%$; $p < 0.001$), and 20 Hz-unfiltered (theta: MAE: 0.143 ± 0.04 ; MAPE: $4.14 \pm 7.31\%$; $p < 0.016$; alpha: MAE: 0.171 ± 0.05 ; MAPE: $6.39 \pm 4.91\%$; $p < 0.001$; beta: MAE: 0.100 ± 0.03 ; MAPE: $15.93 \pm 11.40\%$; $p < 0.001$). In case of gamma band, 4 Hz (MAE: 0.028 ± 0.008 ; MAPE: $0.19 \pm 0.03\%$) showed significantly improved performance when compared with 20 Hz-unfiltered (MAE: 0.097 ± 0.03 ; MAPE: $0.99 \pm 1.06\%$; $p < 0.001$) and nonsignificant difference when compared with 9–15 Hz (MAE: 0.025 ± 0.01 ; MAPE: $0.11 \pm 0.04\%$; $p < 0.885$), but the

TABLE 7: Mean absolute error (MAE) and mean absolute percentage error (MAPE) values in theta frequency band (mean of all EEG channels and mean of all simulated subjects).

Low-pass EOG filter (Hz)	Simple		Adaptive filtering				Hybrid methods			
	Regression		LMS		RLS		REGICA		AIR	
	MAE	MAPE	MAE	MAPE	MAE	MAPE	MAE	MAPE	MAE	MAPE
4	0.281	10.048	0.280	10.386	0.278	10.401	0.279	10.449	0.278	10.446
5	0.145	5.536	0.141	6.120	0.138	6.030	0.137	6.042	0.137	6.040
6	0.093	3.590	0.088	3.605	0.085	3.409	0.081	3.359	0.081	3.354
7	0.094	2.020	0.092	1.879	0.087	1.589	0.082	1.484	0.083	1.468
8	0.113	3.292	0.111	2.590	0.106	2.531	0.099	2.435	0.100	2.448
9	0.130	4.134	0.128	3.395	0.122	3.317	0.114	3.205	0.116	3.231
10	0.140	4.511	0.138	3.764	0.132	3.677	0.124	3.565	0.125	3.593
12	0.149	4.753	0.147	4.009	0.140	3.910	0.131	3.794	0.133	3.824
15	0.151	4.816	0.150	4.084	0.142	3.979	0.133	3.853	0.135	3.884
20	0.152	4.827	0.150	4.108	0.142	3.999	0.134	3.863	0.135	3.894
25	0.152	4.829	0.150	4.113	0.143	4.003	0.134	3.864	0.135	3.895
35	0.152	4.829	0.150	4.116	0.143	4.006	0.134	3.864	0.135	3.895
Unfiltered	0.152	4.835	0.150	4.146	0.143	4.029	0.134	3.862	0.135	3.893

TABLE 8: Mean absolute error (MAE) and mean absolute percentage error (MAPE) values in alpha frequency band (mean of all EEG channels and mean of all simulated subjects).

Low-pass EOG filter (Hz)	Simple		Adaptive filtering				Hybrid methods			
	Regression		LMS		RLS		REGICA		AIR	
	MAE	MAPE	MAE	MAPE	MAE	MAPE	MAE	MAPE	MAE	MAPE
4	0.021	0.773	0.020	0.699	0.020	0.688	0.019	0.677	0.019	0.675
5	0.020	0.704	0.020	0.638	0.019	0.623	0.019	0.611	0.018	0.608
6	0.018	0.609	0.018	0.544	0.017	0.528	0.017	0.518	0.017	0.514
7	0.022	0.544	0.021	0.445	0.020	0.425	0.019	0.421	0.019	0.416
8	0.040	0.849	0.038	0.764	0.037	0.746	0.035	0.712	0.035	0.714
9	0.069	1.640	0.066	1.552	0.064	1.542	0.062	1.479	0.062	1.487
10	0.097	2.621	0.094	2.508	0.091	2.495	0.088	2.409	0.088	2.421
12	0.140	4.405	0.136	4.202	0.132	4.180	0.127	4.074	0.128	4.093
15	0.171	6.216	0.166	5.811	0.161	5.789	0.155	5.651	0.156	5.678
20	0.180	6.793	0.175	6.318	0.170	6.294	0.164	6.145	0.164	6.175
25	0.181	6.852	0.175	6.372	0.171	6.347	0.164	6.195	0.165	6.225
35	0.181	6.862	0.176	6.382	0.171	6.358	0.164	6.204	0.165	6.234
Unfiltered	0.181	6.865	0.176	6.387	0.171	6.360	0.164	6.204	0.165	6.235

errors were low for 5–8 Hz (MAE: 0.023 ± 0.009 ; MAPE: $0.10 \pm 0.04\%$; $p < 0.079$). Both 5–8 Hz and 9–15 Hz have nonsignificant differences for gamma band but showed statistically increased results when compared with 20 Hz–unfiltered ($p < 0.001$). Overall, in summary, 5–8 Hz outperformed 4 Hz for all metrics except for alpha band ($p < 0.079$) and when compared with 9–15 Hz and 20 Hz–unfiltered showed highly significantly increased results for theta, alpha, and beta bands ($p < 0.05$) and better results with nonsignificant difference for all other metrics. From this analysis, it can be concluded that 5–8 Hz perform better as compared to all other low-pass filtering classes. Next, we analyzed results of each low-pass frequency in 5–8 Hz range to check whether there is any single optimal frequency which showed

lowest errors with high-level of statistical significance (Figure 6). In this analysis, no significant differences were observed between most of the metrics when they compared statistically. However, outputs from 6 Hz (MSE: 6.70 ± 11.00 ; theta: MAE: 0.086 ± 0.02 , MAPE: $3.46 \pm 6.03\%$; beta: MAE: 0.004 ± 0.001 , MAPE: $0.72 \pm 0.56\%$; gamma: MAE: 0.023 ± 0.009 , MAPE: $0.098 \pm 0.03\%$) low-pass filter show significantly increased results when compared with 5 Hz (MSE: 7.28 ± 12.01 ; theta: MAE: 0.140 ± 0.06 , MAPE: $5.95 \pm 10.15\%$; beta: MAE: 0.005 ± 0.001 , MAPE: $0.77 \pm 0.56\%$; gamma: MAE: 0.024 ± 0.008 , MAPE: $0.10 \pm 0.03\%$) low-pass filter results with $p < 0.074$ in mean square error, theta, beta, and gamma bands (except for LMS in gamma band with nonsignificant difference), while in delta and alpha bands

TABLE 9: Mean absolute error (MAE) and mean absolute percentage error (MAPE) values in beta frequency band (mean of all EEG channels and mean of all simulated subjects).

Low-pass EOG filter (Hz)	Simple Regression		Adaptive filtering				Hybrid methods			
			LMS		RLS		REGICA		AIR	
	MAE	MAPE	MAE	MAPE	MAE	MAPE	MAE	MAPE	MAE	MAPE
4	0.007	1.018	0.007	1.122	0.005	0.794	0.005	0.679	0.005	0.676
5	0.007	0.959	0.006	1.039	0.005	0.703	0.004	0.573	0.004	0.573
6	0.007	0.938	0.006	0.982	0.004	0.646	0.003	0.510	0.003	0.506
7	0.007	0.944	0.006	0.961	0.004	0.637	0.003	0.491	0.003	0.486
8	0.007	1.003	0.006	0.987	0.004	0.678	0.003	0.519	0.003	0.512
9	0.007	1.128	0.007	1.074	0.005	0.768	0.004	0.595	0.004	0.588
10	0.009	1.367	0.008	1.228	0.007	0.930	0.006	0.790	0.006	0.784
12	0.016	2.410	0.016	2.336	0.014	2.057	0.013	1.917	0.013	1.916
15	0.034	5.027	0.034	5.208	0.033	4.925	0.031	4.719	0.031	4.725
20	0.066	10.752	0.067	11.173	0.065	10.705	0.062	10.381	0.062	10.405
25	0.094	15.951	0.095	16.437	0.092	15.767	0.089	15.289	0.089	15.324
35	0.122	18.770	0.124	19.315	0.121	18.521	0.117	17.945	0.117	17.996
Unfiltered	0.127	19.029	0.129	19.581	0.125	18.771	0.121	18.184	0.122	18.237

TABLE 10: Mean absolute error (MAE) and mean absolute percentage error (MAPE) values in gamma frequency band (mean of all EEG channels and mean of all simulated subjects).

Low-pass EOG filter (Hz)	Simple Regression		Adaptive filtering				Hybrid methods			
			LMS		RLS		REGICA		AIR	
	MAE	MAPE	MAE	MAPE	MAE	MAPE	MAE	MAPE	MAE	MAPE
4	0.037	0.159	0.034	0.146	0.026	0.110	0.021	0.091	0.020	0.088
5	0.034	0.146	0.031	0.133	0.022	0.095	0.018	0.075	0.017	0.071
6	0.033	0.141	0.030	0.129	0.021	0.089	0.016	0.068	0.015	0.064
7	0.033	0.140	0.031	0.130	0.021	0.089	0.016	0.066	0.015	0.062
8	0.033	0.141	0.031	0.134	0.022	0.092	0.016	0.067	0.015	0.063
9	0.034	0.142	0.032	0.138	0.022	0.095	0.016	0.069	0.015	0.065
10	0.034	0.143	0.033	0.141	0.023	0.098	0.017	0.071	0.016	0.067
12	0.034	0.144	0.034	0.144	0.024	0.102	0.017	0.073	0.016	0.069
15	0.034	0.145	0.034	0.146	0.024	0.104	0.018	0.075	0.017	0.071
20	0.034	0.146	0.035	0.148	0.025	0.106	0.018	0.077	0.017	0.073
25	0.035	0.156	0.036	0.161	0.026	0.119	0.019	0.090	0.018	0.087
35	0.046	0.270	0.047	0.281	0.037	0.242	0.031	0.214	0.030	0.211
Unfiltered	0.300	3.581	0.308	3.593	0.296	3.502	0.287	3.375	0.287	3.395

low significant differences were observed ($p < 0.153$). There was no significant difference observed between 6, 7, and 8 Hz except for theta and alpha band in 6 Hz versus 8 Hz ($p < 0.072$) and theta, alpha, and beta bands in 7 Hz versus 8 Hz ($p < 0.096$). It can be concluded that results from 6–8 Hz showed statistically increased results when compared with outputs from all other low-pass filtering and unfiltered EOG signals; but overall, there is no significant difference observed in 6–8 Hz except for few cases. Furthermore, these results advocate our hypothesis that unfiltered EOG signals cause high bidirectional contamination and low-pass filtering should be applied to EOG signals before using them in artifact removal algorithms.

In this study, we also used real EEG datasets to verify the efficacy of the proposed framework. The five algorithms

described above were applied separately to each subject's data to remove ocular artifacts with four low-pass EOG filtering. These EOG filtering (4 Hz, 7 Hz, 12 Hz, and UF) were chosen such that there is one low-pass filtering from each class (Table 2). We compared the classification accuracies obtained after the application of each method with each EOG low-pass filtering. In BCI studies, common spatial pattern (CSP) is the most commonly used filtering technique to extract features from EEG signals [63]. Generally, the goal of the CSP is to find spatial filters by maximizing the variance of one class while minimizing the variance of the other to discriminate the two populations of EEG signals [64]. Finally, we used linear discernment analysis (LDA) for classification of the extracted features of the two classes due to its simplicity and low computational cost. For each subject and each

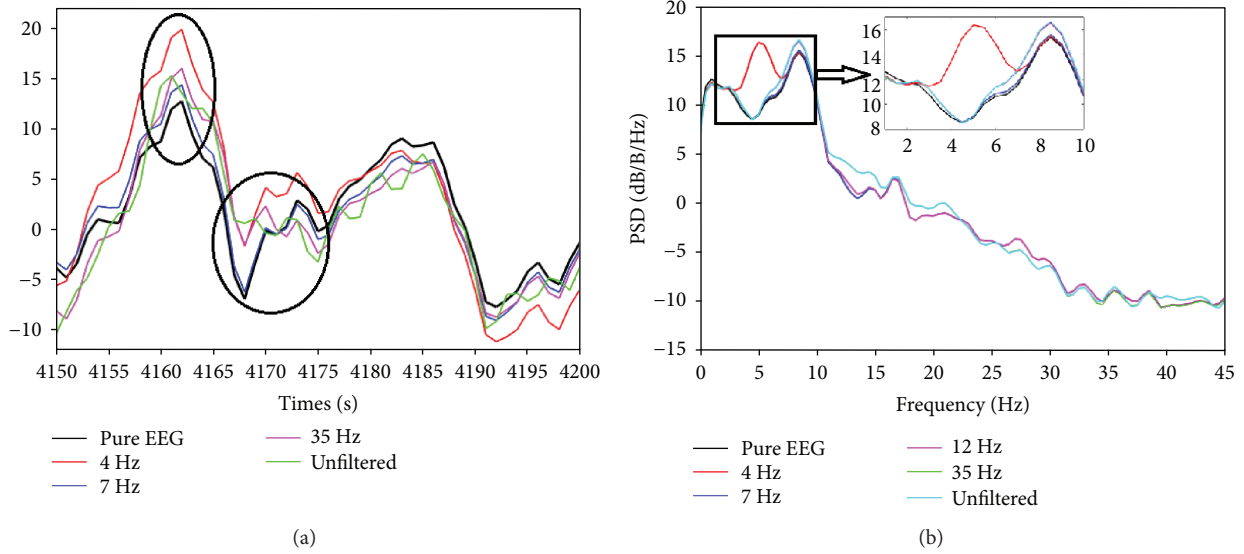


FIGURE 4: Analysis of bidirectional contamination by comparing reconstructed EEG obtained using different EOG low-pass filtering. (a) Time domain. (b) Frequency domain.

Class A Metrics	Class B															
	(5 6 7 8) Hz					(9 10 12 15) Hz					(20 25 35 UF) Hz					
	REG	LMS	RLS	REGICA	AIR	REG	LMS	RLS	REGICA	AIR	REG	LMS	RLS	REGICA	AIR	
4 Hz	MSE	0.007	0.027	0.013	0.007	0.007	0.009	0.477	0.095	0.009	0.008	0.012	0.915	0.256	0.011	0.010
	Delta	0.024	0.026	0.024	0.019	0.020	0.023	0.100	0.037	0.019	0.020	0.024	0.159	0.042	0.019	0.020
	Theta	0.013	0.013	0.012	0.011	0.011	0.033	0.032	0.030	0.024	0.025	0.039	0.038	0.034	0.027	0.029
	Alpha	<i>0.091</i>	<i>0.093</i>	0.117	0.160	0.158	0.002	0.001	0.001	0.001	0.001	0.001	0.001	0.001	0.001	0.001
	Beta	<i>0.053</i>	0.023	0.016	0.011	0.010	0.002	0.002	0.002	0.002	0.002	0.001	0.001	0.001	0.001	0.001
Gamma	0.023	<i>0.079</i>	0.024	0.013	0.010	0.037	0.885	0.323	0.024	0.016	0.001	0.001	0.001	0.001	0.001	
(5 6 7 8) Hz	MSE					<i>0.094</i>	0.286	0.274	0.156	0.152	0.010	0.167	0.096	0.004	0.004	
	Delta					<i>0.264</i>	0.272	0.589	0.132	0.221	0.342	0.232	0.518	<i>0.093</i>	0.168	
	Theta					0.028	0.022	0.025	0.031	0.030	0.016	0.013	0.014	0.016	0.016	
	Alpha					0.001	0.001	0.001	0.001	0.001	0.001	0.001	0.001	0.001	0.001	
	Beta					0.001	0.001	0.001	0.001	0.001	0.001	0.001	0.001	0.001	0.001	
Gamma					0.239	0.301	0.191	0.089	0.102	0.001	0.001	0.001	0.001	0.001	0.001	
(9 10 12 15) Hz	MSE										0.005	0.035	0.010	0.004	0.004	
	Delta										0.965	0.150	0.285	0.020	<i>0.054</i>	
	Theta										0.002	0.002	0.002	0.002	0.002	
	Alpha										0.002	0.002	0.002	0.002	0.002	
	Beta										0.001	0.001	0.001	0.001	0.001	
Gamma										0.001	0.001	0.001	0.001	0.001		

FIGURE 5: Statistical increases between different metrics for artifact corrections with different EOG filtering (paired t-tests were used between class A versus class B). Bold and underline: $p < 0.01$; Bold: $p < 0.05$; Italic: $p < 0.1$; Color indicate better class.

artifact-free EEG obtained after using different EOG filtering, 6 runs of 6-fold cross-validation were used to calculate the classification accuracies. The 6-fold cross-validation randomly divides the data into six equal partitions and use five set of partitions for training and 1 set of partition for testing. This process was repeated for six times, and the average accuracy for each subject was calculated. The average classification accuracies of each subjects for all six sessions with artifact-free EEG data using different low-pass EOG filtering, and each method are listed in Table 11. Similar to the results of simulated signals, it can be visualized from Table 11 that results from the candidate of class II low-pass filtering showed highest classification accuracies (REG: 69.52 ± 4.52 ; LMS: 73.45 ± 2.04 ; RLS: 73.99 ± 2.75 ; REGICA: 77.46 ± 3.59 ; AIR: 76.85 ± 3.27) for all subjects and all methods when compared with the results from the candidates of all other classes

(class I: REG: 66.43 ± 4.11 ; LMS: 70.13 ± 2.45 ; RLS: 70.83 ± 2.59 ; REGICA: 73.37 ± 3.64 ; AIR: 73.53 ± 4.71 ; class III: REG: 67.20 ± 6.09 ; LMS: 70.37 ± 2.84 ; RLS: 72.14 ± 4.65 ; REGICA: 74.53 ± 3.00 ; AIR: 73.30 ± 3.65 ; class IV: REG: 67.12 ± 3.75 ; LMS: 69.90 ± 2.40 ; RLS: 69.67 ± 4.48 ; REGICA: 73.07 ± 2.21 ; AIR: 72.91 ± 3.06). We further validated these results statistically using paired t -test. This analysis revealed that classification accuracies obtained with 7 Hz showed highly significant results when compared with outputs from 4 Hz ($p < 0.028$ for all methods), 12 Hz ($p < 0.01$ for LMS, REGICA, and AIR and $p < 0.163$ for REG and RLS), and unfiltered EOG ($p < 0.032$ for all methods). Furthermore, it could also be noted that hybrid methods demonstrated high-classification accuracies as compared to simple regression and adaptive filtering methods. These results from experimental EEG datasets verified the results from

Sub-Class A	Metrics	Sub-Class B														
		6 Hz					7 Hz					8 Hz				
		REG	LMS	RLS	REGICA	AIR	REG	LMS	RLS	REGICA	AIR	REG	LMS	RLS	REGICA	AIR
5 Hz	MSE	<u>0.008</u>	<u>0.038</u>	<u>0.018</u>	<u>0.009</u>	<u>0.009</u>	<u>0.009</u>	0.199	<u>0.047</u>	<u>0.010</u>	<u>0.010</u>	<u>0.012</u>	0.739	0.180	<u>0.011</u>	<u>0.011</u>
	Delta	0.105	0.114	0.112	0.118	0.120	0.152	0.640	0.268	0.149	0.166	0.157	0.633	0.592	0.151	0.177
	Theta	0.026	0.025	0.026	0.021	0.022	<i>0.060</i>	<i>0.054</i>	<i>0.055</i>	0.043	0.046	0.177	0.171	0.161	0.112	0.122
	Alpha	0.153	0.118	0.113	0.114	0.111	0.363	0.547	0.653	0.822	0.819	0.013	0.010	0.011	0.014	0.013
	Beta	<i>0.074</i>	0.026	0.018	0.013	0.011	<i>0.082</i>	<i>0.067</i>	0.025	0.011	0.010	0.254	0.449	0.127	0.023	0.020
	Gamma	0.046	0.158	0.035	0.021	0.016	<i>0.066</i>	0.665	0.132	0.031	0.020	<i>0.097</i>	0.828	0.530	0.047	0.027
6 Hz	MSE						0.017	0.898	0.387	0.014	0.014	<i>0.067</i>	0.496	0.848	0.026	0.026
	Delta						0.819	0.299	0.808	0.890	0.625	0.669	0.257	0.622	0.784	0.615
	Theta						0.769	0.504	0.619	0.841	0.762	<i>0.068</i>	0.044	<i>0.055</i>	<i>0.072</i>	<i>0.068</i>
	Alpha						0.092	0.135	0.168	0.230	0.222	0.008	0.005	0.006	0.008	0.007
	Beta						<i>0.138</i>	0.418	<i>0.092</i>	0.012	0.011	0.192	0.419	0.423	0.805	0.639
	Gamma						<i>0.241</i>	<i>0.622</i>	0.896	0.110	<i>0.060</i>	<i>0.724</i>	0.437	0.491	0.481	0.253
7 Hz	MSE											0.152	0.314	0.324	0.295	0.298
	Delta											0.481	0.260	0.516	0.486	0.600
	Theta											0.007	0.006	0.006	0.005	0.006
	Alpha											0.003	0.002	0.002	0.003	0.002
	Beta											0.020	<i>0.096</i>	0.034	0.010	0.012
	Gamma											0.258	0.328	0.227	0.139	0.149

FIGURE 6: Statistical increases between different metrics for artifact corrections with different EOG filtering of best class from Figure 5 (paired t-tests were used between subclass A versus subclass B). Bold and underline: $p < 0.01$; Bold: $p < 0.05$; Italic: $p < 0.1$; Color indicate better class.

simulated EEG signals that a low-pass EOG filtering from 6–8 Hz could be used to remove artifacts efficiently. As it can be seen from Table 11 that classification accuracies obtained from all low-pass filtered EOG are higher than those obtained when unfiltered EOG was used. From Figure 7, the t -testing also revealed that results from each low-pass filtering showed statistically increased classification accuracies as compared to the results from artifact-free EEG obtained after using unfiltered EOG signals. Therefore, these results also validate our hypothesis that low-pass filtering of EOG can be used to minimize the effect of bidirectional contamination problem.

4. Discussions

Many studies have shown that the performance of BCI applications can be reduced due to the presence of ocular artifacts in EEG data [23–27]. Among different methods, EOG-based algorithms are simple and fast due to which could be used as a good tool for real-time/online BCI applications if their performance is enhanced, since it is highly affected by bidirectional contamination [10, 44, 47, 51, 60]. The simplest solution to this problem is low-pass filtering EOG signals before using them in artifact removal algorithm [10, 39]. In efforts to overcome the effect of bidirectional contamination, a number of studies have applied different low-pass filtering on EOG signals ranging from 5 to 100 Hz, but there is no consensus on which low-pass frequency should be used for optimal results. The idea of low-pass filtering EOG is based on studies that have demonstrated that high-frequency components in EOG signals are generated from brain activities [52], and this is supported by some studies [10, 39, 43, 44, 47, 51]. It has been previously shown that performance of simple regression-based algorithms can be improved by using low-pass filtered EOG signals (7.5 Hz) as compared to unfiltered EOG signals [43]. Thus, the performance of EOG-based algorithms could be highly affected and dependent on the low-pass EOG signal

filtering. Various studies have utilized different low-pass frequencies for removal of ocular artifacts from EEG data [35, 43–45, 47, 51, 65, 66]. Table 1 lists the different low-pass filtering used in those studies, note though that in literature, there is still no evidence on the optimal low-pass frequency of EOG signals. In this light, it is very important to investigate the optimal low-pass filtering for EOG signals before using them in artifact removal process, not only for efficient removal/reduction of artifacts but also for enhancement of the classification accuracies and communication rates of the current BCI systems.

In this study, we used unfiltered and twelve different low-pass frequencies to filter simulated EOG signals before using them in artifact removal algorithm. The frequencies with their categorization used in this study are listed in Table 2. EOG-based five algorithms from simple [44], adaptive [45, 53], and hybrid [47, 51] categories have been chosen to investigate the task. The performance of each algorithm was evaluated in both the time and frequency domains in order to reach a conclusion for optimal low-pass filtering of EOG signals. In the time domain, the mean square error, mutual information scores, and gain in signal-to-artifact ratio were used as evaluation metrics [41, 61, 62], whereas in the frequency domain, the mean absolute error and mean absolute percentage error were employed [43, 51]. The results for each algorithm with each evaluation metric are shown in Tables 3–10. Time and frequency results indicate that there is a reduction of ocular artifacts by using low-pass filtering on EOG signals as compared to unfiltered EOG outputs. However, for some low-pass filtering, corrected EEG signals specifically from the frontal area (e.g., Fp1) showed distortion in the neuronal component of the EEG signals. Since we argued throughout the paper that optimal filtering will reduce the bidirectional contamination and hence will result in efficient removal of artifacts from EEG data, therefore, we tried to analyze the effect of bidirectional contamination in Figure 4. It can be seen that by using filtered EOG, specifically 7 Hz (blue line), the distortion in EEG for both time and

TABLE 11: Classification accuracies (mean of all six runs for each subject).

Low-pass EOG filter (Hz)	Sub	Simple	Adaptive filtering		Hybrid methods	
		Regression	LMS	RLS	REGICA	AIR
4	1	65.28	70.83	71.53	77.08	77.08
	2	61.11	73.61	66.67	78.47	80.56
	3	67.36	65.97	71.53	70.14	72.92
	4	64.58	66.67	69.44	69.44	71.53
	5	63.89	70.14	72.22	70.83	65.97
	6	63.19	70.14	70.83	70.83	69.44
	7	72.92	70.14	73.61	72.92	76.39
	8	66.67	72.22	67.36	72.22	70.14
	9	72.92	71.53	74.31	78.47	77.78
Mean \pm SD		66.43 \pm 4.11	70.13 \pm 2.45	70.83 \pm 2.59	73.37 \pm 3.64	73.53 \pm 4.71
7	1	69.44	72.92	79.17	81.25	81.25
	2	63.19	75.69	72.22	80.56	79.17
	3	73.61	72.92	72.92	75.69	75.00
	4	69.44	70.14	71.53	73.61	74.31
	5	64.58	72.22	75.69	73.61	71.53
	6	65.28	71.53	74.31	74.31	75.00
	7	73.61	76.39	76.39	76.39	79.86
	8	70.14	74.31	70.14	78.47	75.69
	9	76.39	75.00	73.61	83.33	79.86
Mean \pm SD		69.52 \pm 4.52	73.45 \pm 2.04	73.99 \pm 2.75	77.46 \pm 3.59	76.85 \pm 3.27
12	1	76.39	71.53	76.39	77.78	77.08
	2	57.64	71.53	70.14	72.22	75.69
	3	68.75	70.83	66.67	74.31	70.83
	4	66.67	68.75	65.28	72.92	68.06
	5	61.81	65.97	74.31	72.92	67.36
	6	61.81	69.44	75.00	72.92	73.61
	7	71.53	76.39	77.78	77.08	75.00
	8	66.67	68.75	68.06	70.83	75.69
	9	73.61	70.14	75.69	79.86	76.39
Mean \pm SD		67.20 \pm 6.09	70.37 \pm 2.84	72.14 \pm 4.65	74.53 \pm 3.00	73.30 \pm 3.65
UF	1	67.36	72.22	77.78	73.61	75.00
	2	65.28	70.83	68.06	70.83	75.69
	3	70.14	68.06	64.58	70.14	67.36
	4	67.36	70.14	65.97	71.53	73.61
	5	60.42	65.97	75.00	72.92	71.53
	6	63.19	66.67	70.14	73.61	71.53
	7	70.83	71.53	66.67	73.61	70.83
	8	67.36	71.53	66.67	73.61	72.92
	9	72.22	72.22	72.22	77.78	77.78
Mean \pm SD		67.12 \pm 3.75	69.90 \pm 2.40	69.67 \pm 4.48	73.07 \pm 2.21	72.91 \pm 3.06

frequency domain is very less as compared to that of when using unfiltered or high values of low-pass filtering (e.g., 35 Hz, green line) of EOG signals. Moreover, the effect of bidirectional contamination can also be analyzed by observing the errors obtained using different performance metrics, that is, lower the errors means less effect of bidirectional contamination. Furthermore, statistical testing is utilized by means of paired t -test to check any differences and

improvements between all low-pass filtering results. From time domain metrics, results of paired t -test were displayed only for mean square errors (mutual information and signal-to-artifact ratio also have similar results) and in the frequency domain for mean absolute errors of all frequency bands. In each low-pass filtering class, all the results were averaged before applying statistical testing. From Figure 5, the results of this statistical testing revealed that the

Group 1	Group 2														
	7 Hz					12 Hz					UF				
	REG	LMS	RLS	REGICA	AIR	REG	LMS	RLS	REGICA	AIR	REG	LMS	RLS	REGICA	AIR
4 Hz	0.016	0.015	0.028	0.003	0.022	0.624	0.859	0.352	0.368	0.851	0.467	0.813	0.482	0.800	0.681
7 Hz						0.153	0.024	0.162	0.069	0.010	0.031	0.015	0.025	0.024	0.031
12 Hz											0.959	0.624	0.149	0.157	0.759

FIGURE 7: Statistical increases between classification accuracies after artifact corrections with different EOG filtering (paired t -tests were used between group 1 versus group 2). Bold and underline: $p < 0.01$; Bold: $p < 0.05$; Italic: $p < 0.1$; Color indicate better class.

frequency class 5–8 Hz have low errors and statistically significant results as compared to all other frequency ranges with $p < 0.05$ in most of the cases (bold in purple color). Finally, we applied paired t -test on results of each low-pass frequency belonging to 5–8 Hz class to see whether there are any differences in the results with these low-pass filtering of EOG signals. The results of this analysis are listed in Figure 6. This testing revealed that, although in most of the cases, there are no significant differences in the results ($p > 0.1$), but 6–8 Hz EOG filtering shows statistically increased results as compared to 5 Hz low-pass filter ($p < 0.1$).

Although, simulated signals are the primary tool to analyze the performance of algorithms, but validation with real EEG signals is the ultimate goal specifically for applications like BCIs. We also used MI-based BCI signals to further validate the results obtained through the comprehensive analysis using simulated datasets. Four low-pass EOG filtering, one from each group defined in Table 2 was selected to analyze the effect of artifact removal on the classification accuracies of the MI-based BCI. Classification accuracies were used as an evaluation metric to verify the results, that is, higher the classification accuracies means that the corresponding low-pass EOG filtering could be used as an optimal frequency class to remove artifacts from EEG signals and to overcome the bidirectional contamination problem. It can be seen that all methods show best results when 7 Hz low-pass EOG filtering was used to remove ocular artifacts. Furthermore, statistical testing is utilized by means of paired t -test to check any differences and improvements between the classification accuracies obtained with each method and all low-pass filtering. The results of this analysis are shown in Figure 7. The results of this statistical testing revealed that the classification accuracies obtained after artifact removal from each method by using 7 Hz low-pass filtered EOG signals show a significant statistical increase as compared to 4 Hz, 12 Hz, and unfiltered EOG with $p < 0.05$ in most of the cases (bold in purple color). Furthermore, results from all low-pass EOG filtering showed statistically significant results when compared to the classification accuracies obtained after the application of unfiltered EOG signals. These results from experimental EEG data not only validate the outcomes from simulated datasets but also support our hypothesis that low-pass filtering should be applied to EOG signals before using them for artifact removal to reduce the effect of bidirectional contamination.

The main focus of this study was to analyze the effect of different low-pass filtering of EOG signals on the removal of ocular artifacts from EEG data, but the classification

accuracies for real EEG signals could be improved by incorporating more features and by using enhanced classifier. For instance, EEG signals can be divided into different sub-frequency bands to calculate more CSP features for each subband. Also, it has been shown previously that the performance of many other classifiers like support vector machine (SVM) is better than LDA but at the cost of more computations. Although the present investigation can be considered helpful in optimizing EOG signal filtering, the comprehensive comparison of the performances of other algorithms with no need of EOG signals for artifact removal still remains to be determined. Furthermore, the performances of BCI systems with EOG-based and non-EOG-based methods also should be investigated to conclude the optimal method for BCI applications. Therefore, in our future studies, we will use simulated and experimental EEG to evaluate artifact removal and BCI performance by including more methods like independent component analysis, canonical correlation analysis, empirical mode decomposition, and wavelet transform.

5. Conclusions

The optimal performance of a BCI depends on the effective removal/reduction of ocular artifacts from EEG recordings. Since the efficiency of an algorithm's removal of ocular activities is highly affected by bidirectional contamination, it is very important to use the optimal low-pass filtering for EOG signals in order to overcome/minimize the effect of bidirectional contamination. In the literature, there is still no evidence on the optimal low-pass frequency of EOG signals. In this study, we investigated the optimal EOG signal filtering for efficient removal of ocular artifacts from EEG data using fifteen artificially contaminated EEG and EOG datasets. Results from statistical testing of this investigation suggest that low-pass frequency from 6–8 Hz could be used as the optimal EOG signal filtering frequency for good results in terms of artifact removal and retrieval of true EEG signals. Furthermore, MI-based BCI datasets were utilized to validate the results of simulated signals. Classification accuracies obtained by class II showed statistically increased results as compared to results from all other classes. Moreover, the performance of each algorithm was enhanced by applying low-pass filtering to EOG signals before using them for artifact removal process. Overall, hybrid algorithms (REGICA and AIR) showed better performances as compared to regression and adaptive filtering methods for both simulated and experimental signals.

Data Availability

Data will be provided on request.

Conflicts of Interest

The authors declare that they have no conflicts of interest.

Acknowledgments

This work was supported by the National Research Foundation of Korea (NRF), grant funded by the Korean Government (MSIP) (Grant no. 2015R1A5A1037668).

References

- [1] M. A. Kamran, M. Y. Jeong, and M. M. N. Mannan, "Optimal hemodynamic response model for functional near-infrared spectroscopy," *Frontiers in Behavioral Neuroscience*, vol. 9, p. 151, 2015.
- [2] M. A. Kamran, M. M. N. Mannan, and M. Y. Jeong, "Cortical signal analysis and advances in functional near-infrared spectroscopy signal: a review," *Frontiers in Human Neuroscience*, vol. 10, p. 261, 2016.
- [3] D. Delisle-Rodriguez, A. C. Villa-Parra, T. Bastos-Filho et al., "Adaptive spatial filter based on similarity indices to preserve the neural information on EEG signals during on-line processing," *Sensors*, vol. 17, no. 12, article 2725, 2017.
- [4] Q. Liu, M. Ganzetti, N. Wenderoth, and D. Mantini, "Detecting large-scale brain networks using EEG: impact of electrode density, head modeling and source localization," *Frontiers in Neuroinformatics*, vol. 12, p. 4, 2018.
- [5] J. Shin, J. Kwon, and C.-H. Im, "A ternary hybrid EEG-NIRS brain-computer Interface for the classification of brain activation patterns during mental arithmetic, motor imagery, and idle state," *Frontiers in Neuroinformatics*, vol. 12, p. 5, 2018.
- [6] L. F. Nicolas-Alonso and J. Gomez-Gil, "Brain computer interfaces, a review," *Sensors*, vol. 12, no. 2, pp. 1211–1279, 2012.
- [7] A. Greco, N. Mammone, F. C. Morabito, and M. Versaci, "Kurtosis, Renyi's entropy and independent component scalp maps for the automatic artifact rejection from EEG data," *International Journal of Signal Processing*, vol. 2, no. 4, pp. 240–244, 2006.
- [8] N. Mammone and F. C. Morabito, "Enhanced automatic wavelet independent component analysis for electroencephalographic artifact removal," *Entropy*, vol. 16, no. 12, pp. 6553–6572, 2014.
- [9] M. Taherisadr, O. Dehzingi, and H. Parsaei, "Single channel EEG artifact identification using two-dimensional multi-resolution analysis," *Sensors*, vol. 17, no. 12, p. 2895, 2017.
- [10] J. A. Urigüen and B. Garcia-Zapirain, "EEG artifact removal—state-of-the-art and guidelines," *Journal of Neural Engineering*, vol. 12, no. 3, article 031001, 2015.
- [11] N. Mammone and F. C. Morabito, "Enhanced automatic artifact detection based on independent component analysis and Renyi's entropy," *Neural Networks*, vol. 21, no. 7, pp. 1029–1040, 2008.
- [12] N. Mammone, F. La Foresta, and F. C. Morabito, "Automatic artifact rejection from multichannel scalp EEG by wavelet ICA," *IEEE Sensors Journal*, vol. 12, no. 3, pp. 533–542, 2012.
- [13] T. Radüntz, J. Scouten, O. Hochmuth, and B. Meffert, "Automated EEG artifact elimination by applying machine learning algorithms to ICA-based features," *Journal of Neural Engineering*, vol. 14, no. 4, article 046004, 2017.
- [14] B. Somers, T. Francart, and A. Bertrand, "A generic EEG artifact removal algorithm based on the multi-channel Wiener filter," *Journal of Neural Engineering*, vol. 15, no. 3, article 036007, 2018.
- [15] D. B. Stone, G. Tamburro, P. Fiedler, J. Hauelsen, and S. Comani, "Automatic removal of physiological artifacts in EEG: the optimized fingerprint method for sports science applications," *Frontiers in Human Neuroscience*, vol. 12, p. 96, 2018.
- [16] P. Berg and M. Scherg, "Dipole modelling of eye activity and its application to the removal of eye artefacts from the EEG and MEG," *Clinical Physics and Physiological Measurement*, vol. 12, Supplement A, pp. 49–54, 1991.
- [17] O. Dimigen, W. Sommer, A. Hohlfeld, A. M. Jacobs, and R. Kliegl, "Coregistration of eye movements and EEG in natural reading: analyses and review," *Journal of Experimental Psychology: General*, vol. 140, no. 4, pp. 552–572, 2011.
- [18] G. L. Wallstrom, R. E. Kass, A. Miller, J. F. Cohn, and N. A. Fox, "Automatic correction of ocular artifacts in the EEG: a comparison of regression-based and component-based methods," *International Journal of Psychophysiology*, vol. 53, no. 2, pp. 105–119, 2004.
- [19] J. C. Corby and B. S. Kopell, "Differential contributions of blinks and vertical eye movements as artifacts in EEG recording," *Psychophysiology*, vol. 9, no. 6, pp. 640–644, 1972.
- [20] G. Gratton, M. G. Coles, and E. Donchin, "A new method for off-line removal of ocular artifact," *Electroencephalography and Clinical Neurophysiology*, vol. 55, no. 4, pp. 468–484, 1983.
- [21] J. Xie, G. Xu, A. Luo et al., "The role of visual noise in influencing mental load and fatigue in a steady-state motion visual evoked potential-based brain-computer Interface," *Sensors*, vol. 17, no. 8, p. 1873, 2017.
- [22] M. Ahn, H. Cho, S. Ahn, and S. C. Jun, "User's self-prediction of performance in motor imagery brain-computer Interface," *Frontiers in Human Neuroscience*, vol. 12, p. 59, 2018.
- [23] M. Fatourehchi, A. Bashashati, R. K. Ward, and G. E. Birch, "EMG and EOG artifacts in brain computer interface systems: a survey," *Clinical Neurophysiology*, vol. 118, no. 3, pp. 480–494, 2007.
- [24] A. Bashashati, B. Nouredin, R. K. Ward, P. Lawrence, and G. E. Birch, "Effect of eye-blinks on a self-paced brain interface design," *Clinical Neurophysiology*, vol. 118, no. 7, pp. 1639–1647, 2007.
- [25] A. Erfanian and B. Mahmoudi, "Real-time ocular artifact suppression using recurrent neural network for electroencephalogram based brain-computer interface," *Medical and Biological Engineering and Computing*, vol. 43, no. 2, pp. 296–305, 2005.
- [26] X. Yong, M. Fatourehchi, R. K. Ward, and G. E. Birch, "Automatic artefact removal in a self-paced hybrid brain-computer interface system," *Journal of NeuroEngineering and Rehabilitation*, vol. 9, no. 1, p. 50, 2012.
- [27] T. M. Vaughan, W. Heetderks, L. Trejo et al., "Brain-computer interface technology: a review of the second international meeting," *IEEE Transactions on Neural Systems and Rehabilitation Engineering*, vol. 11, no. 2, pp. 94–109, 2003.

- [28] D. Labate, F. La Foresta, N. Mammone, and F. C. Morabito, "Effects of artifacts rejection on EEG complexity in Alzheimer's disease," in *Advances in Neural Networks: Computational and Theoretical Issues*, Smart Innovation, Systems and Technologies, S. Bassis, A. Esposito, and F. Morabito, Eds., pp. 129–136, Springer, Cham, 2015.
- [29] N. Mammone, "Preprocessing the EEG of Alzheimer's patients to automatically remove artifacts," in *Multidisciplinary Approaches to Neural Computing*, A. Esposito, M. Faudez-Zanuy, F. Morabito, and E. Pasero, Eds., vol. 69 of Smart Innovation, Systems and Technologies, pp. 279–287, Springer, Cham, 2018.
- [30] C. Amo, L. de Santiago, R. Barea, A. López-Dorado, and L. Boquete, "Analysis of gamma-band activity from human EEG using empirical mode decomposition," *Sensors*, vol. 17, no. 5, p. 989, 2017.
- [31] A. H. H. Al-Nuaimi, E. Jammeh, L. Sun, and E. Ifeachor, "Complexity measures for quantifying changes in electroencephalogram in Alzheimer's disease," *Complexity*, vol. 2018, Article ID 8915079, 12 pages, 2018.
- [32] H. Cai, J. Han, Y. Chen et al., "A pervasive approach to EEG-based depression detection," *Complexity*, vol. 2018, Article ID 5238028, 13 pages, 2018.
- [33] R. J. Croft and R. J. Barry, "Removal of ocular artifact from the EEG: a review," *Neurophysiologie Clinique/Clinical Neurophysiology*, vol. 30, no. 1, pp. 5–19, 2000.
- [34] C. H. Brunia, J. Möcks, and M. M. C. van den Berg-Lenssen, "Correcting ocular artifacts in the EEG: a comparison of several models," *Journal of Psychophysiology*, vol. 3, pp. 1–50, 1989.
- [35] R. J. Croft and R. J. Barry, "EOG correction: a new perspective," *Electroencephalography and Clinical Neurophysiology*, vol. 107, no. 6, pp. 387–394, 1998.
- [36] R. J. Croft and R. J. Barry, "EOG correction: a new aligned-artifact average solution," *Clinical Neurophysiology*, vol. 107, no. 6, pp. 395–401, 1998.
- [37] R. J. Croft and R. J. Barry, "EOG correction: which regression should we use?," *Psychophysiology*, vol. 37, no. 1, pp. 123–125, 2000.
- [38] R. J. Croft, J. S. Chandler, R. J. Barry, N. R. Cooper, and A. R. Clarke, "EOG correction: a comparison of four methods," *Psychophysiology*, vol. 42, no. 1, pp. 16–24, 2005.
- [39] F. Ghaderi, S. K. Kim, and E. A. Kirchner, "Effects of eye artifact removal methods on single trial P300 detection, a comparative study," *Journal of Neuroscience Methods*, vol. 221, pp. 41–47, 2014.
- [40] G. Gratton, "Dealing with artifacts: the EOG contamination of the event-related brain potential," *Behavior Research Methods, Instruments, & Computers*, vol. 30, no. 1, pp. 44–53, 1998.
- [41] H. Peng, B. Hu, Q. Shi et al., "Removal of ocular artifacts in EEG—an improved approach combining DWT and ANC for portable applications," *IEEE journal of biomedical and health informatics*, vol. 17, no. 3, pp. 600–607, 2013.
- [42] T. T. Pham, R. J. Croft, P. J. Cadusch, and R. J. Barry, "A test of four EOG correction methods using an improved validation technique," *International Journal of Psychophysiology*, vol. 79, no. 2, pp. 203–210, 2011.
- [43] S. Romero, M. Mañanas, and M. J. Barbanaj, "Ocular reduction in EEG signals based on adaptive filtering, regression and blind source separation," *Annals of Biomedical Engineering*, vol. 37, no. 1, pp. 176–191, 2009.
- [44] S. Romero, M. A. Mañanas, and M. J. Barbanaj, "A comparative study of automatic techniques for ocular artifact reduction in spontaneous EEG signals based on clinical target variables: a simulation case," *Computers in Biology and Medicine*, vol. 38, no. 3, pp. 348–360, 2008.
- [45] P. He, G. Wilson, and C. Russell, "Removal of ocular artifacts from electro-encephalogram by adaptive filtering," *Medical and Biological Engineering and Computing*, vol. 42, no. 3, pp. 407–412, 2004.
- [46] M. K. Islam, A. Rastegarnia, and Z. Yang, "Methods for artifact detection and removal from scalp EEG: a review," *Neurophysiologie Clinique/Clinical Neurophysiology*, vol. 46, no. 4–5, pp. 287–305, 2016.
- [47] M. A. Klados, C. Papadelis, C. Braun, and P. D. Bamidis, "REG-ICA: a hybrid methodology combining blind source separation and regression techniques for the rejection of ocular artifacts," *Biomedical Signal Processing and Control*, vol. 6, no. 3, pp. 291–300, 2011.
- [48] B. Jervis, E. Ifeachor, and E. Allen, "The removal of ocular artefacts from the electroencephalogram: a review," *Medical and Biological Engineering and Computing*, vol. 26, no. 1, pp. 2–12, 1988.
- [49] P. Sadasivan and D. N. Dutt, "ANC schemes for the enhancement of EEG signals in the presence of EOG artifacts," *Computers and Biomedical Research*, vol. 29, no. 1, pp. 27–40, 1996.
- [50] M. M. N. Mannan, S. Kim, M. Y. Jeong, and M. A. Kamran, "Hybrid EEG—eye tracker: automatic identification and removal of eye movement and blink artifacts from electroencephalographic signal," *Sensors*, vol. 16, no. 2, p. 241, 2016.
- [51] M. M. N. Mannan, M. Y. Jeong, and M. A. Kamran, "Hybrid ICA—regression: automatic identification and removal of ocular artifacts from electroencephalographic signals," *Frontiers in Human Neuroscience*, vol. 10, p. 193, 2016.
- [52] T. Gasser, P. Ziegler, and W. F. Gattaz, "The deleterious effect of ocular artefacts on the quantitative EEG, and a remedy," *European Archives of Psychiatry and Clinical Neuroscience*, vol. 241, no. 6, pp. 352–356, 1992.
- [53] A. G. Correa, E. Laciari, H. Patiño, and M. Valentinuzzi, "Artifact removal from EEG signals using adaptive filters in cascade," *Journal of Physics: Conference Series*, vol. 90, article 012081, 2007.
- [54] T. Elbert, W. Lutzenberger, B. Rockstroh, and N. Birbaumer, "Removal of ocular artifacts from the EEG—a biophysical approach to the EOG," *Clinical Neurophysiology*, vol. 60, no. 5, pp. 455–463, 1985.
- [55] A. Schlögl, C. Keinrath, D. Zimmermann, R. Scherer, R. Leeb, and G. Pfurtscheller, "A fully automated correction method of EOG artifacts in EEG recordings," *Clinical Neurophysiology*, vol. 118, no. 1, pp. 98–104, 2007.
- [56] M. Tangermann, K.-R. Müller, A. Aertsen et al., "Review of the BCI competition IV," *Frontiers in Neuroscience*, vol. 6, p. 55, 2012.
- [57] D. Wang, D. Miao, and G. Blohm, "Multi-class motor imagery EEG decoding for brain-computer interfaces," *Frontiers in Neuroscience*, vol. 6, no. 151, 2012.
- [58] N. P. Castellanos and V. A. Makarov, "Recovering EEG brain signals: artifact suppression with wavelet enhanced independent component analysis," *Journal of Neuroscience Methods*, vol. 158, no. 2, pp. 300–312, 2006.
- [59] Y. Tran, A. Craig, P. Boord, and D. Craig, "Using independent component analysis to remove artifact from

- electroencephalographic measured during stuttered speech,” *Medical and Biological Engineering and Computing*, vol. 42, no. 5, pp. 627–633, 2004.
- [60] K. T. Sweeney, T. E. Ward, and S. F. McLoone, “Artifact removal in physiological signals—practices and possibilities,” *IEEE Transactions on Information Technology in Biomedicine*, vol. 16, no. 3, pp. 488–500, 2012.
- [61] H. Ghandeharion and A. Erfanian, “A fully automatic ocular artifact suppression from EEG data using higher order statistics: improved performance by wavelet analysis,” *Medical Engineering and Physics*, vol. 32, no. 7, pp. 720–729, 2010.
- [62] J. J. Kierkels, G. J. van Boxtel, and L. L. Vogten, “A model-based objective evaluation of eye movement correction in EEG recordings,” *IEEE Transactions on Biomedical Engineering*, vol. 53, no. 2, pp. 246–253, 2006.
- [63] H. Lu, H.-L. Eng, C. Guan, K. N. Plataniotis, and A. N. Venetsanopoulos, “Regularized common spatial pattern with aggregation for EEG classification in small-sample setting,” *IEEE Transactions on Biomedical Engineering*, vol. 57, no. 12, pp. 2936–2946, 2010.
- [64] H. Ramoser, J. Muller-Gerking, and G. Pfurtscheller, “Optimal spatial filtering of single trial EEG during imagined hand movement,” *IEEE Transactions on Rehabilitation Engineering*, vol. 8, no. 4, pp. 441–446, 2000.
- [65] P. Sadasivan and D. N. Dutt, “Development of Newton-type adaptive algorithm for minimization of EOG artefacts from noisy EEG signals,” *Signal Processing*, vol. 62, no. 2, pp. 173–186, 1997.
- [66] R. J. Croft and R. J. Barry, “Issues relating to the subtraction phase in EOG artefact correction of the EEG,” *International Journal of Psychophysiology*, vol. 44, no. 3, pp. 187–195, 2002.
- [67] A. K. Maddirala and R. A. Shaik, “Removal of EOG artifacts from single channel EEG signals using combined singular spectrum analysis and adaptive noise canceler,” *IEEE Sensors Journal*, vol. 16, no. 23, pp. 1–8287, 2016.
- [68] B. Yang, K. Duan, and T. Zhang, “Removal of EOG artifacts from EEG using a cascade of sparse autoencoder and recursive least squares adaptive filter,” *Neurocomputing*, vol. 214, pp. 1053–1060, 2016.
- [69] S. Kanoga, M. Nakanishi, and Y. Mitsukura, “Assessing the effects of voluntary and involuntary eyeblinks in independent components of electroencephalogram,” *Neurocomputing*, vol. 193, pp. 20–32, 2016.
- [70] Z. Wang, P. Xu, T. Liu, Y. Tian, X. Lei, and D. Yao, “Robust removal of ocular artifacts by combining independent component analysis and system identification,” *Biomedical Signal Processing and Control*, vol. 10, pp. 250–259, 2014.
- [71] H. Zeng, A. Song, R. Yan, and H. Qin, “EOG artifact correction from EEG recording using stationary subspace analysis and empirical mode decomposition,” *Sensors*, vol. 13, no. 11, pp. 14839–14859, 2013.
- [72] R. Sameni and C. Gouy-Pailler, “An iterative subspace denoising algorithm for removing electroencephalogram ocular artifacts,” *Journal of Neuroscience Methods*, vol. 225, pp. 97–105, 2014.
- [73] M. K. GN and K. Z. Ahmed, “Correction of ocular artifacts in EEG signal using empirical mode decomposition and cross-correlation,” *Research Journal of Biotechnology*, vol. 9, p. 12, 2014.
- [74] H.-L. Chan, Y.-T. Tsai, L.-F. Meng, and T. Wu, “The removal of ocular artifacts from EEG signals using adaptive filters based on ocular source components,” *Annals of Biomedical Engineering*, vol. 38, no. 11, pp. 3489–3499, 2010.
- [75] S. Puthusserypady and T. Ratnarajah, “Robust adaptive techniques for minimization of EOG artefacts from EEG signals,” *Signal Processing*, vol. 86, no. 9, pp. 2351–2363, 2006.
- [76] D. Moretti, F. Babiloni, F. Carducci et al., “Computerized processing of EEG–EOG–EMG artifacts for multi-centric studies in EEG oscillations and event-related potentials,” *International Journal of Psychophysiology*, vol. 47, no. 3, pp. 199–216, 2003.

Research Article

A Wavelet-Based Correlation Analysis Framework to Study Cerebromuscular Activity in Essential Tremor

Yifan Zhao ¹, Ramon C. Laguna,² Yitian Zhao ³, Jimmy Jiang Liu,³ Xiongxiang He,⁴ John Yianni,⁵ and Ptolemaios G. Sarrigiannis⁵

¹Through-life Engineering Services Centre, Cranfield University, Bedfordshire MK43 0AL, UK

²Computational and Software Techniques in Engineering, Cranfield University, Bedfordshire MK43 0AL, UK

³Cixi Institute of Biomedical Engineering, Ningbo Institute of Industrial Technology, Chinese Academy of Sciences, Ningbo, China

⁴Information Engineering, Zhejiang University of Technology, Hangzhou 310023, China

⁵Department of Neurosciences, Sheffield Teaching Hospitals, NHS Foundation Trust, Royal Hallamshire Hospital, Sheffield S10 2JF, UK

Correspondence should be addressed to Yifan Zhao; yifan.zhao@cranfield.ac.uk and Yitian Zhao; yitian.zhao@bit.edu.cn

Received 12 February 2018; Revised 23 April 2018; Accepted 22 May 2018; Published 3 July 2018

Academic Editor: Nadia Mammone

Copyright © 2018 Yifan Zhao et al. This is an open access article distributed under the Creative Commons Attribution License, which permits unrestricted use, distribution, and reproduction in any medium, provided the original work is properly cited.

Objective. Deep brain stimulation (DBS) provides dramatic tremor relief in patients with severe essential tremor (ET). Typically, the VIM nucleus is the most effective brain area to target for high-frequency electrical stimulation in these patients. Correlation analysis between electrical local field potential (LFP) recordings from the thalamic DBS leads and electrical muscle activity from the contralateral tremulous limb has become an attractive practical tool to interpret the LFPs and their association with the tremulous clinical manifestations. Although functional connectivity analysis between brain electrical recordings and electromyographic (EMG) signals from the tremor has been of interest to an increasing number of engineering researchers, there is no well-accepted tailored framework to consistently characterise the association between thalamic electrical recordings and the tremorogenic EMG activity. **Methods.** This paper proposes a novel framework to address this challenge, including an estimation of the interaction strength using wavelet cross-spectrum and phase lag index while demonstrating the statistical significance of the findings. **Results.** Consistent results were estimated for single and multiple trials of consecutive or partially overlapping epochs of data. The latter approach reveals a substantial increase on the range of statistically significant dynamic low-frequency interrelationships while decreasing the dynamic range of high-frequency interactions. **Conclusion.** Results from both simulation and real data demonstrate the feasibility and robustness of the proposed framework. **Significance.** This study offers the proof of principle required to implement this methodology to uncover VIM thalamic LFP-EMG interactions for (i) better understanding of the pathophysiology of tremor; (ii) objective selection of the DBS electrode contacts with the highest strength of association with the tremorogenic EMG, a particularly useful feature for the implementation of novel multicontact directional leads in clinical practice; and (iii) future research on DBS closed-loop devices.

1. Introduction

Essential tremor (ET) is defined as a neurological disorder that causes involuntary abnormal repetitive shaking. This shaking can appear in different parts of the body such as the hands, forearms, or head [1]. ET is a common movement disorder affecting around four out of 100 adults over 40 years of age. It is considered to be a centrally driven tremor, and the constituents of the network comprise anatomical areas of the

physiological motor system [2]. Treatment of ET is mainly based on pharmacotherapy and surgery for medically refractory cases [3]. The main surgical approach currently in use consists of continuous deep brain stimulation (DBS) through implantation of a depth electrode in the area of the ventral intermediate (VIM) nucleus of the thalamus, a key area in the neuronal loop generating the tremor [3, 4]. The depth electrodes after DBS surgery emit continuous electrical signals coming from the neurostimulator or pacemaker [5].

To confirm electrode position within the VIM thalamic nucleus, in addition to neuronavigation techniques to target this specific anatomical area, some centres perform micro-electrode recordings during surgery to detect tremor-related electric neuronal bursts and find the ideal position for electrode implantation [6]. Through the routinely used macro-electrodes in DBS surgery, neuronal network electrical activity can be recorded from the VIM thalamus in the form of local field potentials (LFPs) a few days after surgery.

2. Material

In this study, we use recordings from two patients (aged 64 and 53, both female) who underwent DBS surgery for medically refractory ET. Ethics approval for use of patients' EEGs and LFPs for the development of new quantitative EEG (qEEG) methods was obtained both from the University of Sheffield and the NHS ethics committees (SMBRER207 and 11/YH/0414). The multichannel Natus Quantum Amplifier (Optima Medical Ltd.) at a sampling rate of 16,384 Hz was used for all EEG/LFP/EMG polygraphy recordings (analogue bandwidth 0.01–4000 Hz).

In our institution (Royall Hallamshire Hospital, Sheffield Teaching Hospitals, NHS Foundation Trust), every patient undergoing DBS surgery for tremor is offered, five days after implantation of the depth electrodes, a comprehensive electrophysiological analysis to include LFPs from the VIM thalamus, electroencephalography (EEG), and electromyographic (EMG) polygraphy recordings, measuring the electrical activity from the muscles, to look at the correlation between the tremor and the thalamic network oscillations. The cortical scalp EEG recordings are not used in this work. There are four electrode contacts on each macroelectrode placed in the thalamus in close proximity to each other (contacts 0, 1, 2, and 3) through which bipolar recordings of LFPs can be obtained. Many centres use an empirical approach in selecting the ideal electrode contact to stimulate after DBS surgery to obtain the ideal tremor suppression. This approach can be time-consuming, and it will become more of a problem as new multicontact directional leads make their way into clinical practice [7]. Additionally, it seems that the LFPs offer very significant information which in the future could be used to optimise clinical outcomes in closed-loop systems [8]. However, before this becomes possible, an objective measure of the strength of association between the VIM thalamic network and the tremor recorded on EMG, or the equivalent mechanical oscillations through accelerometers, is required. One practical solution is based on the correlation analysis between data coming from the DBS leads (LFP) and electrical muscular activity (EMG) of the tremulous limb. Corticomuscular functional connectivity is defined as the interaction between the electrical activity of the cortex in the brain or the thalamus in this instance and the electrical activity recorded from various muscles. During the last few years, a few methods have been developed to understand this type of functional connectivity [9–11].

From the engineering perspective, the approaches to study connectivity between two signals can be classified as

time- and frequency-domain-based methods. One of the classic linear measures to estimate similarity in time domain is cross-correlation that has been used to study ET [12]. It measures the degree of connectivity when a time series is shifted from other reference series. This method is also useful to measure the time lag between two signals. However, this method usually assumes that the system is linear and stationary. Another branch to quantify the correlation or causality between signals in time domain is by mutually predicting selected observable measurements based on multivariate modelling, where the best-established methods are based on the Granger causality test [13] that has been used to study the correlation between EEG signals [14]. They are based on parametric modelling. A full and unbiased model is therefore required, which can be a challenge to achieve due to the limited knowledge on the human brain. Other nonparametric methods include mutual information [15] and transfer entropy [16, 17], which are model-free but usually require larger datasets or averaging over many realisations to mitigate the effects of noise. In the scope of frequency-based methods, cross-spectrum allows determining the connection between two stationary signals in terms of frequency [18]. When computing complex cross-spectrum, results can be divided in cospectrum (in-phase connectivity) and quad-spectrum (out-of-phase connectivity). Coherence [19, 20] uses a normalisation of cross-spectrum values that takes unit value when total linear phase relationship is detected or zero value for independent signals. Both methods are easy-to-use and computationally inexpensive, but the investigated correlation must be stationary and linear and there is no-coupling information among various frequencies. Cross-bispectrum [21] is used to detect the quadratic phase coupling (QPC) between frequency components of two target signals. One pitfall of this algorithm is that bispectrum is affected not only by nonlinearity but also by non-Gaussian data. Thus, it requires the data to present Gaussian distribution to make sure to detect nonlinearity. A suitable approach to overcome these non-phase-coupling peaks is through cross-bicoherence [22]. However, this method only favours the strongly phase-coupled signals, the ones that show QPC interactions.

In addition to the frequency- and time-based approaches, efforts have been made with the wavelet domain to study connectivity of brain networks. This approach aims to address limitations of the above methods on tackling dynamic systems by providing time-resolving value with accurate locality. Meanwhile, it is a model-free (nonparametric) measure, which reduces the requirement of a priori knowledge of the underlying model. Wavelet coherence has attracted increased interest on studying brain-related disorders. Jeong et al. [23] proposed to use wavelet energy and wavelet coherence as EEG biomarkers to distinguish Parkinson's disease and Alzheimer's disease. A wavelet coherence-based clustering of EEG signals has been developed to estimate the brain connectivity in absence epileptic patients [24]. It has also been applied to studies on autism [25], traumatic brain injury [26], schizophrenia [27], and poor sleep quality [28]. However, there is very limited research focusing on its application on ET. Furthermore, for the approaches based on wavelet coherence to understand brain connectivity, there are no

well-accepted complete frameworks to understand cerebro-muscular connectivity systematically.

Addressing these challenges, this paper develops a new wavelet-based correlation analysis framework combined by the estimation of connectivity strength, significance test, and phase-delay characterisation. It aims to better understand cerebro-muscular interactions in a structured manner. It should be noted that this framework has the prospect to be applied on other applications of connectivity analysis, such as EEG-EEG and EEG-EMG.

3. Methods

Model-free (nonparametric) measures are chosen in this paper to study the correlation between LFPs and EMG because this biological system is so complex that it would require a substantial number of parameters and computation time to build a satisfactory parametric model. Additionally, there is no well-accepted analytical model to start with. A common deficiency when applying biomedical signal-processing tools is the assumption of stationarity. A typical practice for the estimation of spectrum distribution is segmenting long records of data and averaging calculations over segments. The main disadvantage of this practice is the inability of having time-resolved values. There is therefore no time resolution, and the dynamic behaviour of neuronal interactions cannot be revealed. One solution to overcome this issue is the use of wavelets.

Wavelet transformation makes a decomposition of a time series into a frequency-time domain. It uses convolution of a mother wavelet and its scaled and shifted versions. Among all the possible mother wavelets, the *Morlet* wavelet provides a good balance between frequency and time resolution and has been widely used in EEG and EMG research [29]. This study is restricted to this wavelet. Equation (1) corresponds with a normalised *Morlet* wavelet where the dimensionless frequency w_0 is set as 6 and dimensionless time is denoted by η . Considering an observed time-serial $x(k)k = 1, \dots, N$, in continuous wavelet transform (CWT), the mother wavelet is modified by varying the scale s , as shown in (2), so that $\eta = s \cdot t$ with a discretised time domain of time step δt .

$$\Psi_0(\eta) = \pi^{1/4} e^{iw_0\eta} e^{-(1/2)\eta^2}, \quad (1)$$

$$W_k^x(s) = \sqrt{\frac{\delta t}{s}} \sum_{k'=1}^N x_k \Psi_0 \left[\frac{(k-k')\delta t}{s} \right]. \quad (2)$$

3.1. Wavelet Coherence. Coherence is one of the most widely used methods for measuring linear interactions. It is based on the Pearson correlation coefficient used in statistics but in frequency and time domain. It measures the mean resultant vector length (or consistency) of the cross-spectral density between two signals. Its squared value varies from 0 to 1, meaning low and high linear frequential correlation. During this study, coherence is used as a reference standard for comparison to other methods. The wavelet formulation of

coherence between two signals, x and y , and in the frequency w and time t domain, can be formulated as

$$\text{coh}_{xy}^2(w, t) = \frac{|S_{xy}(w, t)|^2}{S_x(w, t)S_y(w, t)}, \quad (3)$$

$$S_{xy}(w, t) = \mathbb{E} \left(W_x(w, t) \overline{W_y(w, t)} \right),$$

where $S_{xy}(w, t)$ is the wavelet cross-spectrum between x and y and $S_x(w, t)$ and $S_y(w, t)$ are the corresponding autospectrums. Working with two single signals (single realisation) usually requires using a smoothing operator (see $f(\cdot)$ operator in (4)), and ergodicity properties should be assumed [30].

$$\widehat{\text{coh}}_{xy}^2(w, t) = \frac{|f(S_{xy}(w, t))|^2}{f(S_x(w, t)) \cdot f(S_y(w, t))}. \quad (4)$$

If multiple trials of both signals are available, square coherence can be estimated using (5), which is used in this study.

$$\widehat{\text{coh}}_{xy}^2(w, t) = \frac{|\widehat{S}_{xy}(w, t)|^2}{\widehat{S}_x(w, t)\widehat{S}_y(w, t)}, \quad (5)$$

where

$$\widehat{S}_{xy}(w, t) = \frac{1}{n} \sum_{m=1}^n W_{x_m}(w, t) \overline{W_{y_m}(w, t)}. \quad (6)$$

The number of trials is denoted by n .

To assert significant values of wavelet coherence, the statistical methodology established by Gallego et al. [31] is employed. It estimates a threshold based on the null hypothesis (H_0) of independency by analytically calculating the statistical distribution of coherence. Specifically, H_0 assumes that both signals are independent Gaussian variables. Under H_0 , $\widehat{\text{coh}}_{xy}^2(w, t) \leq r_\alpha$ with a specified probability α , where r_α is calculated as

$$r_\alpha = 1 - \alpha^{1/(n-1)}, \quad 0 \leq \alpha \leq 1. \quad (7)$$

In this paper, the parameter α is set as a fixed value of 0.05, equivalent to a 95% of confidence interval.

3.2. Wavelet Cross-Spectrum. Wavelet cross-spectrum (WCS) also provides information about linear synchronisation, but its values are not normalised as in wavelet coherence. Its calculation is written in (6) for multiple trials. Its values seem difficult to be interpreted by statisticians and complementary plots, such as coherence or coquadrature, that can help understand the frequential relationships between signals [9]. That is why few neurological connectivity studies have used this method. However, this paper proposes to use an appropriate significant test that allows WCS results to be judged with more clarity by including the variance of each signal.

It has been proven by Bigot et al. [32] that including the variance spectrum data (autospectrum) $\widehat{S}_x(w, t)$ and $\widehat{S}_y(w, t)$

benefits the interpretation of WCS in contrast to wavelet coherence. Its performance is based, analogously to coherence, on a threshold calculation under a null hypothesis. However, this H_0 makes the statistical procedure using a combination of parametric and nonparametric estimations. It has parametric characteristics since it establishes the signals as independent Gaussian vectors. But its distribution is considered to show a zero-mean value and a general covariance matrix \sum_x and \sum_y estimated by the sampled data. Hence, it does not make any parametric assumption on the covariance. The statistical test establishes, under $H_0(\sum_x, \sum_y)$ and $n \geq 1$, that $P(|\widehat{S}_{xy}(w, t)| \geq \lambda_\alpha) \leq \alpha$. The threshold λ_α , for each time t and frequency w point, is defined as

$$\lambda_\alpha(w, t) = \frac{\rho_x \rho_y}{n} \cdot \|\Psi_{w,t}\| \cdot \left(-\log\left(\frac{\alpha}{2}\right) + \sqrt{-2n \log\left(\frac{\alpha}{2}\right)} \right), \quad (8)$$

where ρ_x and ρ_y are the largest eigenvalues of the empirical covariance matrix of the time series x and y , respectively. The symbol $\|\Psi_{w,t}\|$ means the energy of the wavelet, but since wavelet-normalised values are considered, this variable is omitted. This paper considers a significant probability of 95% with $\alpha = 0.05$.

3.3. Phase Lag Characterisation. Apart from the quantification of the linear interaction strength and associated significance, it is also important to measure the time or phase lag between signals at a certain frequency. It is particularly important for studying corticomuscular interactions as they carry significant time delays.

The most straightforward approach would be calculating the time lag from the phase information in the complex data of the WCS results with a simple fraction

$$\text{lag} = \frac{\phi_d}{2\pi f} \quad (9)$$

where ϕ_d is the phase difference between both signals at a specific time and frequency and f is the sample rate. However, volume conduction can cause the coherence and the phase-locking value to spuriously increase, and (9) is not effective to deal with this kind of common noise sources. To overcome this problem, a measure called the weighted phase lag index (WPLI) algorithm [33] that describes the consistency of the phase difference or time lag is used. This value will inform if the phase lag existent between both signals is consistent. This method not only highlights frequency bands where the phase difference is constant, indicating a strong linear relationship, but also penalises those synchronisations where time lag is close to zero, thus avoiding possible artefacts coming from common noise sources. The weight can be illustrated by Figure 1, which clearly shows the WPLI weights cross-spectra according to the magnitude of the imaginary component of the cross-spectrum. Cross-spectra around the real axis contribute to a less extent than

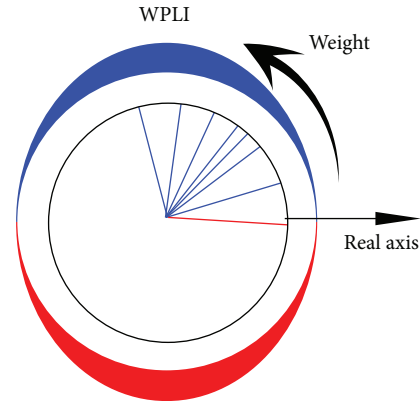


FIGURE 1: Illustration of the WPLI [22] (blue: phase lead; red: phase lag), where the oval outer layer reflects the weights, so values around real axes contribute less than values close to the imaginary axis.

cross-spectra around the imaginary axis. Their values are calculated as

$$\widehat{\Omega}^w = \frac{\sum_{j=1}^n \sum_{k \neq j} \text{Im}\{S_{xy_j}\} \cdot \text{Im}\{S_{xy_k}\}}{\sum_{j=1}^n \sum_{k \neq j} |\text{Im}\{S_{xy_j}\}| \cdot |\text{Im}\{S_{xy_k}\}|}, \quad (10)$$

where $\text{Im}\{\cdot\}$ is the imaginary part of the argument and S_{xy_j} is the cross-spectrum value of the j th trial of the total number of trials (n). The value is normalised from -1 to 1 . As indicated by Figure 1, a value of 1 suggests that the phase lag is 90° while a value of 0 corresponds to 0° or 180° . It should be noted that this process should be applied before the significance test.

The proposed methodology can be illustrated by Figure 2. Starting from the multiple trials' data collection or extraction, the WCS is applied on each trial to measure the correlation strength. After the number of trails is sufficient, the results of WCS of all trails are averaged. A significance test can then be applied to produce the binary correlation map. Meanwhile, the phase lag can be estimated based on the averaged WCS.

4. Results on Simulation Examples

The simulation example aims to evaluate the performance of the proposed analysis framework on frequential and time resolution and robustness against noise. Considering a linear single input single output (SISO) system, the input signal is defined as

$$x(t_i) = Z \left(\sum_{k=1}^K \cos(2\pi f_k t_i) \cdot \mathbb{W}_{[t_1, t_2]_k} \right) + \varepsilon_1. \quad (11)$$

The input signal constitutes an ensemble of K components, with different frequencies in the cosine form. It is defined within a temporal range $[t_1, t_2]$ through a window function $\mathbb{W}_{[t_1, t_2]_k}$. The entire ensemble was sampled by a normal distribution $Z \sim (0, 1)$. In other words, the amplitude of the entire signal is modulated by a random Gaussian signal.

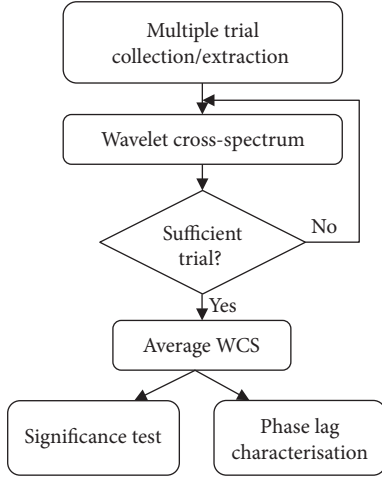


FIGURE 2: The flowchart of the proposed correlation analysis framework.

For the window function, a Tukey window was used with a taper parameter of 0.5. This type of window was selected to avoid possible ringing artefacts coming from the temporal sharp transitions of the frequency components. A white Gaussian noise ε_1 was also added, emulating a more realistic situation. The output signal is defined as

$$y(t_i) = Z \left(\sum_{k=1}^K a_k \cdot \cos(2\pi f_k t_i + \theta_k) \cdot \mathbb{W}_{[t_1, t_2]_k} \right) + \varepsilon_2. \quad (12)$$

One difference with the input is the change on the amplitude of each frequential component by setting a_k . In addition, each component presents a specific phase θ_k . Therefore, the linear system modulates the amplitude for each frequency of the input and delays it with a specific value. It must be noted that one can get several realisations of both measures, having then multiple trials of this linear interaction. Figure 3 illustrates the produced input and output signal of a single trial, which includes two frequential components: $f_1 = 10$ Hz within $[0.1, 0.5]$ and $f_2 = 30$ Hz within $[0.6, 0.9]$. The total data length is 1 sec with the sample rate of 1000 Hz. Both amplitude gains are equal and unit valued ($a_1 = a_2 = 1$), and delays θ_1 and θ_2 are set to 25 ms and 14 ms, respectively. Gaussian noise was added for both signals with the signal-to-noise ratio (SNR) of 40 dB. The bottom graph of Figure 3 shows the result of standard coherence based on Fourier transform. Although it successfully reveals the strong coherence at the frequency around 10 Hz and 30 Hz, it cannot localise when the coherence changes occurred. Such an approach therefore misses the time-resolved information, which is key to study a dynamical system. Although such a limitation can be partly addressed through using a sliding-window technique [34], the selection of window size is usually challenging and depends on the frequency of signals.

If there is no noise, the measured frequency-time interaction after the significance test using WCS can be represented by Figure 4. The yellow colours, indicating the significant

interactions, clearly correctly capture the two frequential components and corresponding starting and ending times, which cannot be revealed by the standard coherence. The white dashed line marks the cone of influence (COI). When computing CWT using convolution procedure, edge artefacts cannot be ignored. That is why COI is introduced to describe the area in which the power of the shifted wavelet drops to e^{-2} of the value at the edge [35].

If there is noise involved, the number of trials is important and should be considered. Figure 5 shows the result of WC with the associated significance test where $\text{SNR} = -5$ dB and $n = 5$. The linear synchronisation around frequencies of 10 Hz and 30 Hz is distinguishable. The temporal resolution of the interaction is close to the ideal one since the ending points of high coherent frequencies at 10 Hz and 30 Hz are located close to $[0.1 \text{ s}, 0.5 \text{ s}]$ and $[0.6 \text{ s}, 0.9 \text{ s}]$. However, high coherence values can be observed in the high-frequency band and very low-frequency band, which are determined as significant, which are artefacts. This is caused by the introduction of severe noise. Figure 6 shows the results using WCS for the same parameter settings. It shows a clearer plot with better contrast comparing to Figure 5. The simulated synchronisation can be easily differentiated from the rest of the noisy values based on the graph of significance test (see Figure 6(b)). This is explained by the normalisation process followed in the CWT process by Grinsted, where the energy of the wavelet signals is normalised (\mathbb{L}_2 normalisation). One direct consequence of \mathbb{L}_2 normalisation is that the values at higher frequencies are compressed more than those at lower frequencies.

To quantitatively study the influence of SNR and the number of trials on the results, the 2-D correlation coefficient between the significance tests of the ideal case (see Figure 4) and the testing case (see Figure 6(b)) is employed to measure the accuracy of connectivity detection. The equation to calculate the correlation coefficient of two images A and B can be written as

$$r = \frac{\sum_i \sum_j (A_{ij} - \bar{A})(B_{ij} - \bar{B})}{\sqrt{\left(\sum_i \sum_j (A_{ij} - \bar{A})^2\right) \left(\sum_i \sum_j (B_{ij} - \bar{B})^2\right)}}, \quad (13)$$

where \bar{A} and \bar{B} denote the means of A and B , respectively, and i and j denote the indexes of horizontal and vertical directions, respectively. A closer value of correlation coefficient to 1 indicates a better performance of detection. In this test, the SNR was varied from 30 dB to -10 dB with the step of 1 dB, and n was varied from 1 to 50 with the step of 1. The result is illustrated by a coloured matrix of correlation values, as shown in Figure 7. Drawing a horizontal line across the SNR axis, it can be observed that the correlation value increases with the number of trials. The increment rate is faster at higher levels of noise (lower value of SNR) than lower noise levels (higher value of SNR). A distinctive high noise range exists from 5 dB to -5 dB where limited trials (less than 6) can produce good results. For $\text{SNR} < -5$ dB and $\text{SNR} > 10$ dB, a significant number of trials are required to achieve reliable results. The fact of getting better results

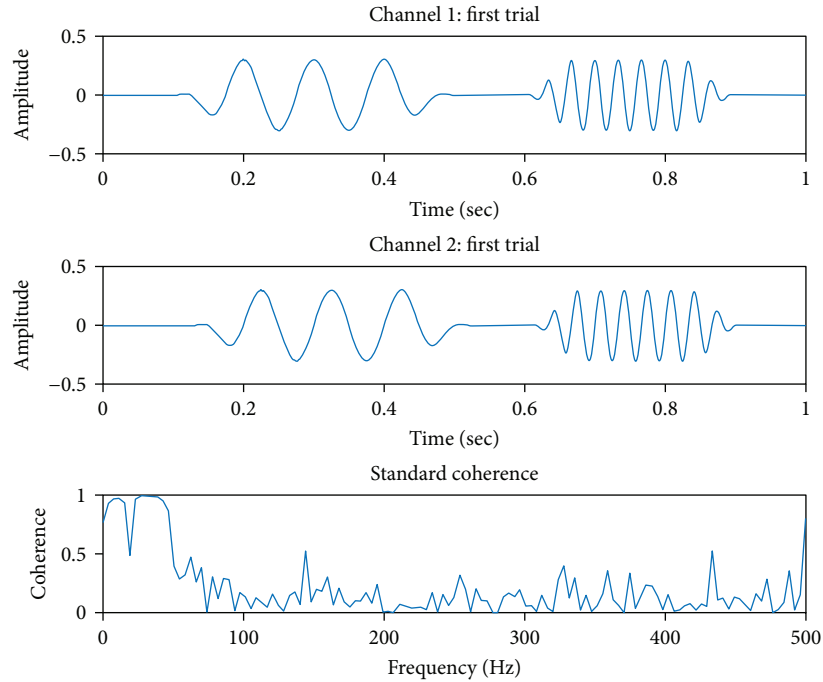


FIGURE 3: Example plots of the simulation signals (x = channel 1, y = channel 2) and their standard coherence.

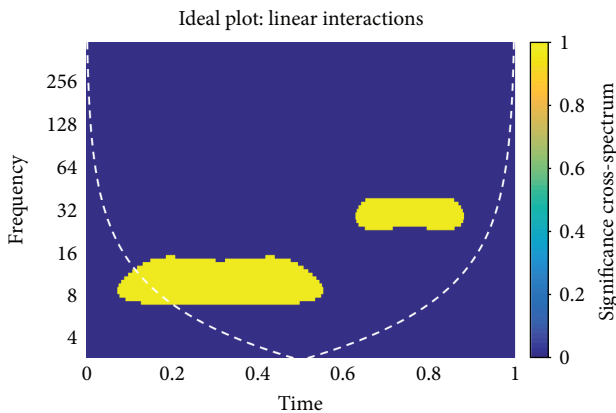


FIGURE 4: Measured interaction after significance test for the simulation example without noise using WCS.

with high noise levels (from 5 dB to -5 dB) with limited trials than those with low noise levels (>10 dB) can be explained by the influence of the Tukey window. When applied to short-time segments of low-frequency components, such a window function generates low-frequency artefacts. These artefacts can pass the statistical test when the threshold is low, which happens if the variance of both signals is low, or, in other words, when low noise is applied to the signal. This means, the noise level can influence the variance and thus the statistical threshold and finds a balance where the threshold only shows the sequential linear interactions without artefacts.

To complement the WCS results, Figure 8 shows the estimated WPLI results with the noise level of -5 dB and 5 trials. Although the first interaction at 10 Hz is still differentiable, the second interaction at 30 Hz is not so clear when

comparing with the rest of the noisy values. It should be noted that WPLI values are not aiming at locating strong linear interactions but indicating the consistency of time lag, which helps distinguish the true interaction and artefact. Combining Figure 8 with Figure 6, it can be observed that the synchrony at 10 Hz shows higher phase lag consistency than that at 30 Hz. Considering the time delay of the two components ($f_1 = 10$ Hz and $f_2 = 30$ Hz) were set to 25 ms and 14 ms, respectively, the phase difference is $\theta_1 = 90^\circ$ and $\theta_2 = 135^\circ$. According to Figure 1, the weight of θ_1 is higher than the weight of θ_2 ; hence, WPLI values around the interaction of f_1 have higher contrast than those of f_2 .

5. Results on Essential Tremor Data

5.1. Data Collection. All electrophysiological recordings were obtained with a multichannel Natus Quantum Amplifier (Optima Medical Ltd.). Four types of data were available for each recording: scalp electroencephalography (EEG), intracranial thalamic (VIM) local field potentials (LFPs), electromyography (EMG) with surface electrodes, and mono-axial accelerometer recordings from the hands and head. All data were sampled at 16.38 kHz and then downsampled to 2 kHz. This study focuses only on the interactions between thalamic LFPs and contralateral EMG (as each right and left half of the brain supplies the contralateral side of the body). LFPs refer to the summated electrical neuronal activity recorded with the DBS leads from the VIM thalamus. This activity was recorded by a quadripolar DBS lead with three possible input channels (0-1, 0-2, and 0-3) taking the pole 0 as a reference. Figure 9 shows an illustration of the lead layout. EMG data was recorded by surface EMG electrodes placed in different arm muscles. Given three LFP channels

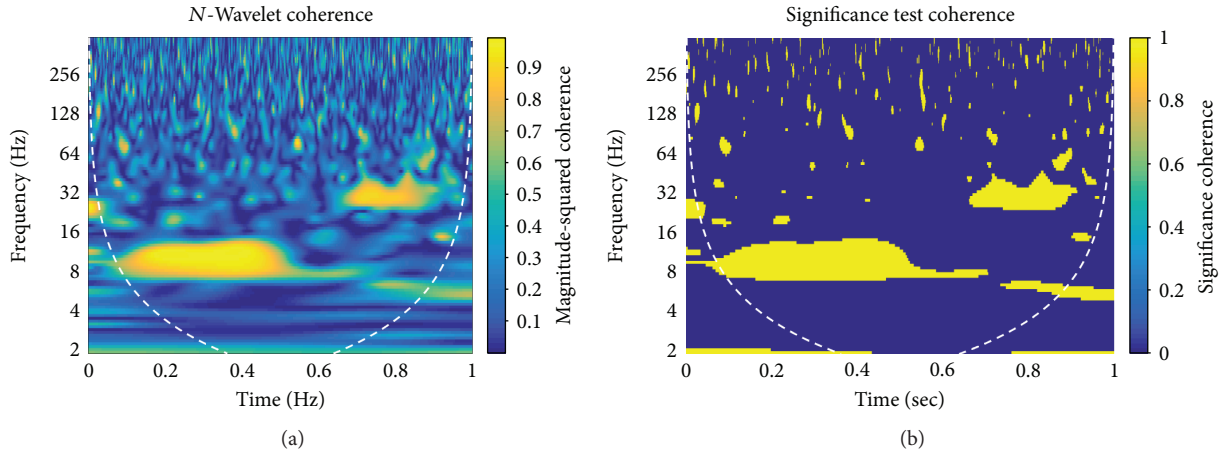


FIGURE 5: Results of wavelet coherence associated with significance test for the simulation example where $SNR = -5$ dB and $n = 5$.

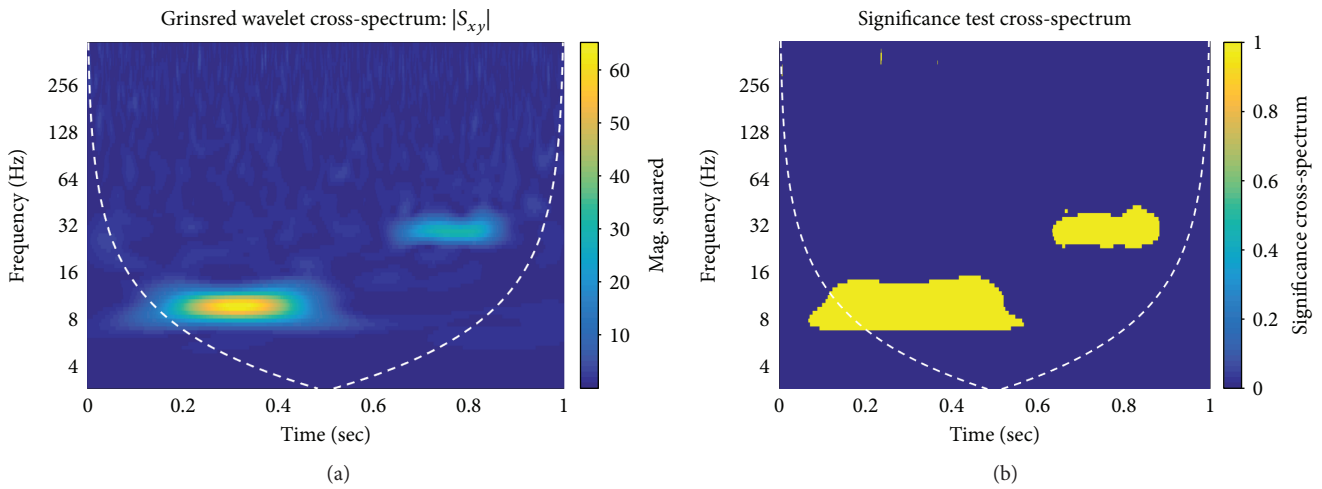


FIGURE 6: Results of WCS associated with significance test for the simulation example where $SNR = -5$ dB and $n = 5$.

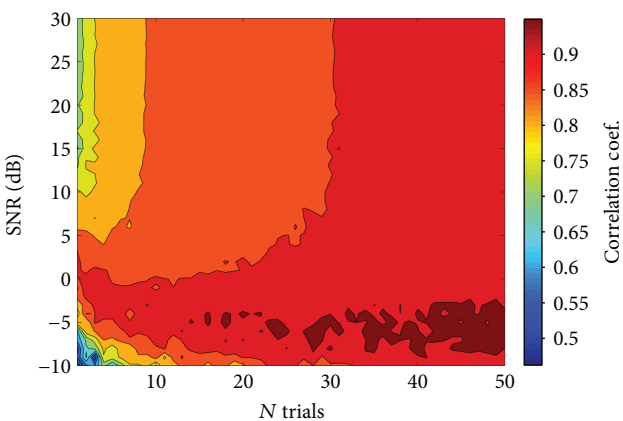


FIGURE 7: The accuracy of connectivity detection using WCS, represented by the 2-D correlation coefficient, for various levels of noise and number of trials.

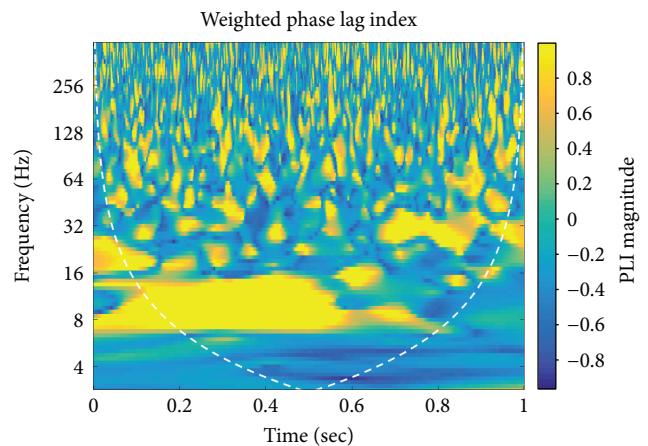


FIGURE 8: The estimated weighted phase lag index for the simulation example.

and five EMG channels, there are 15 possible pairs to be analysed in terms of interactions. However, based on previous observations from our clinical work, the right triceps brachii

muscle (commonly showing well-formed tremorogenic oscillations) and the left 0–3 LFPs were considered in this work. Therefore, this pair is primarily studied below.

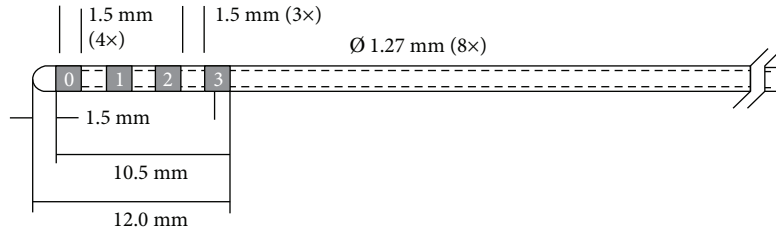


FIGURE 9: Design of quadripolar DBS lead based on Medtronic DBS model 3387.

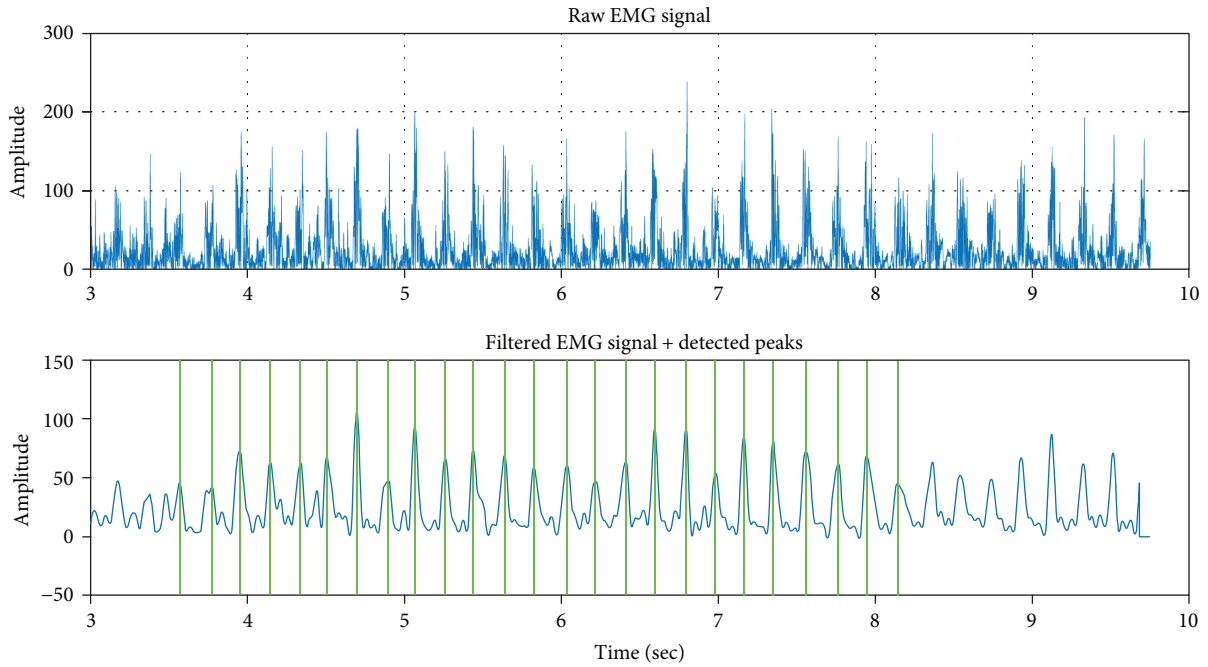


FIGURE 10: Illustration of multiple-trial extraction.

5.2. Multiple-Trial Data Extraction. The simulation example has demonstrated that the use of multiple trials or realisations of an event was important to better reveal significant interactions. However, it is not possible to repeat the same ET event in the same subject with the same conditions such as timing within each tremorogenic oscillation. To overcome this issue, the tremorogenic EMG signal trials were substituted by time segments coming from a long single trial signal. The necessary condition for extracting statistical properties by analysing data over time instead of evaluating several data samples is called ergodicity [36]. This is an important assumption that the target signal is considered as stationary instead of nonstationary and thus not assuming dynamical changes along the entire signal. However, it does not impede the detection of dynamic changes on frequential interactions. If the dynamic changes occur periodically, the true interactions will be enhanced by considering those time segments, while noise will be attenuated. Additionally, restricting time segments around a specific time interval, with the right number of trials and overlap, will make possible to see how local stationarity properties change over time, similar to a sliding-window technique, but the selection of widow size is not required.

For correcting this issue of the timing offset, a reference point, for each time segment extracted, is set as the closest peak of the EMG signal. Through this manner, phase cancellation artefacts can be avoided to some extent. To detect the peaks on EMG, the procedure follows three steps. The first step processes the data with a linear low-pass filter (passband edge frequency 15 Hz, stopband frequency 30 Hz, passband ripple 1 dB, and 60 dB of attenuation) since it is known that the tremor appears at low frequencies and the filtered signal is corrected with the corresponding delay of the filter. In the second step, the frequency component with highest magnitude is analysed. In the third step, a peak neighbourhood search is performed with a restriction based on the period of the fundamental frequency. Figure 10 illustrates an example of peak extraction from an epoch of EMG sample data coming from the triceps brachii, where the top figure shows a time series of raw EMG data and the bottom figure shows the filtered data with the detected peaks marked by green lines.

5.3. Interaction Estimation Based on a Single Trial. Figure 11 shows the result of WCS of a 10 sec single trial between left L0L3(LFP) and right triceps (EMG). As shown in the top graph, there is a distinguishable linear interaction between

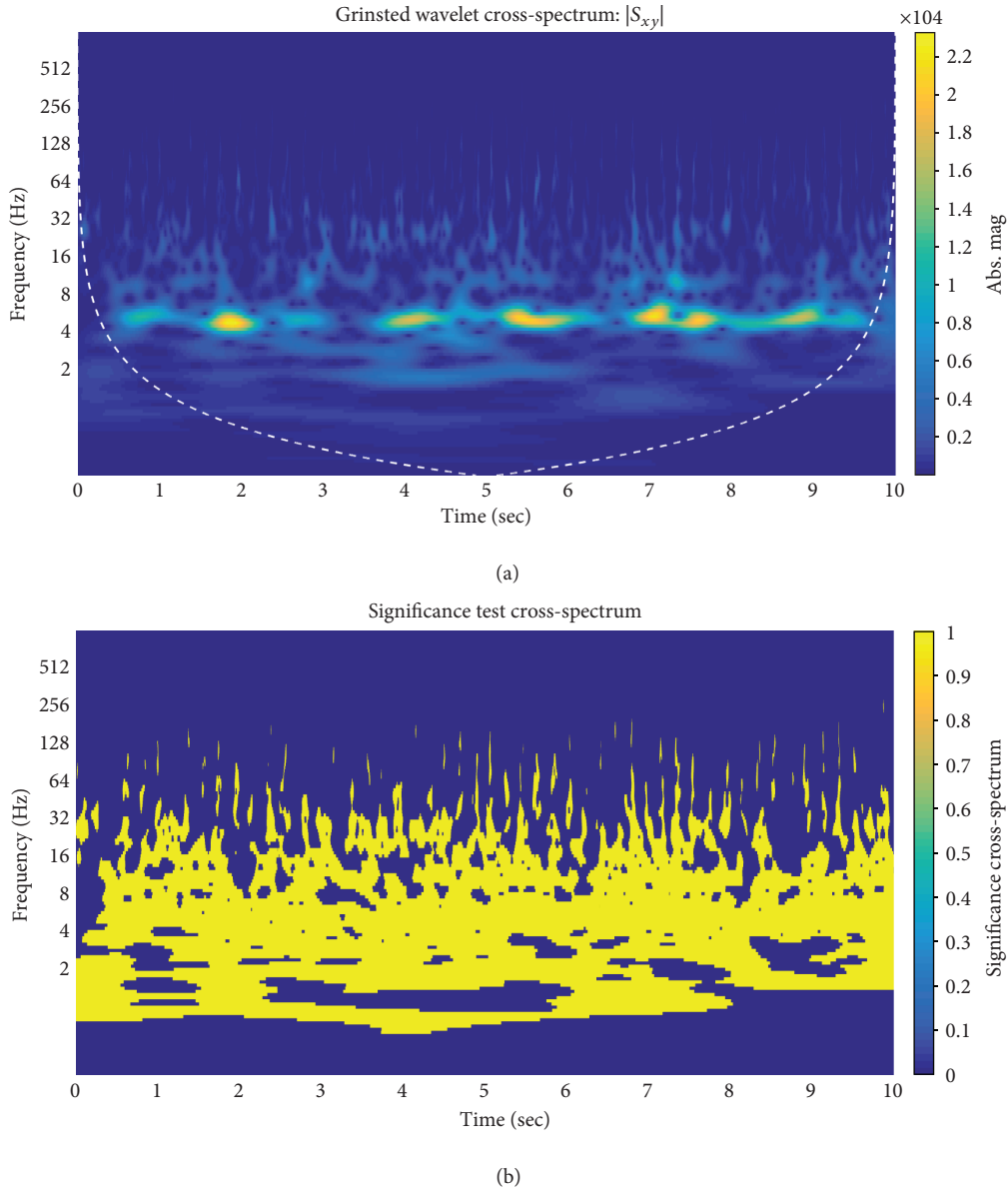


FIGURE 11: Result of wavelet cross-spectrum of a 10 sec single trial between LOL3 LFPs and right triceps brachii EMG.

LFP and EMG around 5 Hz, which at the same time is the frequency of the arm tremor (validated by the accelerometer data). Moreover, the intensity of 5 Hz interactions is intermittent, showing peaks and troughs over time. In addition, weaker synchronisation is present at lower and higher frequencies. The significance test of a single trial is shown in the bottom graph of Figure 11, where significant interactions are observed from 1 to 128 Hz when using a single trial that as a result reduces the confidence level of estimation. Multiple trials are required to improve the confidence level to reveal the true significant interactions by reducing the influence of noise.

The colour scale establishes a range of values, in terms of WCS module, of fourth order of magnitude. However, it is not a reliable feature to compare with other combinations of signals, since the scale depends on the amplitude of the

original signals that can differ depending on the impedance and position of the reference electrode. Instead, comparing different plots during a long period of time and checking which one is more consistent and regular will lead to better interpretation of the underlying interactions. Figure 12 shows the WCS results of a 15 sec single trial of five combinations between LFPs and EMG recordings. In this figure, the triceps brachii (a) presents a more stable and periodical behaviour in terms of the linear spectral correlation with LOL3. Figures 12(b), 12(c), and 12(e) show high spread values over lower frequencies.

5.4. Interaction Estimation Based on Multitrial. Two parameters to be determined for multitrial analysis for real data include the number of trials and the overlap rate. With sampling starting from the 6th sec of the data of LOL3 and right

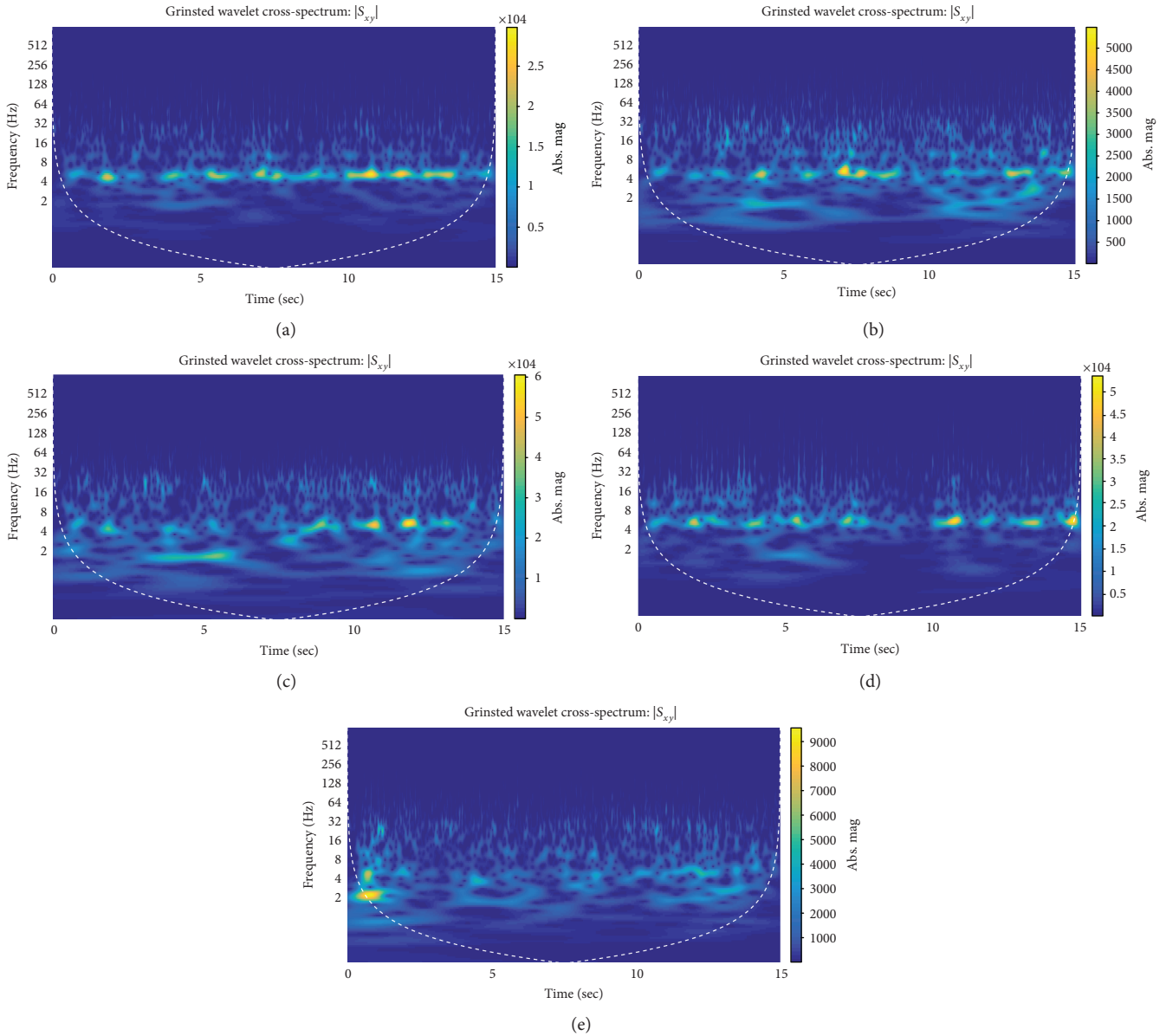


FIGURE 12: Result of wavelet cross-spectrum of a 15 sec single trial between (a) left L0L3 LFPs and the right triceps brachii EMG, (b) L0L3-right biceps brachii, (c) L0L3-right extensor digitorum communis, (d) L0L3-right flexor carpi ulnaris, and (e) L0L3-right abductor pollicis brevis.

triceps brachii with a window length of 1 sec epoch, the correlation was estimated where the trial number was set as 10 and 20, and the overlap rate was set as 0%, 50%, and 75%. For the trial number of 10 and the overlap rate of 0%, the sampling windows are [6 s, 7 s], [7 s, 8 s], ..., [15 s, 16 s]. It should be noted that the overlap rates of 50% and 75% are approximate values. The true overlap rates are determined by the references points based on the closest peak of the EMG signal. For example, the second window of the overlap rate of 50% is not necessary to start exactly from 6.5 s. It starts from the closest EMG peak around 6.5 s. Figures 13–14 show the results of WCS with the trial number of 10 and 20 and overlap rates of 0%, 50%, and 75%. In comparison with the result of a single trial shown in Figure 15, results of the

multitrial highlight those interactions that keep repeating over time and reduce the occasional high values that could be artefactual. For example, the 5 Hz tremor along with its first harmonic at 10 Hz shows a stable linear correlation. Despite losing time resolution due to averaging, dynamic changes in WCS values at higher frequencies are still observable and could be genuine. A more regular temporal pattern can be observed for the frequency band from 16 Hz to 64 Hz following the increment of the overlap rate. The increased number of trials makes the results smoother and more consistent.

To evaluate the time lag of the significant interactions, the WPLI approach was applied and the result is shown in Figure 16. The higher contrast shows that components

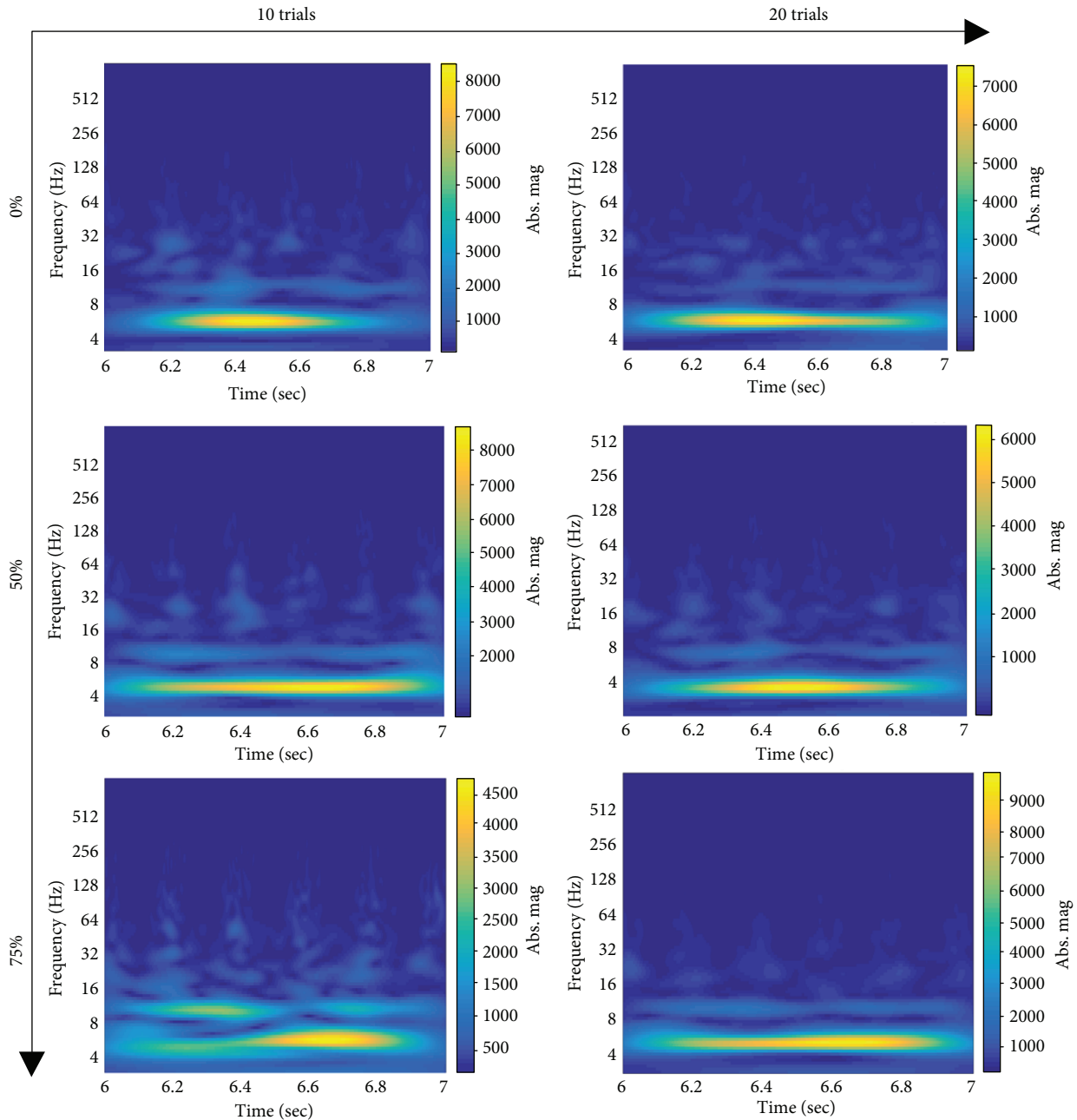


FIGURE 13: Result of wavelet cross-spectrum for left L0L3 versus right triceps brachii based on multitrials with different parameter settings (number of trials and degree of overlap).

around the first harmonic of the tremor have the more prominent phase lag.

6. Conclusions

This paper proposes a novel data analysis framework to study thalamomuscular associations in essential tremor involving three steps: correlation strength estimation, significance test, and phase lag characterisation. This framework aims to improve the robustness and reliability of correlation analysis between the local field potential recordings from the brain and the tremulous electrical activity recorded on EMG. It

has been shown in the simulation example that the proposed approach can effectively evaluate the linear interaction between two signals. The sensitivity analysis studies show how the number of trials and noise level of measurement affect the results. For data with noise level < -5 dB or > 10 dB, a significant number of trials produce much better results. However, for data with noise level > -5 dB and < 5 dB, the number of trials has less influence on the findings. The application of the method, on real data from two patients with ET undergoing DBS surgery for tremor suppression, demonstrates the validity of the proposed approach through segmenting a long single epoch into a number of overlapped

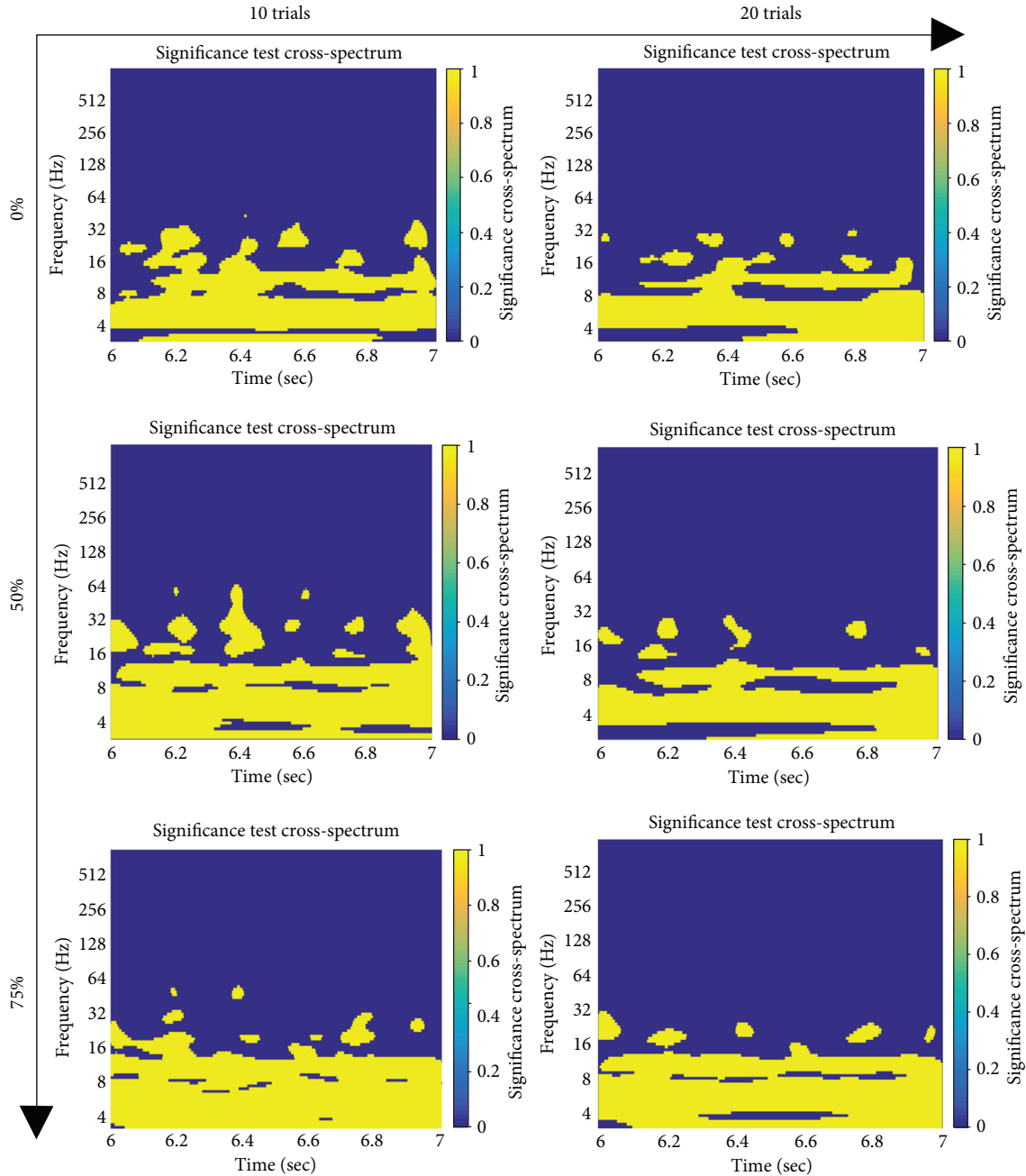


FIGURE 14: Significance test result of wavelet cross-spectrum for left L0L3 versus right triceps brachii based on multitrial analysis with different parameter settings (number of trials and degree of overlap).

windows to produce the averaged strength of associations. One limitation of this approach is that the result is difficult to be quantified due to the complexity of WCS patterns if the ground truth is unknown. Another potential limitation is that the number of trials plays an important role in improving the performance of this approach. With a single trial, the significance test cannot be constructed. In the real data application, it is not possible to repeat the same ET event (i.e., tremorogenic oscillation) in the same subject with the same conditions. Future work therefore will focus on quantification of the results and reduce the dependency from the number of trials.

It should be noted that wavelet cross-spectrum and phase lag characterisation used in this framework are not novel. However, combining them together along with a significance test is new. Furthermore, this is the first attempt to apply wavelet-based correlation analysis on patients with medically refractory essential tremor undergoing surgery. This paper shows a clear association between the thalamic local field potential recordings and the contralateral tremorogenic EMG oscillations, at the frequency of the tremor and its first harmonic (Figure 13). These interactions are beyond the observational empirical interpretation of thalamic LFPs and EMG recordings from patients with ET. This paper offers a

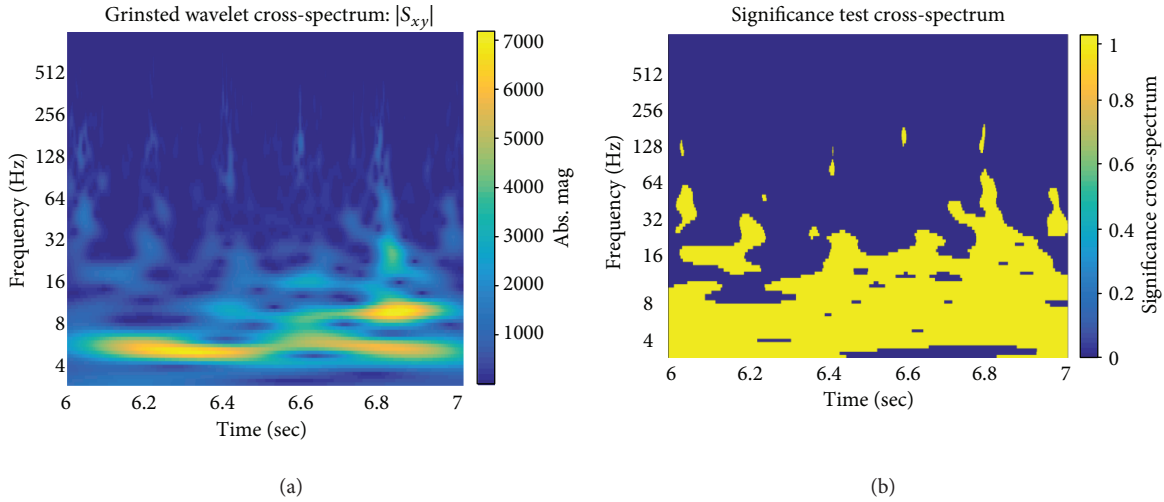


FIGURE 15: Result of wavelet cross-spectrum for L0L3-right triceps brachii based on a single trial over a 1-second epoch.

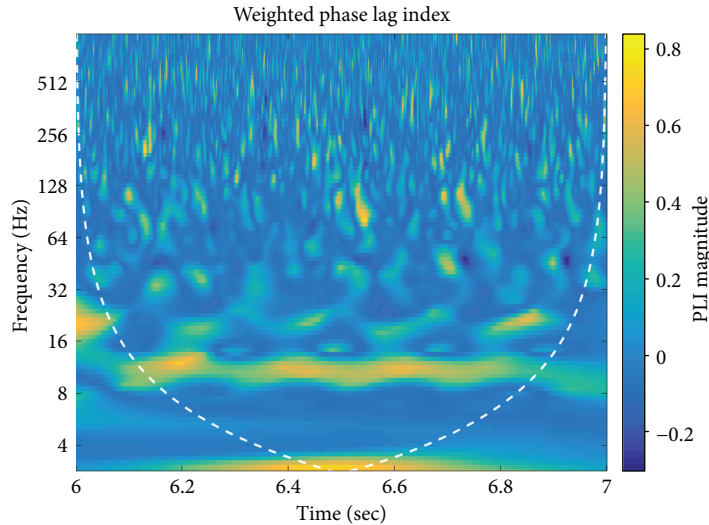


FIGURE 16: Result of WPLI for L0L3 versus right-triceps brachii based on 30 trials and 80% overlap.

framework that can be used to choose the thalamic contacts that show the strongest association with the tremulous EMG oscillations that if selected for high-frequency DBS stimulation produce a better clinical outcome in comparison to the empirical programming of the DBS device. Our clinical experience so far confirms this hypothesis, but this will be explored in a future study, on a significant number of patients with ET, where the emphasis will be on the use of such a framework to obtain best tremor suppression by objective selection of the ideal contacts to stimulate. As more complex multicontact directional DBS leads are already used in various centres, evidence-based (both radiological and neurophysiological) selection of the ideal contacts to stimulate will become increasingly important [7]. With this framework, the electrophysiological LFP recordings and their relationship to the tremor can be analysed to determine the DBS lead contacts that show the strongest association with

the tremor and select them for stimulation. This work offers the proof of principle required to assess the utility and the limitations of this methodology. It has been demonstrated that the proposed framework can reveal significant cerebro-muscular interactions, in this instance thalamic (VIM) LFPs versus the tremulous EMG activity, reaffirming *in vivo* that this part of the thalamus is part of the central tremorogenic network in ET. It could play an important role for future research on developing a closed-loop DBS device. It also has the potential to objectively determine in individual patients which of the thalamic lead contacts shows objectively the strongest association with the tremor, particularly as multicontact leads make their way into clinical practice. This thalamic lead contact could plausibly offer the best tremor suppression for each patient. This hypothesis will have to be confirmed in future electroclinical studies as our clinical experience so far is pointing in this direction.

Data Availability

The data used to support the findings of this study are available from the corresponding author upon request.

Conflicts of Interest

The authors declare that they have no conflicts of interest.

Acknowledgments

This work was supported in part by the Through-Life Engineering Services Centre at Cranfield University (UK), in part by Royal Hallamshire Hospital at Sheffield (UK), in part by Zhejiang University of Technology (China), and in part by the Computational and Software Techniques in Engineering MSc Course at Cranfield University (UK). The authors thank Neurocare for the purchase of the medical equipment used for the polygraphy recordings on their patients. This research was carried out in part at the National Institute for Health Research (NIHR) Sheffield Biomedical Research Centre (Translational Neuroscience)/NIHR Sheffield Clinical Research Facility. This work was also supported by the National Science Foundation Program of China (61601029), a grant of the Ningbo 3315 Innovation Team, and the China Association for Science and Technology (2016QNRC001).

References

- [1] E. Critchley, "Clinical manifestations of essential tremor," *Journal of Neurology, Neurosurgery, and Psychiatry*, vol. 35, no. 3, pp. 365–372, 1972.
- [2] J. Raethjen and G. Deuschl, "The oscillating central network of essential tremor," *Clinical Neurophysiology*, vol. 123, no. 1, pp. 61–64, 2012.
- [3] E. D. Louis, "Essential tremor," *Lancet Neurology*, vol. 4, no. 2, pp. 100–110, 2005.
- [4] P. Pal, "Guidelines for management of essential tremor," *Annals of Indian Academy of Neurology*, vol. 14, no. 5, p. 25, 2011.
- [5] M. L. Kringsbach, N. Jenkinson, S. L. F. Owen, and T. Z. Aziz, "Translational principles of deep brain stimulation," *Nature Reviews Neuroscience*, vol. 8, no. 8, pp. 623–635, 2007.
- [6] R. E. Gross, P. Krack, M. C. Rodriguez-Oroz, A. R. Rezaei, and A.-L. Benabid, "Electrophysiological mapping for the implantation of deep brain stimulators for Parkinson's disease and tremor," *Movement Disorders*, vol. 21, no. S14, pp. S259–S283, 2006.
- [7] W. M. M. Schüpbach, S. Chabardes, C. Matthies et al., "Directional leads for deep brain stimulation: opportunities and challenges," *Movement Disorders*, vol. 32, no. 10, pp. 1371–1375, 2017.
- [8] S. F. Lempka and C. C. McIntyre, "Theoretical analysis of the local field potential in deep brain stimulation applications," *PLoS One*, vol. 8, no. 3, article e59839, 2013.
- [9] J. Raethjen, R. B. Govindan, F. Kopper, M. Muthuraman, and G. Deuschl, "Cortical involvement in the generation of essential tremor," *Journal of Neurophysiology*, vol. 97, no. 5, pp. 3219–3228, 2007.
- [10] D. Halliday, B. Conway, S. Farmer, U. Shahani, A. Russell, and J. Rosenberg, "Coherence between low-frequency activation of the motor cortex and tremor in patients with essential tremor," *The Lancet*, vol. 355, no. 9210, pp. 1149–1153, 2000.
- [11] S. Chakraborty, J. Kopecká, O. Šprdlík et al., "Intermittent bilateral coherence in physiological and essential hand tremor," *Clinical Neurophysiology*, vol. 128, no. 4, pp. 622–634, 2017.
- [12] R. Zakaria, F. A. Lenz, S. Hua, B. H. Avin, C. C. Liu, and Z. Mari, "Thalamic physiology of intentional essential tremor is more like cerebellar tremor than postural essential tremor," *Brain Research*, vol. 1529, pp. 188–199, 2013.
- [13] J. F. Geweke, "Measures of conditional linear dependence and feedback between time series," *Journal of the American Statistical Association*, vol. 79, no. 388, pp. 907–915, 1984.
- [14] Y. Zhao, S. A. Billings, H. Wei, F. He, and P. G. Sarrigiannis, "A new NARX-based granger linear and nonlinear causal influence detection method with applications to EEG data," *Journal of Neuroscience Methods*, vol. 212, no. 1, pp. 79–86, 2013.
- [15] S.-H. Jin, P. Lin, and M. Hallett, "Linear and nonlinear information flow based on time-delayed mutual information method and its application to corticomuscular interaction," *Clinical Neurophysiology*, vol. 121, no. 3, pp. 392–401, 2010.
- [16] T. Kreuz, "Measures of neuronal signal synchrony," *Scholarpedia*, vol. 6, no. 12, article 11922, 2011.
- [17] P. Xie, F. M. Yang, Y. B. Wang, L. L. Wang, and C. H. Yang, "Research on corticomuscular coherence based on transfer entropy with parameters optimization," *Brain Stimulation*, vol. 10, no. 2, p. 439, 2017.
- [18] D. J. Pedrosa, C. Nelles, P. Brown et al., "The differentiated networks related to essential tremor onset and its amplitude modulation after alcohol intake," *Experimental Neurology*, vol. 297, pp. 50–61, 2017.
- [19] V. K. Jirsa and A. McIntosh, *Handbook of Brain Connectivity*, Springer Berlin Heidelberg, Berlin, Heidelberg, 2007.
- [20] N. Ramnani, L. Lee, A. Mechelli, C. Phillips, A. Roebroeck, and E. Formisano, "Exploring brain connectivity: a new frontier in systems neuroscience," *Trends in Neurosciences*, vol. 25, no. 10, pp. 496–497, 2002.
- [21] P. Venkatakrisnan, R. Sukanesh, and S. Sangeetha, "Detection of quadratic phase coupling from human EEG signals using higher order statistics and spectra," *Signal, Image and Video Processing*, vol. 5, no. 2, pp. 217–229, 2011.
- [22] S. Marceglia, A. M. Bianchi, S. Cerutti, and D. Servello, "Cross-bispectral analysis of local field potentials: an application to essential tremor," in *2009 4th International IEEE/EMBS Conference on Neural Engineering*, pp. 494–497, Antalya, Turkey, 2009.
- [23] D.-H. Jeong, Y.-D. Kim, I.-U. Song, Y.-A. Chung, and J. Jeong, "Wavelet energy and wavelet coherence as EEG biomarkers for the diagnosis of Parkinson's disease-related dementia and Alzheimer's disease," *Entropy*, vol. 18, no. 1, p. 8, 2016.
- [24] C. Ieracitano, J. Duun-Henriksen, N. Mammone, F. La Foresta, and F. C. Morabito, "Wavelet coherence-based clustering of EEG signals to estimate the brain connectivity in absence epileptic patients," in *2017 International Joint Conference on Neural Networks (IJCNN)*, pp. 1297–1304, Anchorage, AK, USA, May 2017.
- [25] A. Bernas, A. P. Aldenkamp, and S. Zinger, "Wavelet coherence-based classifier: a resting-state functional MRI study on neurodynamics in adolescents with high-functioning autism," *Computer Methods and Programs in Biomedicine*, vol. 154, pp. 143–151, 2018.

- [26] X. Liu, J. Donnelly, M. Czosnyka et al., "Cerebrovascular pressure reactivity monitoring using wavelet analysis in traumatic brain injury patients: a retrospective study," *PLoS Medicine*, vol. 14, no. 7, article e1002348, 2017.
- [27] M. Yaesoubi, R. L. Miller, J. Bustillo, K. O. Lim, J. Vaidya, and V. D. Calhoun, "A joint time-frequency analysis of resting-state functional connectivity reveals novel patterns of connectivity shared between or unique to schizophrenia patients and healthy controls," *NeuroImage: Clinical*, vol. 15, pp. 761–768, 2017.
- [28] L. Bu, D. Wang, C. Huo, G. Xu, Z. Li, and J. Li, "Effects of poor sleep quality on brain functional connectivity revealed by wavelet-based coherence analysis using NIRS methods in elderly subjects," *Neuroscience Letters*, vol. 668, pp. 108–114, 2018.
- [29] V. B. Perez, B. J. Roach, S. W. Woods et al., "Early auditory gamma-band responses in patients at clinical high risk for schizophrenia," *Supplements to Clinical Neurophysiology*, vol. 62, pp. 147–162, 2013.
- [30] R. C. Helmich, I. Toni, G. Deuschl, and B. R. Bloem, "The pathophysiology of essential tremor and Parkinson's tremor," *Current Neurology and Neuroscience Reports*, vol. 13, no. 9, p. 378, 2013.
- [31] J. A. Gallego, J. L. Dideriksen, A. Holobar et al., "Influence of common synaptic input to motor neurons on the neural drive to muscle in essential tremor," *Journal of Neurophysiology*, vol. 113, no. 1, pp. 182–191, 2015.
- [32] J. Bigot, M. Longcamp, F. Dal Maso, and D. Amarantini, "A new statistical test based on the wavelet cross-spectrum to detect time-frequency dependence between non-stationary signals: application to the analysis of cortico-muscular interactions," *NeuroImage*, vol. 55, no. 4, pp. 1504–1518, 2011.
- [33] M. Vinck, R. Oostenveld, M. van Wingerden, F. Battaglia, and C. M. A. Pennartz, "An improved index of phase-synchronization for electrophysiological data in the presence of volume-conduction, noise and sample-size bias," *NeuroImage*, vol. 55, no. 4, pp. 1548–1565, 2011.
- [34] K. F. K. Wong, E. A. Mukamel, A. F. Salazar et al., "Robust time-varying multivariate coherence estimation: application to electroencephalogram recordings during general anesthesia," in *2011 Annual International Conference of the IEEE Engineering in Medicine and Biology Society*, pp. 4725–4728, Boston, MA, USA, 2011.
- [35] A. Grinsted, J. C. Moore, and S. Jevrejeva, "Application of the cross wavelet transform and wavelet coherence to geophysical time series," *Nonlinear Processes in Geophysics*, vol. 11, no. 5/6, pp. 561–566, 2004.
- [36] A. Cohen, *Biomedical Signal Processing: Time and Frequency Domains Analysis*, CRC Press, 1986.

Research Article

Automatic Lateralization of Temporal Lobe Epilepsy Based on MEG Network Features Using Support Vector Machines

Ting Wu,^{1,2} Duo Chen,³ Qiqi Chen,² Rui Zhang,² Wenyu Zhang,⁴ Yuejun Li,¹ Ling Zhang,⁵ Hongyi Liu,² Suren Wan,³ Tianzi Jiang,¹ and Junpeng Zhang ⁴

¹Key Laboratory for Neuroinformation of the Ministry of Education, School of Life Science and Technology, University of Electronic Science and Technology of China, Chengdu, China

²Department of Magnetoencephalography, Nanjing Brain Hospital Affiliated to Nanjing Medical University, Nanjing, China

³State Key Laboratory of Bioelectronics, School of Biological Science and Medical Engineering, Southeast University, Nanjing, China

⁴Department of Medical Information and Engineering, College of Electrical Engineering and Information Technology, Sichuan University, Chengdu, China

⁵School of Biomedical Engineering, Hubei University of Science and Technology, Xianning, China

Correspondence should be addressed to Junpeng Zhang; junpeng.zhang@gmail.com

Received 17 August 2017; Revised 27 November 2017; Accepted 18 January 2018; Published 18 February 2018

Academic Editor: Hamed Azami

Copyright © 2018 Ting Wu et al. This is an open access article distributed under the Creative Commons Attribution License, which permits unrestricted use, distribution, and reproduction in any medium, provided the original work is properly cited.

Correct lateralization of temporal lobe epilepsy (TLE) is critical for improving surgical outcomes. As a relatively new noninvasive clinical recording system, magnetoencephalography (MEG) has rarely been applied for determining lateralization of unilateral TLE. Here we propose a framework for using resting-state brain-network features and support vector machine (SVM) for TLE lateralization based on MEG. We recruited 15 patients with left TLE, 15 patients with right TLE, and 15 age- and sex-matched healthy controls. The lateralization problem was then transferred into a series of binary classification problems, including left TLE versus healthy control, right TLE versus healthy control, and left TLE versus right TLE. Brain-network features were extracted for each participant using three network metrics (nodal degree, betweenness centrality, and nodal efficiency). A radial basis function kernel SVM (RBF-SVM) was employed as the classifier. The leave-one-subject-out cross-validation strategy was used to test the ability of this approach to overcome individual differences. The results revealed that the nodal degree performed best for left TLE versus healthy control and right TLE versus healthy control, with accuracy of 80.76% and 75.00%, respectively. Betweenness centrality performed best for left TLE versus right TLE with an accuracy of 88.10%. The proposed approach demonstrated that MEG is a good candidate for solving the lateralization problem in unilateral TLE using various brain-network features.

1. Introduction

Temporal lobe epilepsy (TLE) is the most common type of drug-resistant focal epilepsy in adults [1]. TLE is traditionally associated with mesial temporal sclerosis (MTS), cell loss, and gliosis in the hippocampus, entorhinal cortex, and amygdala [2]. Currently, surgical intervention is the main choice of treatment for medically intractable TLE [3]. However, surgery helps only 70% of patients become seizure free [4]. Indeed, approximately one-third of TLE patients are unable to control their seizures, even with the best available medications and surgery. Correct clinical diagnosis for TLE is critical for improving surgical outcomes and requires highly

trained professionals [5]. Manual diagnosis of unilateral TLE using brain-neuroimaging methods is time-consuming, and different experts may give contradictory diagnoses for the same data [6]. Therefore, an objective and automated tool that can accurately classify brain images is desirable for presurgical evaluation of epileptogenic lateralization in TLE.

The support vector machine (SVM) method is a supervised machine learning technique for classification, and the radial basis function (RBF) kernel is the most commonly used kernel function for SVM [7]. As a classification tool, the SVM technique is flexible, automated, and sufficiently fast to operate in a clinical setting [8]. SVM algorithms have been applied for measuring brain morphology [9], including

cortical thickness, volume, curvature, and identification of MTS in TLE patients. SVM approaches have been utilized to determine lateralization of the TLE epileptogenic focus with diffusion tensor imaging (DTI) structural connectomes [10]. Another study verified the use of SVM for voxel-based MRI classification, and TLE with MTS can be distinguished from TLE without MTS with over 88% accuracy [8]. These investigations have combined SVM with MRI or DTI. However, one of the newest neuroimaging tools, magnetoencephalography (MEG), has rarely been applied for solving the classification problem of unilateral TLE.

During the last decade, MEG has become increasingly available as a noninvasive, reliable, fast, and patient-friendly technique for recording brain activity [11–14]. MEG has been widely applied for studying epilepsy disorders, particularly the localization of pathological brain activity or lesions in candidates for epilepsy surgery [15–17]. In addition, the sensitivity of MEG has been investigated for spike detection that depends on two sensor types (magnetometer and gradiometer) in patients with epileptic foci in the mesial temporal lobe [18]. The results revealed that the magnetometer was more sensitive in the mesial temporal area, whereas the gradiometer performed better in the lateral temporal area. In another study, the ability of MEG to determine the localization and orientation of medial temporal spikes was evaluated in patients with known medial TLE using magnetic source imaging (MSI) with equivalent current dipoles (ECD) [19]. The results revealed that MSI with ECD was able to detect medial temporal spikes, providing important localizing information in patients with medial TLE. In our previous MEG study, we investigated the relationship between endogenous neuromagnetic signals in patients with epilepsy and epileptic foci determined by clinical data, analyzing the performance of several existing methods for localizing the epileptic focus, such as ECD, imaginary coherence (IC), and synthetic aperture magnetometry (SAM) [20]. The results suggested that the IC method performs better than ECD or SAM for quantitatively identifying epileptic activity. Thus, in the current study, we calculated connectivity matrices to construct a brain-network for all participants, based on the IC method.

Brain regions and the structural or functional associations between them constitute a brain-network. Complex network analysis is useful for quantitatively characterizing the properties of brain-networks with a small number of network measures [21, 22]. Recent studies have established that TLE affects a distributed neural network, with widespread extratemporal effects, rather than having a single focal epileptogenic source [23–26]. Based on both structural and functional connectivity (FC) analyses, accumulating evidence suggests that brain-networks in TLE patients are pathologically altered [27–30]. Hsiao et al. [31] investigated FC alterations in the default mode network (DMN) in TLE, using resting-state spike-free MEG recordings. Their results revealed that TLE involved changes in FC within the DMN and that the change was associated with the lateralization of TLE. In right TLE, FC between the DMN and the right medial temporal region is enhanced, while left TLE involves enhanced FC between the DMN and bilateral medial

temporal regions [31]. By analyzing resting-state MEG signals, Jin et al. [32] calculated betweenness centrality at the source-level functional network in mesial TLE. The results indicated that altered electrophysiological functional hubs reflected pathophysiological brain-network reorganization [32]. To test the hypothesis that FC and network characteristics are useful for determining the lateralization of TLE, Yang et al. extracted resting-state functional brain-network features as inputs to an SVM [33]. Using a leave-one-out cross-validation strategy, their SVM model achieved a prediction accuracy of 83% with 12 TLE patients. However, there are few studies using MEG data to construct functional brain-networks for investigating the lateralization of unilateral TLE.

In the current study, we extracted brain-network features of patients and healthy controls based on a resting-state MEG scan, including nodal degree, betweenness centrality, and nodal efficiency. The features were used as input to the SVM to classify left TLE, right TLE, and healthy controls. The results indicated that nodal degree exhibited the best performance for left TLE versus healthy control and right TLE versus healthy control, while betweenness centrality performed best for left TLE versus right TLE. Thus, our findings indicated that MEG is helpful for solving the lateralization problem of unilateral TLE.

2. Materials and Methods

2.1. Patients and Healthy Control Participants. Thirty patients with unilateral TLE (age range: 15–62 years, mean age: 38 years; 15 left TLE and 15 right TLE) were recruited at the Nanjing Brain Hospital, Nanjing Medical University. Seizure-type classification was based on the International League Against Epilepsy (ILAE) criteria [34] and the laterality of the seizure origin was determined using clinical history, a comprehensive neurological examination, interictal EEG recordings, and neuroimaging. Fifteen healthy volunteers (age range: 19–45 years, mean age: 27.9 years) were recruited as controls who had no history of symptoms related to neurological or psychiatric disorders. There were no significant differences in age or sex between the groups.

2.2. Ethics Statement. A full explanation of this study was provided to all patients and control participants before enrollment. All participants provided voluntary and informed written consent according to the standards set by the ethical committee of Nanjing Brain Hospital of Nanjing Medical University, who approved the study.

2.3. MEG Recordings. MEG recordings were performed while participants were seated inside a magnetically shielded room using a whole-head CTF 275-Channel MEG system (VSM MedTech Systems Inc., Coquitlam, BC, Canada). Before beginning data acquisition, three small coils were attached to the nasion, left, and right preauricular points on the head of each participant. The three coils were subsequently activated at different frequencies for measuring each individual's head position relative to the MEG sensors. The system allowed for head localization to an accuracy of 1 mm. The sampling rate of MEG recordings was 1200 Hz.

All MEG data were recorded with noise cancellation of third-order gradients. Each epoch took 120 seconds and 15 epochs were recorded from each participant. The head position was measured before and after each epoch. The limit for acceptable head movement during MEG recording was 5 mm. Spontaneous resting-state activity was recorded while participants remained in a supine position with their eyes closed. The resting-state in this study was defined as spontaneous activity not evoked by cognitive tasks and in the absence of seizure activity.

2.4. MRI Acquisition. MRI acquisition was similar to that in our previous study [20]. MR images were acquired on a 3 T scanner (Siemens Medical Solutions, Erlangen, Germany). The protocol typically included the following sequences: (1) A T1-weighted, 3D spoiled gradient-recalled echo in a steady-state sequence with TR = 7.5 ms, TE = min full, flip angle = 15°, and field of view = 240 mm × 240 mm; (2) A T2-weighted image, 2D fluid-attenuated inversion recovery (FLAIR) with TR = 8000 ms, TE = 120 ms, TI = 2000 ms, matrix = 192 × 256, field of view = 240 mm × 240 mm, and slice thickness = 5 mm in the coronal and axial planes, respectively. To allow for accurate coregistration of the two data sets, the three fiducial points were placed in locations identical to those of the three coils used in the MEG recordings.

2.5. MEG Preprocessing. All MEG recordings were visually examined off-line by two experienced epileptologists, and the peaks of all epileptic spikes were marked manually based on the MEG recordings. We extracted three quasi-stationary segments (20 s per segment) from each participant. The segments were at least 10 s away from recent epileptic discharge and free from eye- or muscle-related artifacts or epileptic activities. Then, the data were band-pass filtered in the 1 to 4 Hz range as a frequency band of interest for further analysis. Preprocessing and analysis of MEG data were performed with Brainstorm [35], a well-documented software package that is freely available to download online under the GNU general public license (<http://neuroimage.usc.edu/brainstorm>).

2.6. Network Construction. The Freesurfer open-source software package was used to extract the cortical envelope (<http://surfer.nmr.mgh.harvard.edu/fswiki/DownloadAndInstall>) of each subject based on their individual MRI results. The cortical regions of interest (ROIs) in each of the individual hemispheres were identified from the reconstructed brain of each participant according to the automatic anatomical labeling template, using Desikan-Killiany atlases to define ROI [36]. The cortical surface of each subject was downsampled to 15,000 vertices. The standardized low resolution brain electromagnetic tomography (sLORETA) was then used to extract time series for each vertex [37] (See Brainstorm Tutorials for details, <http://neuroimage.usc.edu/brainstorm/Tutorials>). sLORETA was based on minimum-norm estimation (MNE) and the cortical source activities (current density) were normalized with an individual estimate of the source standard deviation at each point. MNE can fit the MEG data through a forward model with a solution of minimum energy. The method has

been identified as an efficient tool for functional mapping, since it is consistent with physiology and capable of correcting localization. Subsequently, the dynamic current strengths of the source activity at grid points within each ROI were averaged to represent the cortical source dynamics of each ROI. Based on the time-varying source strengths, the IC, which is insensitive to volume conduction effects [38], was used to estimate the functional connectivity between each pair of ROIs. The details of our IC calculations have recently been published [20]. IC calculation resulted in a full 68 × 68 adjacency matrix between ROIs for each individual. The flowchart for the brain-network construction is displayed in Figure 1.

In general, networks can be represented by graphs that consist of sets of nodes and the corresponding sets of links between the nodes [22, 39]. In this sense, ROIs are considered to be the nodes of a network and the IC values are considered to be the links between them. We calculated graph-theory metrics from these weighted matrices using the GRETNA toolbox [40] (<https://www.nitrc.org/projects/gretna/>) running in Matlab (version 8.1 (R2013a) Mathworks Inc.). The sparsity threshold used for constructing weighted networks was set from 5% (5% strongest connections (edges) were kept along with their weights) to 40%, with step size of 1%, of all the possible connections within networks, generating 36 thresholded weighted networks consequently.

2.7. Feature Extraction. Calculation of graph-theory measures provides three features to characterize the network's nodal properties in this work, including, nodal degree (D), nodal efficiency (E), and betweenness centrality (B).

Measures of node centrality can effectively describe the importance of individual nodes in the network. The nodal degree is considered a basic and important measure of centrality and represents how strongly one node is interacting, structurally, and functionally, with other nodes in the network. Besides node degree, measures of centrality may be based on the length or number of shortest paths between nodes [21]. The weighted degree of node i is defined as

$$D_i^w = \sum_{j \in N} w_{ij}, \quad (1)$$

where N is the set of all nodes in the network and w_{ij} is the connection weight of the link between nodes i and j ($i, j \in N$).

Nodal efficiency is one of the most common measures of integration and can be considered as the average inverse shortest path length [41]. The weighted nodal efficiency is defined as

$$E_i^w = \frac{1}{n-1} \sum_{j \in N, j \neq i} (d_{ij}^w)^{-1}, \quad (2)$$

where n is the number of nodes and d_{ij}^w is the shortest weighted path length between nodes i and j .

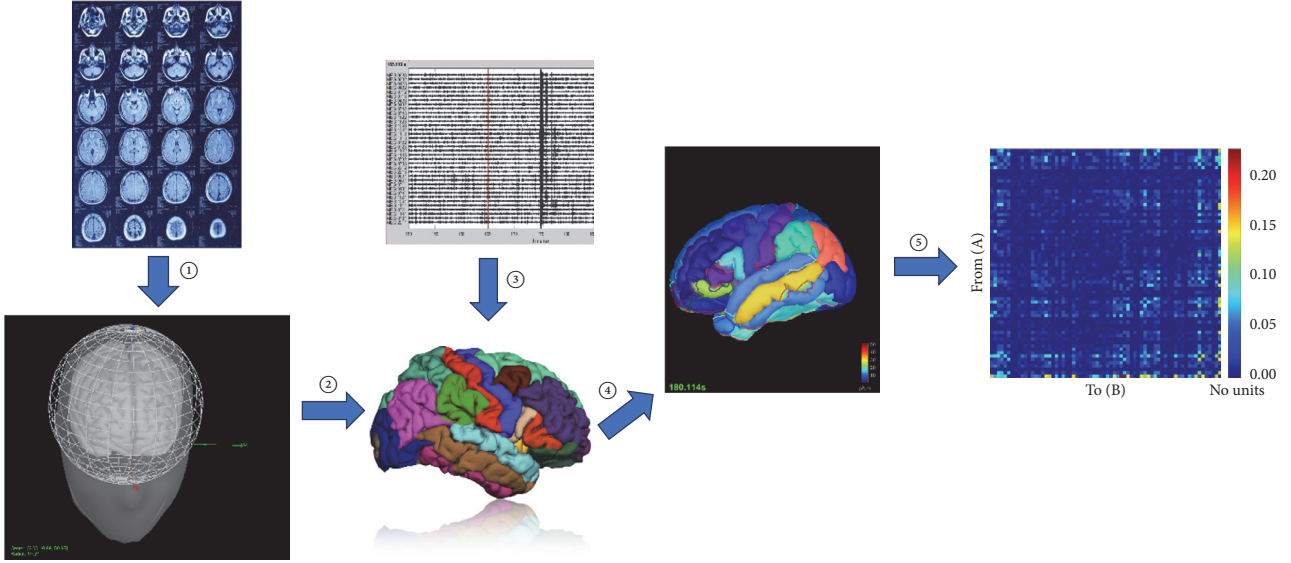


FIGURE 1: Flowchart showing the brain-network construction of spontaneous MEG based on the Desikan-Killiany Atlas. Numbers indicate the five steps. Step (1): individual MRI slices were input into Freesurfer to create the brain-structure model. In this step, the skull and cortex were recognized and their boundary surfaces were determined. The single sphere-based MEG forward model was employed to calculate MEG lead fields. Step (2): the cortex was partitioned into regions based on the Desikan-Killiany Atlas in preparation. Step (3): filtered MEG recordings were projected using the inverse problem algorithm (sLORETA) on the cortices of individual participants to obtain time series for each voxel. Step (4): the time series were averaged over each atlas to produce 68 atlas-based time courses. Step (5): the connectivity matrix was constructed using the 68 atlas time courses in preparation for network parameter calculation.

Betweenness centrality based on the number of shortest paths between nodes is a relatively sensitive measure of centrality [42]. The weighted betweenness centrality is defined as

$$B_i^w = \frac{1}{(n-1)(n-2)} \sum_{\substack{h,j \in N \\ h \neq j, h \neq i, j \neq i}} \frac{\rho_{hj}^{w(i)}}{\rho_{hj}^w}, \quad (3)$$

where ρ_{hj}^w is the number of shortest weighted paths between nodes h and j and $\rho_{hj}^{w(i)}$ is the number of shortest weighted paths between nodes h and j that pass through node i .

For each given threshold of network sparsity 68 node-based metrics were extracted from the segmented ROIs of each participant and the network metrics over 36 thresholds were used to construct the feature vectors for each metric and each subject. All the thresholds were gone through. The optimal threshold that can provide the highest classification accuracy was selected to construct the prediction model.

2.8. Support Vector Machine Classification. An SVM is a classifier that can automatically learn (supervised learning) and produce a decision hyperplane to classify new examples [43, 44]. In this study, a radial basis function kernel SVM (RBF-SVM) was used to distinguish between the groups (left TLE versus healthy controls, right TLE versus healthy controls, and left TLE versus right TLE). In contrast to linear SVM, RBF-SVM can provide a nonlinear boundary using the kernel trick to transform a nonlinear space into a higher dimensional space [45]. The RBF is commonly seen in $K(x_i, y_j) = \exp(-\|x_i - y_j\|^2 / 2\sigma^2)$, where σ^2 is the variance of the Gaussian

kernel [5, 46]. Principal component analysis (PCA) was used to further reduce the resulting feature space [47]. SVM computing was performed using the LIBSVM toolbox, available at <https://www.csie.ntu.edu.tw/~cjlin/libsvm> [48].

We used the leave-one-subject-out cross-validation in this study. In each step, one subject in class 1 and one subject in class 2 construct a test set, and all the left data are treated as a training set. For example, in case of left TLE versus right TLE, the left and right TLE groups, respectively, contain 15 subjects. In the cross validation, one subject from left TLE group forms the test set with anyone subject from right TLE group, exhaustively obtaining $15 \times 15 = 225$ combinations corresponding to a series of binary classifications. Mixing one subject's data in both training and test sets will give the algorithm prior knowledge and cause fake high accuracy. Hence, the leave-one-subject-out cross validation is a fair evaluation scheme to truly reveal the robustness of the classifier on overcoming individual differences. In other words, this is an out-of-sample strategy to ensure the generalizability of the established classifier for out-of-sample individual subjects [49–51].

A confusion matrix was used to evaluate the performance of the algorithm. The lateralization problem was specified into three binary classifications, including, right TLE versus healthy control, left TLE versus healthy control, and, most importantly, left TLE versus right TLE. For each task, samples in the first class were considered “positive” while samples in the second class were considered “negative.” Therefore, for each test sample, a binary classifier has four possible outcomes: True positive (TP); False positive (FP); True negative (TN); False negative (FN).

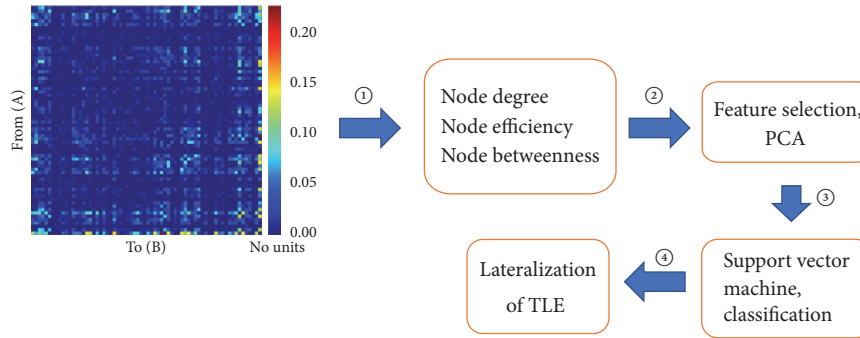


FIGURE 2: Flowchart showing the network parameter-based determination of TLE lateralization. First, based on the connectivity matrix shown in Figure 1, node-related network parameters (node degree, node efficiency, and node betweenness) were calculated (step 1)). Node degree is considered a basic and important measure of centrality and represents how strongly one node is interacting, structurally and functionally, with other nodes in the network. Node efficiency is one of the most common measures of integration and can be considered as the average inverse shortest path length. Node betweenness based on the number of shortest paths between nodes is a relatively sensitive measure of centrality. The parameters were then incorporated into feature vectors. Here, we conducted dimension reduction using PCA (step 2)). The optimal feature vectors were then input into an SVM for classification (step 3)). Finally, by training the SVM, unilateral TLE could be classified with a high degree of accuracy.

Five values in the confusion matrix are employed to evaluate the performance of the algorithm:

$$\begin{aligned} \text{Accuracy} &= (\text{TP} + \text{TN}) / (\text{TP} + \text{FP} + \text{TN} + \text{FN}); \\ \text{Sensitivity} &= \text{TP} / (\text{TP} + \text{FN}); \text{ Specificity} = \text{TN} / (\text{FP} + \text{TN}); \\ \text{Positive Predictive Value, PPV} &= \text{TP} / (\text{TP} + \text{FP}); \\ \text{Negative Predictive Value, NPV} &= \text{TN} / (\text{FN} + \text{TN}). \end{aligned}$$

The flowchart of the RBF-SVM classification is shown in Figure 2.

2.9. Principal Component Analysis (PCA). PCA is a statistical procedure that uses an orthogonal transformation to convert a set of observations of possibly correlated variables into a set of values of linearly uncorrelated variables called principal components. It is used here to reduce the dimensions of feature vector in classification. A relatively smaller dimension may improve the computational efficiency, especially in problems with a large number of samples and a high dimension of feature vectors. Meanwhile, the PCA operation may drop useless components in the feature vector, producing higher confusion matrix values.

The algorithm traverses n (1–68) of the 68 PCA components corresponding to the descending order of eigenvalues. Only the optimal n components are retained to construct the prediction model.

3. Results

Although SVM is a powerful tool for classification, the convolution-based algorithm operation is usually very time-consuming. Before using SVM, it is still valuable to inspect whether the network metrics can classify different groups without the assistance of SVM. Group differences of 68 brain regions in the network metrics calculated based on the optimal threshold were tested with two-tailed t -tests

for independent samples. The brain regions with between-group differences ($P < 0.05$, uncorrected) are displayed in Table 1. False discovery rate (FDR) correction [52] ($q < 0.05$) was used to control for multiple comparisons. None of the significant differences survived the FDR correction. This result suggests the need for mapping of the feature vectors into the higher dimensional space, making it possible to distinguish the MEG data by a powerful classifier, such as RBF-SVM.

The RBF-SVM was utilized to build a nonlinear model that predicted TLE laterality based on the brain-network features using a leave-one-subject-out cross-validation strategy. The performance of the RBF-SVM classification was estimated by calculating the confusion matrix values as defined above. The classification performance between groups was shown in Table 2. For nodal degree (D), the RBF-SVM classifiers achieved the highest classification accuracy for left TLE versus healthy controls (80.76%). For nodal efficiency (E), the resulting classifiers gained an appropriate level of accuracy both for the left TLE versus healthy controls (77.38%) and for right TLE versus healthy controls (73.81%). The betweenness centrality (B) provided the lowest accuracy in left TLE versus healthy controls and right TLE versus healthy controls. However, for left TLE versus right TLE, B achieved the highest accuracy (88.10%), making it the best feature for lateralization of TLE in patients' groups.

4. Discussion

The feature vectors were constructed from the network measures based on brain regions in the source space, rather than the sensor nodes over the scalp. Each brain region with an anatomical or functional label from a given atlas has its own size and shape, whereas the sensor nodes are equal-sized planes, which are approximately equidistributed over the scalp [18]. Although TLE can result in pathophysiological changes in some brain regions, changes might not be

TABLE 1: Brain regions with significant differences ($P < 0.05$, two-tailed t -test, uncorrected) in nodal parameters between the groups.

Brain region	Left TLE versus Right TLE			Left TLE versus HC			Right TLE versus HC		
	D	B	E	D	B	E	D	B	E
bankssts L								0.0427	
entorhinal L							0.0154		
frontalpole L								0.0408	
frontalpole R							0.0195		0.0398
inferiortemporal R								0.0289	
lateraloccipital R	0.0189	0.0356		0.0323					
medialorbitofrontal L	0.0238	0.0236	0.0282		0.0114				
parahippocampal L							0.0475		
parsorbitalis L	0.0198		0.0442	0.0181					
parstriangularis R				0.0433		0.0370			
postcentral L			0.0412						
postcentral R								0.0422	
precuneus R							0.0466		
rostralmiddlefrontal L			0.0500						
rostralmiddlefrontal R			0.0340		0.0412				
superiorfrontal R		0.0149			0.0216				
superiorparietal L	0.0199		0.0182						
superiortemporal L	0.0137	0.0163	0.0219		0.0176				
superiortemporal R		0.0168			0.0455				
supramarginal R	0.0296	0.0361							0.0332
temporalpole L	0.0193		0.0455				0.0356		
temporalpole R							0.0091		0.0189
transversetemporal R							0.0441		0.0075

None of the significant differences survived the FDR correction. TLE: temporal lobe epilepsy; HC: healthy control; D : degree; B : betweenness; E : efficiency; L: left; R: right.

TABLE 2: Classification performance between groups.

RBF-SVM classification	D	B	E
Left TLE versus HC			
Sensitivity	80.95%	76.19%	76.19%
Specificity	78.57%	71.43%	78.57%
PPV	82.82%	77.26%	78.21%
NPV	85.83%	72.62%	81.39%
Accuracy	80.76%	73.81%	77.38%
Right TLE versus HC			
Sensitivity	80.95%	66.67%	78.57%
Specificity	69.05%	64.29%	69.05%
PPV	75.60%	75.64%	77.98%
NPV	75.60%	64.03%	75.12%
Accuracy	75.00%	65.48%	73.81%
Left TLE versus Right TLE			
Sensitivity	73.81%	88.10%	73.81%
Specificity	73.81%	88.10%	76.19%
PPV	79.40%	90.60%	78.81%
NPV	79.40%	89.88%	78.10%
Accuracy	73.81%	88.10%	75.00%

HC: healthy control; D : nodal degree; B : betweenness centrality; E : nodal efficiency.

evenly spaced in the cerebral cortex. On the other hand, network analysis in source space using MEG recordings has been increasingly applied to neuroscience and neurological disorders [53]. Therefore, we selected the brain regions as the basic unit (network node) to calculate the network measures, which were taken as feature vectors for the SVM.

The metrics used to measure the connectivity between each pairs of nodes within networks also should be carefully selected. Compared with the other volume conduction insensitive measures, such as the phase lag index (PLI) [54] and the weighted phase lag index (WPLI) [55], IC is not the newest and is thought to systematically underestimate the true coupling strength because it normalizes the imaginary component via signal amplitudes [54]. However, IC is still a widely used technique for revealing altered FC and has been applied in cases of brain tumors [56], brain lesions [57], and other disorders. In addition, in source-level network analyses, the IC has been suggested to effectively represent the true coupling of two brain regions with a nonzero time delay using MEG data [31, 58]. Thus, we used the IC method to calculate the FC matrix for each subject in the source space.

In the current study, we took advantage of the nodal properties of the brain-network to classify unilateral TLE patients and healthy controls through RBF-SVMs that were trained and tested using the leave-one-subject-out cross-validation method. The classification accuracies were 73.81% to 80.76% for left TLE versus healthy controls, 65.48% to 75.00% for right TLE versus controls, and 73.81% to 88.10% for left TLE versus right TLE, respectively. Among the different classification tests, the best classification accuracy (88.10%) was obtained using betweenness centrality in left TLE versus right TLE. The current results reveal that not only nodal degree, but also betweenness centrality and nodal efficiency can achieve classification accuracies closely for unilateral TLE versus healthy controls. Interestingly, betweenness centrality performed better than nodal degree and nodal efficiency in our study when classifying left TLE and right TLE. To visually represent the results, we used a radar chart (Figure 3) to compare the relative confusion matrix values for three features. In the chart, a pentagon is used to represent the performance of each feature on five performance measures defined in the confusion matrix in the section above; for each feature, its five performance measures are represented by the five vertices of each pentagon in Figure 3. Better features occupy a larger area in the radar chart. It is clear that feature *B* (betweenness centrality) performed better in all confusion matrix values than *D* (degree) and *E* (nodal efficiency). The maximum difference between *B* and *D* was 14.29% on sensitivity, specificity, and accuracy. Similarly, the relative superior performance of betweenness centrality for left TLE versus right TLE makes it more valuable for clinical use, such as assisting epileptic foci localization.

Generally, a large dimension of feature vector may exponentially increase the complexity of the SVM classifier. As such, the value of feature vector dimension is desired as small as possible without compromising the classification accuracy. This is not a significant obstacle in the current research because the dimension is limited to a maximum value of 68 and the sample size of each class is only 45.

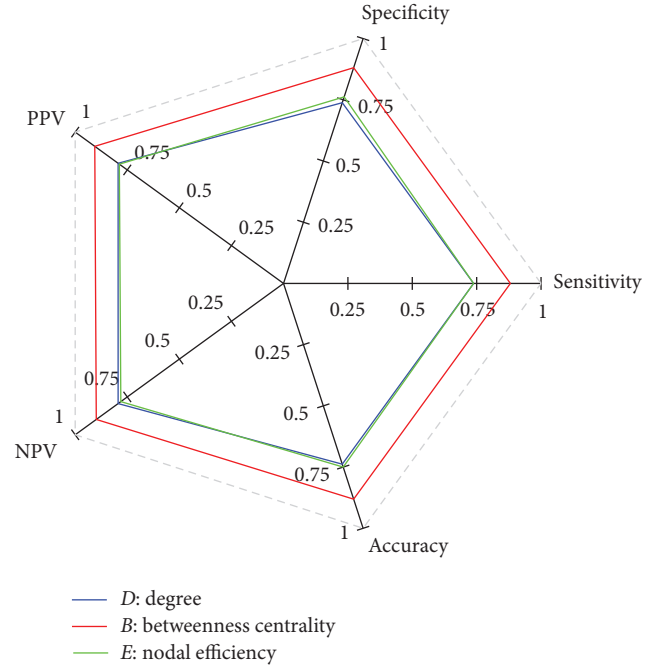


FIGURE 3: Radar chart of the performance of three features for left TLE versus right TLE. The output of each feature is represented by a pentagon in specific color. The outermost grey line means the 100% accuracy of the five values in the confusion matrix.

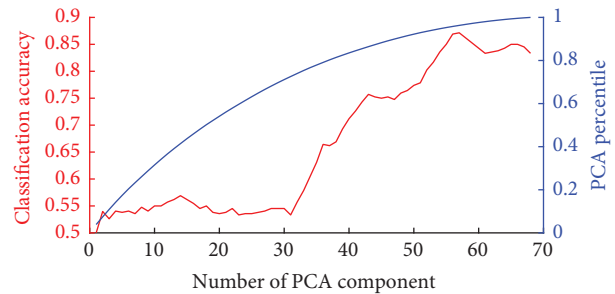


FIGURE 4: Variations in classification accuracy with number of PCA components. The x-axis represents the number of retained PCA components. The left y-axis represents the classification accuracy. The right y-axis represents the PCA percentile under different number of PCA components.

However, to give some references for further study, the issue was studied nevertheless. For space sake, we illustrated an additional experiment on the best feature (*B*, betweenness centrality) in the left TLE versus right TLE classification to demonstrate the effect of PCA in our study. Figure 4 indicates the relationship between classification accuracy and the number of PCA components according to the descending order of eigenvalues. The classification accuracy increases with the number of PCA components and plateaus at 55 (95% percentile) with the classification accuracy of 88.10%, achieving the dimensionality reduction at $(68 - 55)/68 = 19.12\%$. The relationship between the number of PCA components and the classification accuracy maintained a similar pattern in other classification cases.

The current study has two advantages that should be considered. First, similar to a previous study [10], our study used a graph-based approach in which the nodal properties of the brain-network were input into the SVM. Evidence indicates that unilateral TLE is a network disease rather than a disease with a single focal region [23–26]. Additionally, graph-theory metrics are able to summarize the network properties with less computational cost than the voxel-based and skeleton-based methods [8, 10, 59]. Additionally, for classification of TLE lateralization, MEG has higher temporal resolution than MRI [9, 45], fMRI [33], or DTI [8, 10, 59]. Thus, method that can analyze the effects of different frequency bands, especially the frequency band in which epileptiform discharges, was generated. Studies have shown that asymmetric and slow activity of the delta band (1–4 Hz) can reliably lateralize to the epileptogenic hemisphere [14, 60–62]. Indeed, significant differences in delta band activity were found between TLE patients and controls in network analyses [31, 63, 64]. Thus, we only selected one frequency band, the delta band, as our frequency band of interest. Although we propose that delta band-based network metrics are optimal for selection of lateralization, further investigation is warranted to identify and confirm the bands with the best lateralization outcomes.

The large age range of the subjects in the current study should be considered as a potential limitation. Because a relatively small number of suitable patients were available, it was difficult to recruit enough patients within a narrow age range. To enhance the reliability of our results, we plan to conduct future studies of TLE lateralization in a patient sample with a smaller age range.

Clinically, it is more significant to improve the classification accuracy in left TLE versus right TLE than to increase the one in TLE patients versus healthy controls. Our results indicate that the network feature of D is better than B and E in classifying left and right TLE with healthy control, with accuracies of 80.76% and 75.00%, respectively. However, in the classification of left TLE and right TLE, the metric B has better classification accuracy (88.10%) than D and E , which is significant for determining lateralization of unilateral TLE in clinic. Our results can be compared with those from a recent study [10] that also utilized an SVM approach to determine lateralization of the TLE epileptogenic focus. In that study, the input vectors were four graph-theory metrics that were based on DTI signals. Interestingly, and in line with our findings, their results indicated that for left TLE versus healthy control, and right TLE versus healthy control, classifiers based on nodal degree (D) had the best classification performance compared with the other three measures. For left TLE versus right TLE, their results showed the metric B had the highest classification accuracy. Thus, we suggest that, in clinic, when identifying TLE patients from controls, the metric D is an optimal choice, and when evaluating lateralization of unilateral TLE, the metric B will be a better one.

5. Conclusion

As a relatively new noninvasive clinical recording system, MEG is a powerful tool for epilepsy diagnosis. However, MEG is seldom applied for determining lateralization of

unilateral TLE. This study demonstrated that MEG is a good candidate for solving the classification problem of unilateral TLE and that MEG source space brain-network features can be effectively used for determining lateralization. The classification accuracy using the RBF-SVM method based on betweenness centrality was able to achieve an accuracy of 88.10% for TLE lateralization.

Disclosure

The funders had no role in the study design, data collection and analysis, decision to publish, or preparation of the manuscript.

Conflicts of Interest

The authors declare that they have no financial conflicts of interest.

Authors' Contributions

Ting Wu designed the experiments and wrote the paper. Qiqi Chen and Rui Zhang carried out the experiments and data collection. Junpeng Zhang, Wenyu Zhang, Yuejun Li, Duo Chen, and Ling Zhang performed statistical analyses and data interpretation. Suiren Wan and Junpeng Zhang reviewed and revised the manuscript. Tianzi Jiang and Junpeng Zhang conceived and designed the experiments.

Acknowledgments

The authors thank Adam Phillips, Ph.D., from Liwen Bianji, Edanz Group, China (<https://www.liwenbianji.cn/ac>), for editing the English text of a draft of this manuscript. They also thank Yifan Zhang, Zhiqiang Ni, Qi Xie, and Jingxuan Cui from Sichuan University for helping them import MEG data into Brainstorm and conduct primary analysis. This work was supported by the Nanjing Medical Science and Technique Development Foundation, the Nanjing Health Young Talent Training Project, the Six Great Talent Peak Plan of Jiangsu (2015-WSN-072), NSFC Grants (nos. 81470085 and 31271204), and Chengdu Project on Promoting Science and Technology for Benefitting the People (no. 2016-HM01-00462-SF).

References

- [1] Z. Haneef, A. Lenartowicz, H. J. Yeh, H. S. Levin, J. Engel Jr., and J. M. Stern, "Functional connectivity of hippocampal networks in temporal lobe epilepsy," *Epilepsia*, vol. 55, no. 1, pp. 137–145, 2014.
- [2] B. C. Bernhardt, S. J. Hong, A. Bernasconi, and N. Bernasconi, "Imaging structural and functional brain networks in temporal lobe epilepsy," *Frontiers in Human Neuroscience*, vol. 7, article 624, 14 pages, 2013.
- [3] C. LoPinto-Khoury, M. R. Sperling, C. Skidmore et al., "Surgical outcome in PET-positive, MRI-negative patients with temporal lobe epilepsy," *Epilepsia*, vol. 53, no. 2, pp. 342–348, 2012.

- [4] I. Y. Capraz, G. Kurt, Ö. Akdemir et al., "Surgical outcome in patients with MRI-negative, PET-positive temporal lobe epilepsy," *Seizure*, vol. 29, pp. 63–68, 2015.
- [5] A. S. M. Murugavel and S. Ramakrishnan, "Hierarchical multi-class SVM with ELM kernel for epileptic EEG signal classification," *Medical & Biological Engineering & Computing*, vol. 54, no. 1, pp. 149–161, 2016.
- [6] S. Siuly and Y. Li, "Designing a robust feature extraction method based on optimum allocation and principal component analysis for epileptic EEG signal classification," *Computer Methods and Programs in Biomedicine*, vol. 119, no. 1, pp. 29–42, 2015.
- [7] C. Cortes and V. Vapnik, "Support-vector networks," *Machine Learning*, vol. 20, no. 3, pp. 273–297, 1995.
- [8] N. K. Focke, M. Yogarajah, M. R. Symms, O. Gruber, W. Paulus, and J. S. Duncan, "Automated MR image classification in temporal lobe epilepsy," *NeuroImage*, vol. 59, no. 1, pp. 356–362, 2012.
- [9] J. D. Rudie, J. B. Colby, and N. Salamon, "Machine learning classification of mesial temporal sclerosis in epilepsy patients," *Epilepsy Research*, vol. 117, pp. 63–69, 2015.
- [10] K. Kamiya, S. Amemiya, Y. Suzuki et al., "Machine learning of dti structural brain connectomes for lateralization of temporal lobe epilepsy," *Magnetic Resonance in Medical Sciences*, vol. 15, no. 1, pp. 121–129, 2016.
- [11] S. Braeutigam, "Magnetoencephalography: Fundamentals and Established and Emerging Clinical Applications in Radiology," *ISRN Radiology*, vol. 2013, pp. 1–18, 2013.
- [12] E. Foley, A. Cerquiglini, A. Cavanna et al., "Magnetoencephalography in the study of epilepsy and consciousness," *Epilepsy & Behavior*, vol. 30, pp. 38–42, 2014.
- [13] R. Hari and R. Salmelin, "Magnetoencephalography: From SQUIDs to neuroscience. Neuroimage 20th Anniversary Special Edition," *NeuroImage*, vol. 61, no. 2, pp. 386–396, 2012.
- [14] D. J. Englot, S. S. Nagarajan, D. D. Wang et al., "The sensitivity and significance of lateralized interictal slow activity on magnetoencephalography in focal epilepsy," *Epilepsy Research*, vol. 121, pp. 21–28, 2016.
- [15] S. P. Burns, S. Santaniello, R. B. Yaffe et al., "Network dynamics of the brain and influence of the epileptic seizure onset zone," *Proceedings of the National Academy of Sciences of the United States of America*, vol. 111, no. 49, pp. E5321–E5330, 2014.
- [16] B. A. Assaf, K. M. Karkar, K. D. Laxer et al., "Magnetoencephalography source localization and surgical outcome in temporal lobe epilepsy," *Clinical Neurophysiology*, vol. 115, no. 9, pp. 2066–2076, 2004.
- [17] C. T. Anderson, C. E. Carlson, Z. Li, and M. Raghavan, "Magnetoencephalography in the preoperative evaluation for epilepsy surgery," *Current Neurology and Neuroscience Reports*, vol. 14, no. 5, 2014.
- [18] R. Enatsu, N. Mikuni, K. Usui et al., "Usefulness of MEG magnetometer for spike detection in patients with mesial temporal epileptic focus," *NeuroImage*, vol. 41, no. 4, pp. 1206–1219, 2008.
- [19] K. Kaiboriboon, S. Nagarajan, M. Mantle, and H. E. Kirsch, "Interictal MEG/MSI in intractable mesial temporal lobe epilepsy: Spike yield and characterization," *Clinical Neurophysiology*, vol. 121, no. 3, pp. 325–331, 2010.
- [20] T. Wu, S. Ge, R. Zhang et al., "Neuromagnetic coherence of epileptic activity: An MEG study," *Seizure*, vol. 23, no. 6, pp. 417–423, 2014.
- [21] M. Rubinov and O. Sporns, "Complex network measures of brain connectivity: Uses and interpretations," *NeuroImage*, vol. 52, no. 3, pp. 1059–1069, 2010.
- [22] O. Sporns, D. R. Chialvo, M. Kaiser, and C. C. Hilgetag, "Organization, development and function of complex brain networks," *Trends in Cognitive Sciences*, vol. 8, no. 9, pp. 418–425, 2004.
- [23] S. Chiang and Z. Haneef, "Graph theory findings in the pathophysiology of temporal lobe epilepsy," *Clinical Neurophysiology*, vol. 125, no. 7, pp. 1295–1305, 2014.
- [24] L. Bonilha, C. Rorden, J. J. Halford et al., "Asymmetrical extra-hippocampal grey matter loss related to hippocampal atrophy in patients with medial temporal lobe epilepsy," *Journal of Neurology, Neurosurgery & Psychiatry*, vol. 78, no. 3, pp. 286–294, 2007.
- [25] B. M. de Campos, A. C. Coan, C. Lin Yasuda, R. F. Casseb, and F. Cendes, "Large-scale brain networks are distinctly affected in right and left mesial temporal lobe epilepsy," *Human Brain Mapping*, vol. 37, no. 9, pp. 3137–3152, 2016.
- [26] F. Pittau, C. Grova, F. Moeller, F. Dubeau, and J. Gotman, "Patterns of altered functional connectivity in mesial temporal lobe epilepsy," *Epilepsia*, vol. 53, no. 6, pp. 1013–1023, 2012.
- [27] Y.-M. Shon, Y.-I. Kim, B.-B. Koo et al., "Group-specific regional white matter abnormality revealed in diffusion tensor imaging of medial temporal lobe epilepsy without hippocampal sclerosis," *Epilepsia*, vol. 51, no. 4, pp. 529–535, 2010.
- [28] L. Su, J. An, Q. Ma, S. Qiu, and D. Hu, "Influence of resting-state network on lateralization of functional connectivity in mesial temporal lobe epilepsy," *American Journal of Neuroradiology*, vol. 36, no. 8, pp. 1479–1487, 2015.
- [29] N. L. Voets, C. F. Beckmann, D. M. Cole, S. Hong, A. Bernasconi, and N. Bernasconi, "Structural substrates for resting network disruption in temporal lobe epilepsy," *Brain*, vol. 135, no. 8, pp. 2350–2357, 2012.
- [30] H. Zhu, J. Zhu, T. Zhao et al., "Alteration of interictal brain activity in patients with temporal lobe epilepsy in the left dominant hemisphere: A resting-state meg study," *BioMed Research International*, vol. 2014, Article ID 171487, 2014.
- [31] F.-J. Hsiao, H.-Y. Yu, W.-T. Chen et al., "Increased intrinsic connectivity of the default mode network in temporal lobe epilepsy: evidence from resting-state MEG recordings," *PLoS ONE*, vol. 10, no. 6, Article ID e0128787, 2015.
- [32] S.-H. Jin, W. Jeong, and C. K. Chung, "Mesial temporal lobe epilepsy with hippocampal sclerosis is a network disorder with altered cortical hubs," *Epilepsia*, vol. 56, no. 5, pp. 772–779, 2015.
- [33] Z. Yang, J. Choupan, D. Reutens, and J. Hocking, "Lateralization of temporal lobe epilepsy based on resting-state functional magnetic resonance imaging and machine learning," *Frontiers in Neurology*, vol. 6, article no. 184, 2015.
- [34] ILAE, "Proposal for revised classification of epilepsies and epileptic syndromes. Commission on Classification and Terminology of the International League Against Epilepsy," *Epilepsia*, vol. 30, no. 4, pp. 389–399, 1989.
- [35] F. Tadel, S. Baillet, J. C. Mosher, D. Pantazis, and R. M. Leahy, "Brainstorm: a user-friendly application for MEG/EEG analysis," *Computational Intelligence and Neuroscience*, vol. 2011, Article ID 879716, 13 pages, 2011.
- [36] R. S. Desikan, F. Ségonne, B. Fischl et al., "An automated labeling system for subdividing the human cerebral cortex on MRI scans into gyral based regions of interest," *NeuroImage*, vol. 31, no. 3, pp. 968–980, 2006.

- [37] R. D. Pascual-Marqui, "Standardized low-resolution brain electromagnetic tomography (sLORETA): technical details," *Methods and Findings in Experimental and Clinical Pharmacology*, vol. 24, pp. 5–12, 2002.
- [38] G. Nolte, O. Bai, L. Wheaton, Z. Mari, S. Vorbach, and M. Hallett, "Identifying true brain interaction from EEG data using the imaginary part of coherency," *Clinical Neurophysiology*, vol. 115, no. 10, pp. 2292–2307, 2004.
- [39] C. J. Stam and J. C. Reijneveld, "Graph theoretical analysis of complex networks in the brain," *EPJ Nonlinear Biomedical Physics*, vol. 1, no. 3, 2007.
- [40] J. Wang, X. Wang, M. Xia, X. Liao, A. Evans, and Y. He, "GRETNA: A graph theoretical network analysis toolbox for imaging connectomics," *Frontiers in Human Neuroscience*, vol. 9, article no. 386, 2015.
- [41] V. Latora and M. Marchiori, "Efficient behavior of small-world networks," *Physical Review Letters*, vol. 87, article no. 198701, 2001.
- [42] L. C. Freeman, "Centrality in social networks conceptual clarification," *Social Networks*, vol. 1, no. 3, pp. 215–239, 1978.
- [43] C. A. M. Lima, A. L. V. Coelho, and S. Chagas, "Automatic EEG signal classification for epilepsy diagnosis with Relevance Vector Machines," *Expert Systems with Applications*, vol. 36, no. 6, pp. 10054–10059, 2009.
- [44] N. Acir and C. Güzelış, "Automatic spike detection in EEG by a two-stage procedure based on support vector machines," *Computers in Biology and Medicine*, vol. 34, no. 7, pp. 561–575, 2004.
- [45] D. Cantor-Rivera, A. R. Khan, M. Goubran, S. M. Mirsattari, and T. M. Peters, "Detection of temporal lobe epilepsy using support vector machines in multi-parametric quantitative MR imaging," *Computerized Medical Imaging and Graphics*, vol. 41, pp. 14–28, 2015.
- [46] I. Goker, O. Osman, S. Ozekes, M. B. Baslo, M. Ertas, and Y. Ulgen, "Classification of juvenile myoclonic epilepsy data acquired through scanning electromyography with machine learning algorithms," *Journal of Medical Systems*, vol. 36, no. 5, pp. 2705–2711, 2012.
- [47] A. Subasi and M. I. Gursoy, "EEG signal classification using PCA, ICA, LDA and support vector machines," *Expert Systems with Applications*, vol. 37, no. 12, pp. 8659–8666, 2010.
- [48] C. Chang and C. Lin, "LIBSVM: a Library for support vector machines," *ACM Transactions on Intelligent Systems and Technology*, vol. 2, no. 3, article 27, 2011.
- [49] M. D. Rosenberg, E. S. Finn, D. Scheinost et al., "A neuromarker of sustained attention from whole-brain functional connectivity," *Nature Neuroscience*, vol. 19, no. 1, pp. 165–171, 2015.
- [50] J. Dubois and R. Adolphs, "Building a Science of Individual Differences from fMRI," *Trends in Cognitive Sciences*, vol. 20, no. 6, pp. 425–443, 2016.
- [51] E. S. Finn, X. Shen, D. Scheinost et al., "Functional connectome fingerprinting: Identifying individuals using patterns of brain connectivity," *Nature Neuroscience*, vol. 18, no. 11, pp. 1664–1671, 2015.
- [52] Y. Benjamini and Y. Hochberg, "Controlling the false discovery rate: a practical and powerful approach to multiple testing," *Journal of the Royal Statistical Society B: Methodological*, vol. 57, no. 1, pp. 289–300, 1995.
- [53] S. Baillet, "Magnetoencephalography for brain electrophysiology and imaging," *Nature Neuroscience*, vol. 20, no. 3, pp. 327–339, 2017.
- [54] C. J. Stam, G. Nolte, and A. Daffertshofer, "Phase lag index: assessment of functional connectivity from multi channel EEG and MEG with diminished bias from common sources," *Human Brain Mapping*, vol. 28, no. 11, pp. 1178–1193, 2007.
- [55] M. Vinck, R. Oostenveld, M. Van Wingerden, F. Battaglia, and C. M. A. Pennartz, "An improved index of phase-synchronization for electrophysiological data in the presence of volume-conduction, noise and sample-size bias," *NeuroImage*, vol. 55, no. 4, pp. 1548–1565, 2011.
- [56] J. Martino, S. M. Honma, A. M. Findlay et al., "Resting functional connectivity in patients with brain tumors in eloquent areas," *Annals of Neurology*, vol. 69, no. 3, pp. 521–532, 2011.
- [57] A. G. Guggisberg, S. M. Honma, A. M. Findlay et al., "Mapping functional connectivity in patients with brain lesions," *Annals of Neurology*, vol. 63, no. 2, pp. 193–203, 2008.
- [58] A. Elshahabi, S. Klamer, A. K. Sahib, H. Lerche, C. Braun, and N. K. Focke, "Magnetoencephalography reveals a widespread increase in network connectivity in idiopathic/genetic generalized epilepsy," *PLoS ONE*, vol. 10, no. 9, Article ID e0138119, 2015.
- [59] J. An, P. Fang, W. Wang, Z. Liu, D. Hu, and S. Qiu, "Decreased white matter integrity in mesial temporal lobe epilepsy: A machine learning approach," *NeuroReport*, vol. 25, no. 10, pp. 788–794, 2014.
- [60] J. C. Baayen, A. De Jongh, C. J. Stam et al., "Localization of Slow Wave Activity in Patients with Tumor-Associated Epilepsy," *Brain Topography*, vol. 16, no. 2, pp. 85–93, 2003.
- [61] M. Koutroumanidis, C. Martin-Miguel, M. J. Hennessy et al., "Interictal temporal delta activity in temporal lobe epilepsy: Correlations with pathology and outcome," *Epilepsia*, vol. 45, no. 11, pp. 1351–1367, 2004.
- [62] S. J. M. Smith, "EEG in the diagnosis, classification, and management of patients with epilepsy," *Neurology in Practice*, vol. 76, no. 2, pp. ii2–ii7, 2005.
- [63] M. A. Quraan, C. McCormick, M. Cohn, T. A. Valiante, and M. P. McAndrews, "Altered Resting State Brain Dynamics in Temporal Lobe Epilepsy Can Be Observed in Spectral Power, Functional Connectivity and Graph Theory Metrics," *PLoS ONE*, vol. 8, no. 7, Article ID e68609, 2013.
- [64] S. C. Ponten, F. Bartolomei, and C. J. Stam, "Small-world networks and epilepsy: graph theoretical analysis of intracerebrally recorded mesial temporal lobe seizures," *Clinical Neurophysiology*, vol. 118, no. 4, pp. 918–927, 2007.

Research Article

Automated Epileptic Seizure Detection in Scalp EEG Based on Spatial-Temporal Complexity

Xinzhong Zhu,^{1,2,3} Huiying Xu,³ Jianmin Zhao,³ and Jie Tian²

¹School of Life Science and Technology, Xidian University, Xi'an, Shaanxi, China

²CAS Key Lab of Molecular Imaging, Institute of Automation, Chinese Academy of Sciences, Beijing, China

³College of Mathematics, Physics and Information Engineering, Zhejiang Normal University, Jinhua, Zhejiang, China

Correspondence should be addressed to Xinzhong Zhu; zxz@zjnu.edu.cn and Jie Tian; tian@ieee.org

Received 23 September 2017; Revised 17 November 2017; Accepted 23 November 2017; Published 27 December 2017

Academic Editor: Gaoxiang Ouyang

Copyright © 2017 Xinzhong Zhu et al. This is an open access article distributed under the Creative Commons Attribution License, which permits unrestricted use, distribution, and reproduction in any medium, provided the original work is properly cited.

Epilepsy is a group of neurological disorders characterized by epileptic seizures, wherein electroencephalogram (EEG) is one of the most common technologies used to diagnose, monitor, and manage patients with epilepsy. A large number of EEGs have been recorded in clinical applications, which leads to visual inspection of huge volumes of EEG not routinely possible. Hence, automated detection of epileptic seizure has become a goal of many researchers for a long time. A novel method is therefore proposed to construct a patient-specific detector based on spatial-temporal complexity analysis, involving two commonly used entropy-based complexity analysis methods, which are permutation entropy (PE) and sample entropy (SE). The performance of spatial-temporal complexity method is evaluated on a shared dataset. Results suggest that the proposed epilepsy detectors achieve promising performance: the average sensitivities of PE and SE in 23 patients are 99% and 96.6%, respectively. Moreover, both methods can accurately recognize almost all the seizure-free EEG. The proposed method not only obtains a high accuracy rate but also meets the real-time requirements for its application on seizure detection, which suggests that the proposed method has the potential of detecting epileptic seizures in real time.

1. Introduction

Epilepsy affects more than 50 million individuals worldwide [1] and is characterized by the spontaneous and unforeseeable occurrence of seizures [2], which may result in a general convulsion or a lack of attention. Frequent seizures bring individual's risk of continuing physical injuries and may even lead to death. Electroencephalography (EEG) is an effective and noninvasive technique for directly recording the brain electrical activity and diagnosing clinical brain diseases [3]. Abnormal epileptic waveforms appear in EEG signal during the epileptic seizure phase. For epilepsy patients, long-term EEG recording lasting several days is usually applied to localizing the epileptogenic foci in clinic. As a result, a large number of EEG data are recorded and then visually inspected by physicians for identifying seizure information in epilepsy patients. However, visual inspection of long EEG recordings by neurologists is a very cumbersome, time-consuming,

costly work, especially considering a large number of epilepsy patients. Furthermore, routine visual assessment of EEG is not a very objective process. Therefore, there is a great need for detection of epilepsy seizures automatically in order to reduce diagnosis time drastically.

It is well known that brain is a chaotic dynamical system and the brain data tend to exhibit complex fluctuations that contain information about the underlying dynamics [4, 5]. Therefore, nonlinear analysis could better facilitate revealing the mechanisms and characteristics of EEG. It has been found that the EEG from the location of epileptic foci owes strong indications of nonlinear determinism, while that from other zones exhibits linear stochastic dynamics [6], suggesting that nonlinear analysis of EEG in epilepsy may provide useful information for seizure detection. With the rapid development of nonlinearity theory, information entropy analysis is becoming a predominant field to study nonlinear dynamics of EEG signal. One big advantage is that

it only needs hundreds of points to describe the entire system, compared with other nonlinear algorithms such as Lyapunov exponent which usually requires more than thousands of data points to obtain correct results [7].

Entropy represents the predictability (irregularity) of systems in information theory. Lower values of entropy always relate to less randomness and larger system order. Thus, many complexity concepts are related to entropy. Recently, entropy-based complexity methods have been used to analyze epileptic EEG data. Approximate entropy (ApEn) was first used to study normal and epileptic EEG data in [8]. A modified algorithm of ApEn, called sample entropy (SampEn), was then introduced for automatic epileptic seizure detection in EEG recordings [9]. Generally, ApEn is inherently biased because of incorrectly counting self-matches, while the calculation of SampEn overcomes this limitation, resulting in better performance in detecting seizures [10]. However, both these two algorithms are based on the amplitude of EEG data, which leads them to be vulnerable to the selection of reference electrode and the artifacts in EEG data [11]. Li et al. used another order pattern based entropy method (called permutation entropy, PE) as an indicator to predict the epileptic seizures in genetic absence epilepsy rats, and the results showed that PE can successfully detect pre-seizure phase in 169 of 314 seizures (54%), which was higher than SE (21%) in [12]. Permutation entropy was also applied to analyzing EEG data in patients with epilepsy, which demonstrated that the EEG during the seizure-free phase is characterized by a higher value of permutation entropy than the EEG during the seizure phase [13, 14].

Though the entropy-based complexity methods have shown promising results on detection of epileptic seizures [3, 12, 15, 16], it is still an open problem how to bring out the full potential of complexity to enhance the reliability and accuracy of EEG analysis. Meanwhile, some methods only have promising results for selected patients with seizure of single type (such as temporal lobe seizure); the reproducibility and reliability of the results have been questioned when being tested on other patients with numerous seizure types [17]. Furthermore, the characteristics of EEG vary significantly across patients. And this cross-patient variability in seizure and nonseizure activity causes patient nonspecific classifiers to exhibit poor accuracy or long delays in declaring the onset of a seizure. To overcome these problems, in this study, a generalized spatial-temporal complexity method is proposed to develop a high-performance patient-specific seizure detector. In our detector, the potential reason of high accuracy is a completely automated process for constructing a feature vector that unifies in a single feature space with the spatial properties of the electrical activity and time evolution of complexity in brain. Previous patient-specific methods classified spatial and temporal features separately and required a skilled individual in interpreting the brain electrical activity to specify how such features should be integrated [18, 19].

In his study, both PE and SE are adopted to implement the proposed spatial-temporal complexity detector. To validate the performance of the proposed method, a shared dataset from CHB-MIT is used [20]. Results show that the

proposed epilepsy detectors achieve promising performance: the average sensitivities of PE and SE in 23 patients are 99% and 96.6%, respectively. Moreover, both the PE and SE-based detector can accurately recognize almost all the seizure-free EEG. As the proposed seizure detection method not only obtains high accuracy rate but also has a very fast computational speed, this suggests its huge potential on detecting epileptic seizures in real time.

2. Materials and Methods

2.1. EEG Datasets. In this paper, the performance of our proposed method was tested on a shared dataset, which has been widely used during the past few years. The EEG dataset was recorded from pediatric subjects with intractable seizures at Children's Hospital Boston. This database contains 22 subjects (17 females, ages 1.5–19; 5 males, ages 3–22) and can be downloaded from the PhysioNet website: <http://www.physionet.org/pn6/chbmit/>. The International 10-20 system of EEG electrode positions and nomenclature was used to collect these EEG recordings. All signals were sampled at 256 samples per second with 16-bit resolution and filtered within a frequency band from 0.5 Hz to 25 Hz. To characterize their seizures, patients were monitored for up to several days after the suspension of antiseizure medication. More details about the dataset can be found from [20].

Generally, seizure detection can be translated into a binary classification problem: ictal (the seizure phase) and interictal EEG (the seizure-free phase), in spite of the fact that the underlying physiological activity is multiclass. This is because it is neither easy nor practical for an expert to identify and label the subclasses of the seizure and seizure-free phases. In addition, dividing an EEG recording into two encompassing classes, seizure-free and seizure, is also consistent with standard clinical practices. In this database, EEG signal has been marked as “seizure” by experts in all channels from seizure start to end; EEG recordings out of the period of “seizure” were considered as “seizure-free.”

In this shared dataset, epilepsy patients were monitored for up to several days, resulting in that each patient contains between 9 and 42 continuous EDF files (also called records). In most cases, the record contains exactly one hour of digitized EEG data, except for a few records that contain two- or four-hour EEG data. Only the records containing at least a seizure (called seizure records) are used to train or validate the performance of our seizure detector. For each seizure record in a single subject, 300 interictal EEG epochs (4 seconds) are randomly selected from the seizure-free phase and 3 ictal EEG epochs (4 seconds) are randomly selected from the seizure phase. Why much more interictal EEG epochs are chosen is because seizure is a rare event relative to seizure-free event. In addition, only the first 20-second EEG of seizures are considered in this study, since this period is more clinically meaningful. Previous work demonstrated that artifact removal before seizure detection can improve the classification accuracy [21], while this work would not do any preprocessing to show the robustness of the proposed detector.

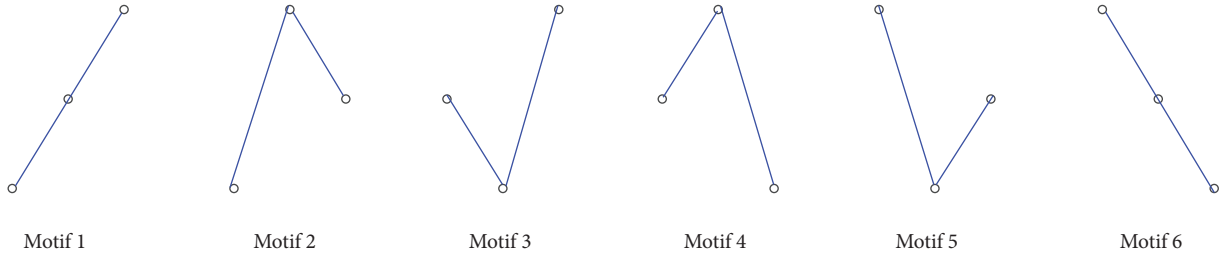


FIGURE 1: Six motifs for the embedding dimension $m = 3$, including “slopes,” “peaks,” and “troughs.”

2.2. Complexity Features. In all the entropy-based complexity methods, permutation entropy (PE) and sample entropy (SE) are two of the most common used methods for physiological signal analysis. Hence, this work adopts permutation entropy and sample entropy to construct detector, respectively.

2.2.1. Permutation Entropy. Permutation Entropy (PE), proposed by Bandt and Pompe, is a nature complexity measure for physiologic time series [22]. In this method, a time series is first mapped to a sequence of order patterns based on comparison of neighboring values, and then PE is calculated based on the statistical measure of relative frequencies of order patterns. Given a time series $(x_t, t = 1, 2, \dots, N)$, delay vectors $X_t = [x_t, x_{t+\tau}, \dots, x_{t+(m-1)\tau}]$ are constructed by an embedding procedure with embedding dimension, m , and time lag, τ . The vector is then arranged in an ascending order: $[x_{t+(j_1-1)\tau} \leq x_{t+(j_2-1)\tau} \leq \dots \leq x_{t+(j_d-1)\tau}]$. There will be $m!$ possible order patterns π (also known as motifs) for m different numbers. As shown in Figure 1, there are 6 different motifs for $m = 3$, which include “slopes,” “peaks,” and “troughs.” When $f(\pi_j)$ denotes the frequency of occurrence for motif π_j in the time series, the relative frequency is thus $p(\pi_j) = f(\pi_j)/(N - (m - 1)\tau)$. The permutation entropy is defined as

$$PE = - \sum_{\pi_j=1}^{m!} p(\pi_j) \log_2 p(\pi_j). \quad (1)$$

In practical use, PE is often normalized by $PE/\log_2(m!)$. The smallest value of PE is 0, which means that the time series is absolutely regular; the largest value of PE is 1, which means the time series is completely random. In other words, the smaller the PE is, the more regular the time series is. In the calculation of PE, only considering the ordinal patterns, the PE value is thus irrelevant to the amplitude of time series, meaning less sensitive to noise embedded in time series. In the EEG application, PE should be extracted from a reasonably short time epoch as EEG is nonstationary. However, EEG cannot be segmented into very short physiologically relevant units. For the sake of compromise, two-second long epoch is used in this study.

The calculation of PE depends on two parameters: embedding dimension (m) and time lag (τ). In general, a too small m will lead few possible motifs and thus a low sensitivity. On the other hand, there will be a high biased entropy when m is too high, since every motif will occur just

a few times. In all, it was shown that the choice of m depends on the length of data (N), with $m! \ll N$. As the length of each epoch is just 512 points (2 seconds), $m = 3$ is appropriate for this study. As for the time lag τ , the choice is critical for the frequency behavior of the signal. As some high frequency components will be discarded for $\tau > 2$, $\tau = 1$ is adopted in this study.

Following the onset of most seizure, brain dynamics develop rhythmic activity that is typically slow and monotonous, which means that ictal EEG is more regular than interictal EEG. As illustrated in Figure 2, the black curve in Figure 2(c) represents the time evolution of the PE values of FPI-F3 channel (Figure 2(b)), which was involved in a seizure and selected from a multichannel EEG recording in Patient I (Figure 2(a)). From Figure 2(b), it can be found that EEG wave following a seizure (onset at 2589 s) is slow and regular than the preceding EEG. And the corresponding PE values in the seizure phase are lower than those in seizure-free phase.

2.2.2. Sample Entropy. Sample entropy (SE), a modification of approximate entropy (AE), is usually used to assess the complexity of physiological signals [10]. SE has two advantages over AE: data length independence and a relative trouble-free implementation. For a given embedding dimension m , time lag τ , and tolerance r , SE is the negative logarithm of the probability that if two sets of simultaneous data points of length m have distance $< r$ then two sets of simultaneous data points of length $m + 1$ also have distance $< r$.

Given a time series $(x_t, t = 1, 2, \dots, N)$, we can construct delay vectors $X(m, t) = [x_t, x_{t+\tau}, \dots, x_{t+(m-1)\tau}]$ at time t with embedding dimension, m , and time lag, τ . If the distance between two vectors is defined as $d(X(m, t), X(m, t'))$, the number of vector pairs in delay vectors of length $m, m + 1$ having $d(X(m, t), X(m, t')) < r$ is counted and denoted by B and A , respectively. The sample entropy can be defined as

$$SE = - \log \frac{A}{B}. \quad (2)$$

It should be noted that A always has a value smaller or equal to B , meaning that SE is always either zero or a positive value. A small value of SE also indicates more self-similarity and regularity in the dataset. In general, $r = 0.2 \cdot \text{std}(x)$ is most common used and offers very good performances [9, 11]. To keep consistency with PE, $m = 3$ and $\tau = 1$ are set for SE.

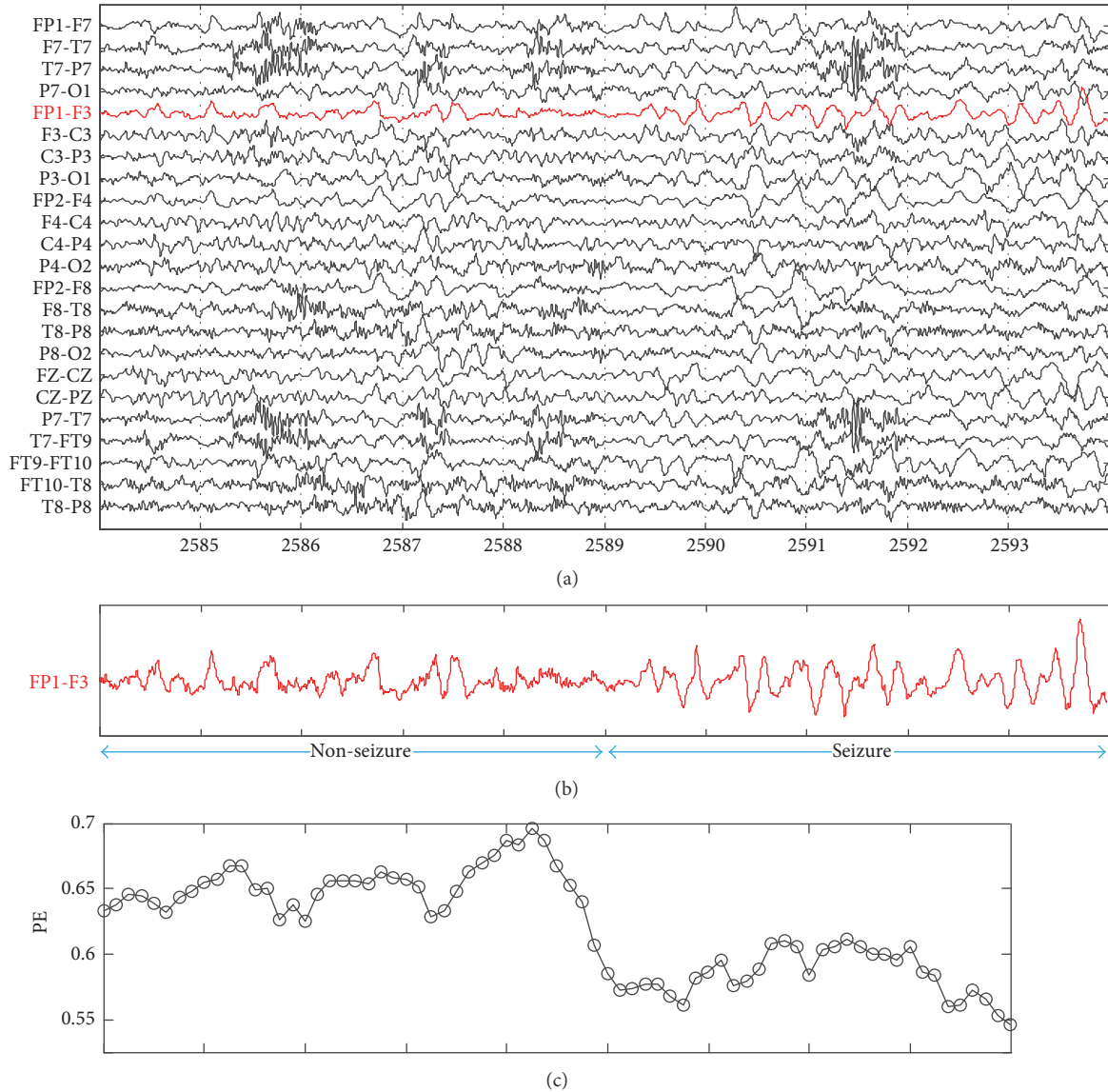


FIGURE 2: (a) The continuous multichannel EEG recording (23 channels) with a seizure in Patient I. (b) The EEG channel FP1-F3 involved in seizure activity. (c) Time evolution of the values of PE for FP1-F3 channel. The length of window is 1 s, and the step is 1/8 s. Almost all of the PE values in seizure state are lower than those in seizure-free state.

2.3. Spatial Features. The identity of the EEG channels involved in seizure can further differentiate seizure EEG from seizure-free EEG. This is because seizure types in this database belong to partial seizure or focal onset seizure (such as temporal lobe seizure), which has a focal origin. Hence, only a set of EEG channels develop rhythmic activity after the seizure onset. Moreover, the identity of the EEG channel involved and the structure of the rhythmic activity differ across individuals. For example, Figures 2 and 3 illustrate seizures from different patients. Patients I's seizure in Figure 2 begins at the 2589th second and is characterized by the appearance of rhythmic activity most prominent on the channels FP1-F3. Patients II's seizure in Figure 3 begins at the 1015th second and rhythmic activity develops most

prominently on channels P8-O2 and FT9-FT10 with the increase in amplitude and decrease in frequency.

In spite of the fact that seizures vary across individuals, the seizures of any given individual exhibit considerable consistency, provided that they emerge from the same brain region. Figure 4 illustrates another seizure from Patient I. It should be noted that the spatial and rhythm character of this seizure is similar to the seizure shown in Figure 2. To automatically capture the spatial complexity information contained within each two-second EEG epoch at time $t = T$, permutation entropies were extracted from each $N = 23$. EEG channels are concatenated, forming a feature vector H_T with N elements as shown in the middle portion of Figure 5.

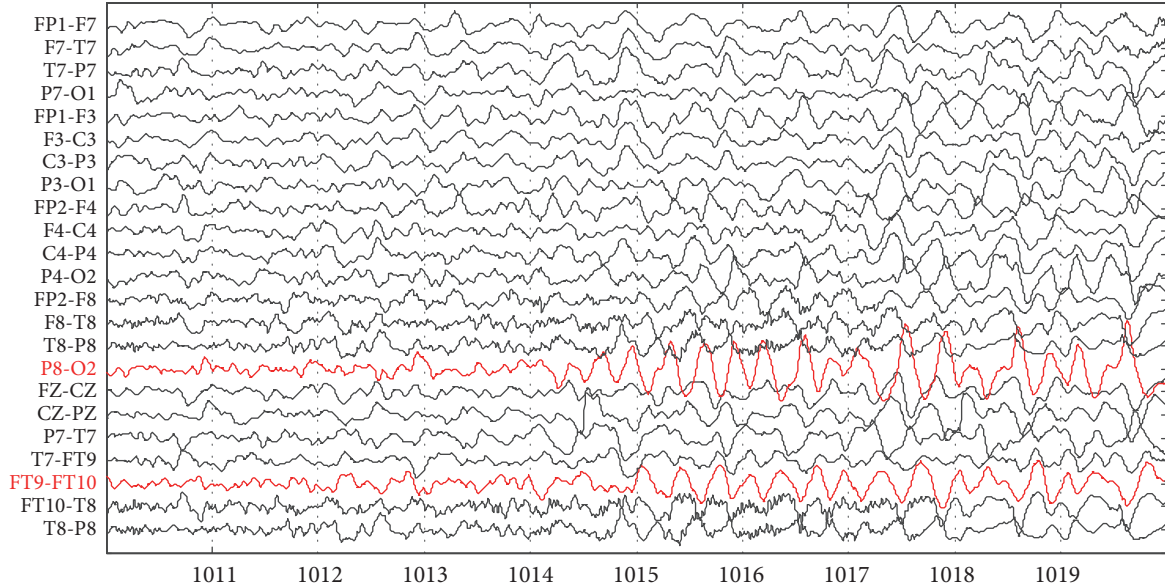


FIGURE 3: The continuous scalp EEG recordings with a seizure in Patient II. The EEG channels (P8-O2, FT9-FT10) involved in a seizure were marked as red.

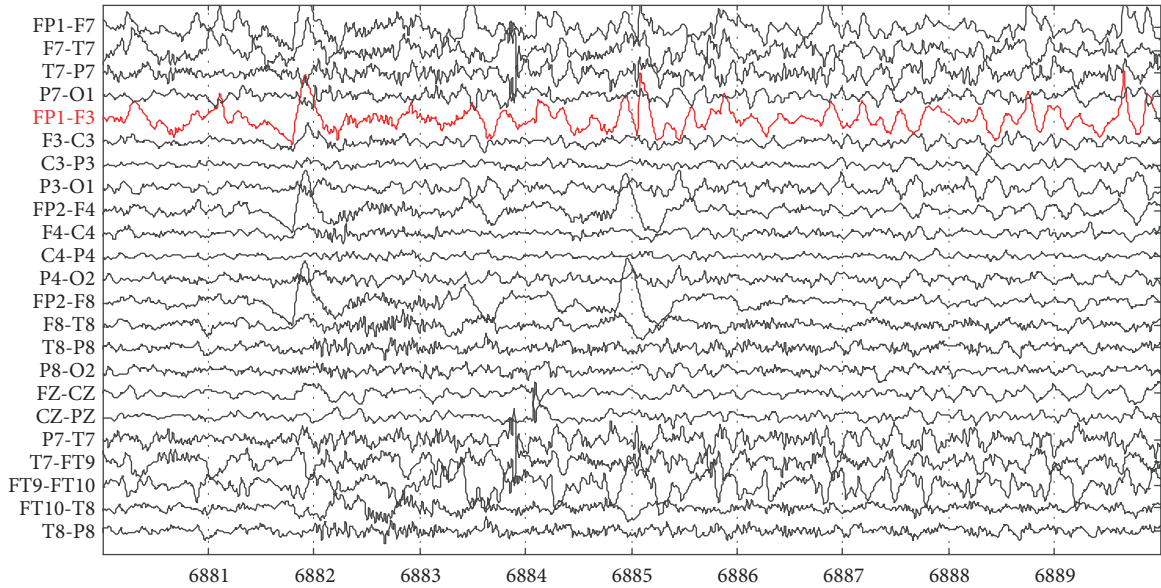


FIGURE 4: The continuous scalp EEG recordings with another seizure in Patient I. The EEG channels (FP1-F3) involved in a seizure were marked as red.

2.4. Time Evolution. Though the spatial complexity feature H_T can capture the dynamics of multichannel EEG adequately, it is still unable to explore how an epoch relates to those in the recent past, as the extraction of H_T is only based on the current epoch. Hence, H_T cannot reflect how a seizure emerges from background EEG nor how it evolves. In order to extract such evolution information, a stacked feature vector \mathcal{H}_T , called spatial-temporal complexity, is constructed by concatenating the spatial features from W nonoverlapping

consecutive 2-second epochs, as shown on the right side of Figure 5.

It should be noted that encoding the temporal evolution of EEG as \mathcal{H}_T is not equal to forming a single feature vector H_T from a longer epoch. This is because the former preserves the discrete events, while the latter smears the complexity signatures of those events. In general, when an EEG abnormality is considered as a seizure, it should persist and evolve for at least 4–10 seconds. To incorporate this

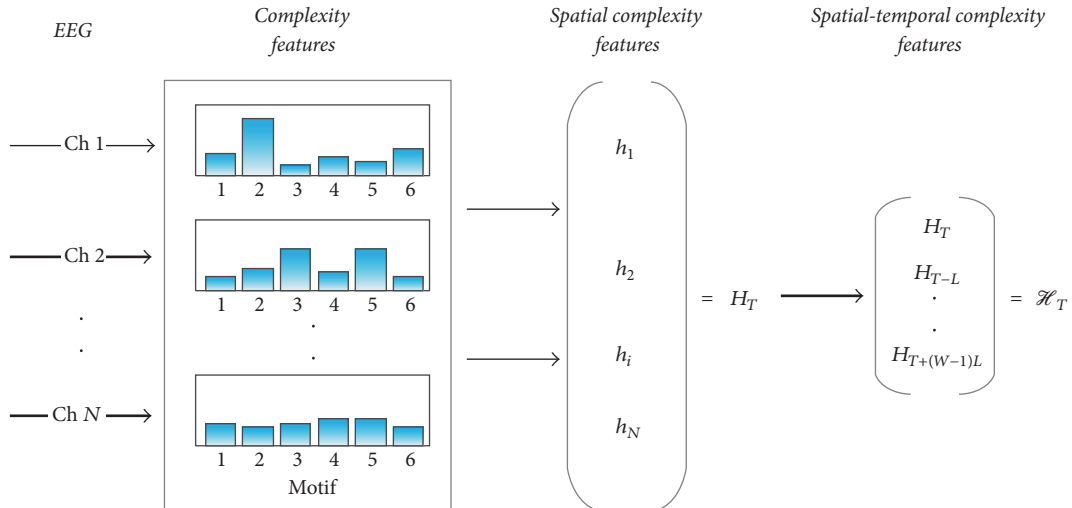


FIGURE 5: The extraction process of spatial-temporal permutation entropy.

domain knowledge, W is set as 2 in this study so that the classifier considers the evolution of feature vectors over 4 seconds.

2.5. Classification. To evaluate the detectability of the proposed spatial-temporal complexity, discriminant analysis (DA) [23] is used to classify a feature vector into the representative of seizure or seizure-free activity. DA performs classification by minimizing the within-class covariance and simultaneously maximizing the between-class covariance. There are two reasons why we choose DA in this work: (1) DA has preferable performance than other classifiers (such as decision tree and support vector machine) in seizure detection [3, 15]; (2) DA is a nonparameter classification method, which is very convenient for clinicians to build the basis for patient-specific detection. In addition, quadratic discriminant analysis (QDA) is used to distinguish between seizure and seizure-free phases in this work, as QDA has more predictability power than linear discriminant analysis (LDA).

To estimate the classification performance for a patient, a leave-one-out cross-validation scheme is adopted; we considered to evaluate the performance based on leaving out hour-long records rather than second-long epochs, as the latter would cause misleadingly good results by including the features of training data close to temporal proximity to those in the test data. Let N_s (median $N_s = 5$) denote the number of seizure records. We train the detector on the epochs selected from $N_s - 1$ seizure records, and then the detector is tested in the remaining seizure record. This process is repeated N_s times so that each seizure record is tested. The average values of performance measures (such as sensitivity and specificity) over the N_s folds are taken as the final estimates of the classifier performance. In this study, the sensitivity and specificity are defined as the proportion of ictal EEG and interictal EEG that are correctly identified, respectively.

3. Results

3.1. Characteristics of Seizure EEG. To investigate the characteristics of EEG with seizure, we firstly compare the complexity of seizure EEG and seizure-free EEG. As different patients in this dataset may have different seizure types, only the channel where the rhythmic activity develops most prominently is considered for each patient in this part. The distribution of PE and SE of seizure-free and seizure EEG for all 23 patients is illustrated in Figure 6. It can be found that the PE values of seizure EEG (0.57 ± 0.036) are much lower than those of seizure-free EEG (0.62 ± 0.03), and the SE values of seizure EEG (0.35 ± 0.1) are also much lower than those of seizure-free EEG (0.46 ± 0.11). To investigate whether their distributions are significantly different, the paired t -test is then performed. And the result shows that both the differences of PE ($t(22) = 9.66, p < 0.001$) and SE ($t(22) = 7.73, p < 0.001$) are significant, which means that the complexity of seizure EEG is significantly lower than that of seizure-free EEG. Epileptogenic processes are hypothesized to result from an abnormal hypersynchronization of the electrical activity of different zones in the brain. In the underlying complex network, a “critical” node associated with a “critical area” (i.e., the epileptogenic zone) starts a recruitment procedure of other areas until the brain triggers the seizure in order to reset this unbearable condition [24]. The neuronal hypersynchronization is expected to affect the complexity of the EEG signal itself: indeed, an excess of synchronization of the nodes of the underlying complex network may also anticipate a substantial complexity’s reduction of the EEG signal. Together with our findings, complexity of scalp EEG can be used as an indicator to monitor the dynamics of brain state.

3.2. Sensitivities of Detectors. Overall, our spatial-temporal complexity detector can obtain very promising performance:

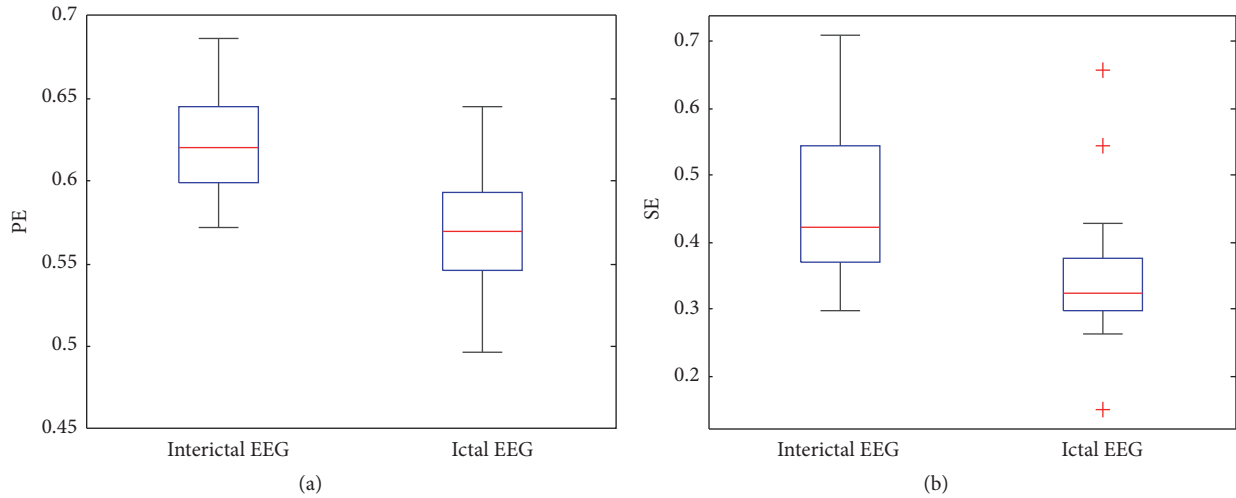


FIGURE 6: Boxplot of permutation entropy (a) and sample entropy (b) for interictal and ictal EEG on all the 23 patients. On each box, the central mark is the median, the edges of the box are the 25th and 75th percentiles, and the plus signs represent outliers which are more than 1.5 times the interquartile range.

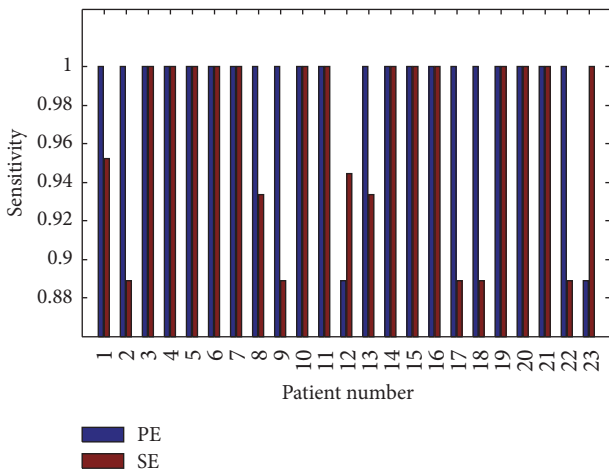


FIGURE 7: Sensitivity of our patient-specific detector.

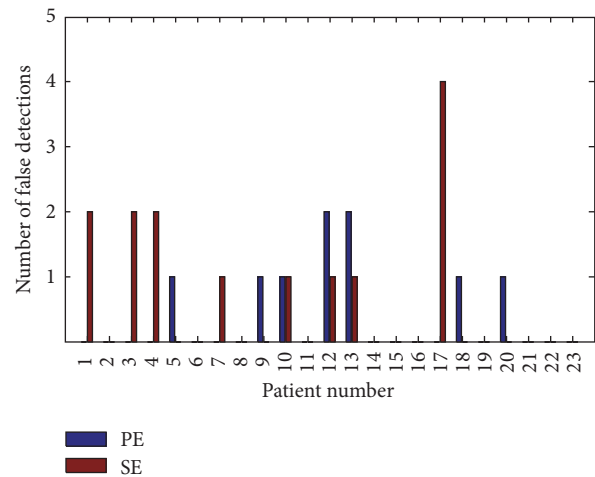


FIGURE 8: Specificity of our patient-specific detector.

the average sensitivities of PE and SE over 23 patients are 99% and 96.6%, respectively. More specifically, the sensitivities of PE and SE for each patient are illustrated in Figure 7. It can be found that the lowest sensitivity of our detector is 88.9%, and the PE detector even can precisely identify ictal EEG for all the patients except for patients 12 and 23.

3.3. Specificities of Detectors. The proposed spatial-temporal complexity detector can accurately recognize almost all the interictal EEG, and both the specificities of PE and SE approach to 100%. To in-depth demonstrate the advantages of our proposed detector, Figure 8 gives the cumulative number of false detection of interictal EEG for each patient. It can be found that there is no false detection in most patients for both PE and SE detectors. The highest number of false detection number is only 4 for the SE detector in patient 17, which is

very small as there are 900 interictal EEG ($300 * 3$, 3 seizure records in patient 17).

4. Discussion and Conclusion

Epileptic seizures involve most of the cerebral cortex, and the dynamic mechanism of the transition from the seizure-free phase to the seizure phase is highly complicated. Moreover, for different patients and different seizure onset, the involved cortical areas and the time course in the seizure transition are different. Therefore, an efficient and robust seizure detection method which is able to distinguish between seizure-free EEGs and seizure EEGs in a fast and precise way is highly desirable [9]. In this paper, a novel method for automatic detection of epileptic seizure is proposed based on the spatial-temporal complexity of scalp EEG. As the proposed feature

can take full advantage of spatial information to represent different seizures, it can be directly used to construct patients-specific detectors. The results show that our proposed detector can accurately identify 88.9% seizure EEG at least for a single patient and almost all the seizure-free EEG.

Although both the PE and SE-based spatial-temporal complexity methods have exciting performance in seizure detection, the detectability of PE still outperforms that of SE. PE is associated with the order structure of vectors in a phase space while SE is based on the similarity of vectors in a phase space, which means that PE is less sensitive to noise embedded in EEG recordings [25]. Furthermore, the advantage of PE is that it can be applied to clinical real-time online monitoring of epileptic seizures because of its simple implementation and fast computation. Therefore, the high identification performance and the low computational cost make it possible to build a real-time detection system of epileptic seizures on the basis of the spatial-temporal PE method.

Conflicts of Interest

The authors declare that there are no conflicts of interest regarding the publication of this paper.

Acknowledgments

This work was supported by the Opening Fund of Zhejiang Provincial Top Key Discipline of Computer Science and Technology at Zhejiang Normal University.

References

- [1] World Health Organization, "Epilepsy," <http://www.who.int/mediacentre/factsheets/fs999/en/>.
- [2] R. S. Fisher, C. Acevedo, A. Arzimanoglou et al., "ILAE official report: a practical clinical definition of epilepsy," *Epilepsia*, vol. 55, no. 4, pp. 475–482, 2014.
- [3] K. Zeng, J. Yan, Y. Wang, A. Sik, G. Ouyang, and X. Li, "Automatic detection of absence seizures with compressive sensing EEG," *Neurocomputing*, vol. 171, pp. 497–502, 2016.
- [4] H. Preissl, W. Lutzenberger, and F. Pulvermüller, "Is there chaos in the brain?" *Behavioral and Brain Sciences*, vol. 19, no. 2, pp. 307–308, 1996.
- [5] H. Korn and P. Faure, "Is there chaos in the brain? II. Experimental evidence and related models," *Comptes Rendus Biologies*, vol. 326, no. 9, pp. 787–840, 2003.
- [6] R. G. Andrzejak, G. Widman, K. Lehnertz, C. Rieke, P. David, and C. E. Elger, "The epileptic process as nonlinear deterministic dynamics in a stochastic environment: An evaluation on mesial temporal lobe epilepsy," *Epilepsy Research*, vol. 44, no. 2–3, pp. 129–140, 2001.
- [7] E. D. Übeyli, "Automatic detection of electroencephalographic changes using adaptive neuro-fuzzy inference system employing Lyapunov exponents," *Expert Systems with Applications*, vol. 36, no. 5, pp. 9031–9038, 2009.
- [8] N. Kannathal, M. L. Choo, U. R. Acharya, and P. K. Sadasivan, "Entropies for detection of epilepsy in EEG," *Computer Methods and Programs in Biomedicine*, vol. 80, no. 3, pp. 187–194, 2005.
- [9] Y. Song, J. Crowcroft, and J. Zhang, "Automatic epileptic seizure detection in EEGs based on optimized sample entropy and extreme learning machine," *Journal of Neuroscience Methods*, vol. 210, no. 2, pp. 132–146, 2012.
- [10] J. S. Richman and J. R. Moorman, "Physiological time-series analysis using approximate entropy and sample entropy," *American Journal of Physiology-Heart and Circulatory Physiology*, vol. 278, no. 6, pp. H2039–H2049, 2000.
- [11] J. M. Yentes, N. Hunt, K. K. Schmid, J. P. Kaipust, D. McGrath, and N. Stergiou, "The appropriate use of approximate entropy and sample entropy with short data sets," *Annals of Biomedical Engineering*, vol. 41, no. 2, pp. 349–365, 2013.
- [12] X. Li, G. Ouyang, and D. A. Richards, "Predictability analysis of absence seizures with permutation entropy," *Epilepsy Research*, vol. 77, no. 1, pp. 70–74, 2007.
- [13] G. Ouyang, J. Li, X. Liu, and X. Li, "Dynamic characteristics of absence EEG recordings with multiscale permutation entropy analysis," *Epilepsy Research*, vol. 104, no. 3, pp. 246–252, 2013.
- [14] J. Li, J. Yan, X. Liu, and G. Ouyang, "Using permutation entropy to measure the changes in EEG signals during absence seizures," *Entropy*, vol. 16, no. 6, pp. 3049–3061, 2014.
- [15] K. Zeng, G. Ouyang, H. Chen, Y. Gu, X. Liu, and X. Li, "Characterizing dynamics of absence seizure EEG with spatial-temporal permutation entropy," *Neurocomputing*, In press.
- [16] N. Nicolaou and J. Georgiou, "Detection of epileptic electroencephalogram based on Permutation Entropy and Support Vector Machines," *Expert Systems with Applications*, vol. 39, no. 1, pp. 202–209, 2012.
- [17] D. Chen, S. Wan, J. Xiang, and F. S. Bao, "A high-performance seizure detection algorithm based on Discrete Wavelet Transform (DWT) and EEG," *PLoS ONE*, vol. 12, no. 3, Article ID e0173138, 2017.
- [18] S. M. Haas, M. G. Frei, and I. Osorio, "Strategies for adapting automated seizure detection algorithms," *Medical Engineering Physics*, vol. 29, no. 8, pp. 895–909, Oct 2007.
- [19] A. Shoeb, H. Edwards, J. Connolly, B. Bourgeois, S. Ted Treves, and J. Guttag, "Patient-specific seizure onset detection," *Epilepsy & Behavior*, vol. 5, no. 4, pp. 483–498, 2004.
- [20] A. Shoeb and J. Guttag, "Application of machine learning to epileptic seizure detection," in *Proceedings of the 27th International Conference on Machine Learning, ICML 2010*, pp. 975–982, June 2010.
- [21] K. Zeng, D. Chen, G. Ouyang, L. Wang, X. Liu, and X. Li, "An EEMD-ICA Approach to Enhancing Artifact Rejection for Noisy Multivariate Neural Data," *IEEE Transactions on Neural Systems and Rehabilitation Engineering*, vol. 24, no. 6, pp. 630–638, 2016.
- [22] C. Bandt and B. Pompe, "Permutation entropy: a natural complexity measure for time series," *Physical Review Letters*, vol. 88, no. 17, Article ID 174102, 2002.
- [23] W. S. Rayens, "Discriminant analysis and statistical pattern recognition," *Journal of the Royal Statistical Society*, vol. 168, no. 3, pp. 635–636, 2005.
- [24] N. Mammone, D. Labate, A. Lay-Ekuakille, and F. C. Morabito, "Analysis of absence seizure generation using EEG spatial-temporal regularity measures," *International Journal of Neural Systems*, vol. 22, no. 6, Article ID 1250024, 2012.
- [25] X. Li, S. Cui, and L. J. Voss, "Using permutation entropy to measure the electroencephalographic effects of sevoflurane," *Anesthesiology*, vol. 109, no. 3, pp. 448–456, 2008.